PEOPLE'S DEMOCRATIC REPUBLIC OF ALGERIA

MINISTRY OF HIGHER EDUCATION AND SCIENTIFIC RESEARCH

UNIVERSITY YAHIA FARES OF MEDEA



FACULTY OF TECHNOLOGY

THESIS

To obtain the degree of

DOCTOR in : MECHANICAL ENGINEERING

Speciality : Energy

Presented by : HADJERI Amel

Thesis title

Numerical Study by Fluid–Structure Interaction of the Spreading and Solidification of a Particle on a Substrate during the Formation of a Ceramic or Metallic Lamella

Defended in front of a jury composed of :

Last and first name	Grade	Institution of affiliation	Designation
Alliche Mounir	Professor	University of Medea	President
Zirari mounir	Professor	University of Medea	Supervisor
Kezrane Mohamed	Professor	University of Medea	Co-supervisor
Bacha Nacer Eddine	Professor	University of Blida	Examiner 1
Chiba younes	Professor	University of Medea	Examiner 2
Danouni samir	MCA	University of Tipaza	Examiner 3

Academic year : 2025/2026

REPUBLIQUE ALGERIENNE DEMOCRATIQUE ET POPULAIRE
MINISTERE DE L'ENSEIGNEMENT SUPERIEUR ET DE LA RECHERCHE SCIENTIFIQUE
UNIVERSITE DE MEDEA



FACULTE DE TECHNOLOGIE

THESE DE DOCTORAT

Présentée en vue de l'obtention du diplôme de

Docteur en : GÉNIE MÉCANIQUE

Specialité : Énergétique

Présentée par : HADJERI Amel

Thème

Étude Numérique par Interaction Fluide Structure, de l'Étalement et la Solidification d'une Particule sur Substrat, pendant le Processus de Formation de Lamelle Céramique ou Métallique

Présentée devant le jury composé de :

Nom & Prénom	Grade	Institution d'affiliation	Designation
Alliche Mounir	Professeur	University de Médéa	President
Zirari mounir	Professeur	University de Médéa	Directeur de thèse
Kezrane Mohamed	Professeur	University de Médéa	Co- Directeur de thèse
Bacha Nacer Eddine	Professeur	University de Blida	Examinateur 1
Chiba younes	Professeur	University de Médéa	Examinateur 2
Danouni samir	MCA	University de Tipaza	Examinateur 3

Année académique : 2025/2026

Dedication

My beloved parents.

With all my love and deepest gratitude, I dedicate this work to you for your unconditional love and endless support.

My mother, you were my guiding light and the source of my strength in moments of despair.

My father, your sacrifices and your belief in me have been the driving force behind my success.

Thank you for being the pillars of my life.

ACKNOWLEDGMENT

I must initially thank Allah for offering me such strength, will, and patience to finish this work, so praise be to Allah.

First and foremost, I would like to express my deepest gratitude to my supervisor, ***Pr. ZIRARI Mounir****, for his continuous guidance, support, and encouragement from the beginning and still today. His expertise and advice have been invaluable to the progress and completion of this research. I feel truly privileged to have had the opportunity to work under his supervision.*

I extend my sincere thanks to my co-supervisor, ***Pr. KEZRAN Mohamed****, for his valuable support to pursue my research with clarity, dedication, and confidence.*

Special thanks go to ***Pr. ALLICHE Mounir*** *for kindly agreeing to chair the examination jury for this thesis. His presence and contribution are greatly appreciated.*

I would sincerely like to thank all the examination board members, ***Pr. BACHA Nacer Eddine****,* ***Pr. CHIBA Younes*** *and* ***Dr. DANOUNI samir****, for dedicating their time to read and evaluate this work, despite their multiple occupations.*

Finally, I would like to thank ***Dr. TAHAR Souad****, for her support, availability, and kindness.*

To my family, thank you for your unconditional love, prayers and encouragement. Your support has been my source of strength throughout this journey.

With heartfelt gratitude,

HADJERI Amel

ABSTRACT

Achieving high-performance coatings requires advanced surface treatment techniques capable of precisely controlling material properties and deposition behavior. Among these, thermal spray and cold spray processes. In this thesis, both techniques are investigated through numerical simulations to better understand the spreading, solidification, and bonding mechanisms that govern the formation of ceramic and metallic lamellae. In the thermal spray process, molten droplets at high temperature impact a solid substrate to produce a cohesive coating. While cold spray technology relies on the impact of high-velocity solid particles, where bonding occurs through plastic deformation without melting the material. A fluid–structure interaction (FSI) model was developed to simulate the spreading and solidification behavior of a molten or semi-molten particle impacting a solid substrate. The model accounts for the coupled fluid dynamics, solid response, and heat transfer between the droplet and the substrate, and investigates the influence of impact parameters such as multiple-droplet impacts, initial droplet velocity, the presence of a solid core, and substrate oxidation on the final lamella morphology. Subsequently, the solid-state particle deposition process in cold spray technology was simulated using a three-dimensional model based on the Coupled Eulerian–Lagrangian (CEL) approach. The effects of particle velocity, material properties, and thermal conditions on the deposition and bonding mechanisms were then analyzed. A key finding of this research is that the high kinetic energy of thermally sprayed droplets is closely associated with an increased spreading rate, which facilitates the formation of flat and uniform splats. Within the cold spray process, high kinetic energy primarily induces severe plastic deformation, thereby enhancing particle/substrate bonding strength. Additionally, the models used in the current study were corroborated through numerical and experimental analyses conducted under the same conditions.

Keywords: Coatings, thermal spray, cold spray, bonding, fluid structure interaction (FSI), Coupled Eulerian-Lagrangian (CEL).

RÉSUMÉ

La réalisation de revêtements haute performance nécessite des techniques de traitement de surface avancées, capables de contrôler précisément les propriétés des matériaux et le comportement du dépôt. Parmi celles-ci, on trouve les procédés de projection thermique et de projection à froid. Dans cette thèse, ces deux techniques sont étudiées par simulation numérique afin de mieux comprendre les mécanismes d'étalement, de solidification et de liaison qui régissent la formation des lamelles céramiques et métalliques. Dans le procédé de projection thermique, des gouttelettes fondues à haute température impactent un substrat solide pour former un revêtement cohésif. La projection à froid, quant à elle, repose sur l'impact de particules solides à grande vitesse, où la liaison se produit par déformation plastique sans fusion du matériau. Un modèle d'interaction fluide–structure (FSI) a été développé afin de simuler le comportement d'étalement et de solidification d'une particule fondue ou semi-fondue impactant un substrat solide. Le modèle prend en compte le couplage entre la dynamique du fluide, la réponse mécanique du solide et les transferts thermiques entre la goutte et le substrat, et étudie l'influence de paramètres d'impact tels que les impacts multiples de gouttes, la vitesse initiale de la particule, la présence d'un cœur solide et l'oxydation du substrat sur la morphologie finale de la lamelle. Par la suite, le procédé de dépôt de particules à l'état solide par projection à froid a été simulé à l'aide d'un modèle tridimensionnel basé sur l'approche couplée eulérienne-lagrangienne (CEL). Les effets de la vitesse des particules, des propriétés du matériau et des conditions thermiques sur les mécanismes de dépôt et de liaison ont ensuite été analysés. Une conclusion clé de cette recherche est que l'énergie cinétique élevée des gouttelettes projetées thermiquement est étroitement associée à une vitesse d'étalement accrue, ce qui facilite la formation de projections planes et uniformes. Dans le procédé de projection à froid, une énergie cinétique élevée induit principalement une déformation plastique importante, améliorant ainsi la résistance de la liaison particules/substrat. De plus, les modèles utilisés dans la présente étude ont été corroborés par des analyses numériques et expérimentales menées dans les mêmes conditions.

Mots-clés : Revêtement, projection thermique, projection à froid, collage, interaction fluide structure (FSI), couplage eulérien-lagrangien (CEL).

ملخص

يتطلب تحقيق طلاءات عالية الأداء تقنيات معالجة سطحية متقدمة قادرة على التحكم بدقة في خصائص المواد وسلوك الترسيب. من بين هذه التقنيات، عمليتا الرش الحراري والرش البارد. في هذه الرسالة، تُدرس كلتا التقنيتين من خلال محاكاة رقمية لفهم آليات الانتشار والتصلب والترابط التي تحكم تكوين الصفائح الخزفية والمعدنية بشكل أفضل. في عملية الرش الحراري، تصطدم قطرات منصهرة عند درجة حرارة عالية بركيزة صلبة لإنتاج طلاء متماسك. بينما تعتمد تقنية الرش البارد على اصطدام جسيمات صلبة عالية السرعة، حيث يحدث الترابط من خلال التشوه اللدن دون ذوبان المادة. طُوّر نموذج تفاعل بنية السوائل في البداية لمحاكاة سلوك الانتشار والتصلب لجسيم منصهر/شبه منصهر يصطدم بركيزة صلبة.تم تطوير نموذج تفاعل مائع–بنية (FSI) لمحاكاة سلوك الانتشار والتصلب لجسيم منصهر أو شبه منصهر عند اصطدامه بركيزة صلبة. يأخذ النموذج في الاعتبار الاقتران بين ديناميكا المائع والاستجابة الميكانيكية للصلب وانتقال الحرارة بين القطرة والركيزة، كما يدرس تأثير معلمات الاصطدام مثل اصطدام القطرات المتعددة، والسرعة الابتدائية للجسيم، ووجود قلب صلب، وأكسدة الركيزة على الشكل النهائي للطبقة المتكونة. بعد ذلك، تمت محاكاة عملية ترسيب الجسيمات في الحالة الصلبة بتقنية الرش البارد باستخدام نموذج ثلاثي الأبعاد قائم على منهج أويلريان-لاغرانج المقترن . ثم حُللت آثار سرعة الجسيمات، وخصائص المواد، والظروف الحرارية على آليات الترسيب والترابط. ومن أهم نتائج هذا البحث أن الطاقة الحركية العالية للقطرات المرشوشة حرارياً ترتبط ارتباطاً وثيقاً بزيادة معدل الانتشار، مما يُسهّل تكوين بقع مسطحة وموحدة. في عملية الرش البارد، تُحفز الطاقة الحركية العالية بشكل رئيسي تشوهاً لدناً شديداً، مما يُعزز قوة الترابط بين الجسيمات والركيزة. بالإضافة إلى ذلك، تم تأكيد صحة النماذج المستخدمة في هذه الدراسة من خلال تحليلات عددية وتجريبية أُجريت في ظل الظروف نفسها.

الكلمات المفتاحية: الطلاء،الرش الحراري، الرش البارد، الترابط، تفاعل بنية السائل ، الاقتران الأويلي-اللاجرانجي.

TABLE OF CONTENTS

GENERAL INTRODUCTION 1
Chapter 1 Literature review on droplet deposition process 3
Introduction 4
1.1. Droplet impact dynamics 4
1.1.1. Spreading and recoiling of droplets 4
1.1.2. Spreading factor 11
1.1.3. Droplet splashing 12
1.2. Substrate characteristics 16
1.2.1. Hydrophilic and hydrophobic surfaces 16
1.2.2. Surface roughness 18
1.2.3. Oxidation of the substrate surface 21
1.3. Droplet solidification 22
Conclusion 28
Chapter 2 Numerical methodology 29
Introduction 30
2.1. Governing equations (fluid domain) 31
2.2. Interface tracking method 33
2.3. Numerical implementation and fluid-structure coupling 36
2.4. Finite element method 38
Conclusion 42
Chapter 3 Numerical simulation of molten droplet deposition 43
Introduction 44
3.1. Model Validation 45
3.2. Results and discussion 47
3.2.1. The effect of droplet spacing 47
3.2.2. The effect of impact velocity 56
3.2.3. The effect of solid core within the droplet in successive impacts 64
3.2.4. The effect of the substrate oxidation 70
Conclusion 73
Chapter 4 Numerical simulation of high-velocity solid particle impact 75
Introduction 76

4.1. Previous studies: Experimental results 79
4.2. Numerical approaches 84
4.2.1. Lagrangian method 84
4.2.2. Eulerian method 85
4.2.3. Arbitrary Lagrangian Eulerian method 85
4.2.4. Coupled Eulerian Lagrangian method 85
4.2.5. Smoothed Particle Hydrodynamics method 86
4.3. Numerical methodology 86
4.3.1. Johnson-Cook (JC) Plasticity Model 87
4.3.2. The Mie–Gruneisen Equation of State 88
4.3.3. Johnson-Cook (JC) Damage Model 88
4.4. Model validation 88
4.5. Results and discussion 94
4.5.1. The influence of impact velocity 95
4.5.2. The influence of particle-substrate material combinations 104
4.5.3. The influence of particle and substrate preheating 117
4.5.4. Mixed Al–Cu multi-particle deposition 112
Conclusion 121
GENERAL CONCLUSION 128
Perspectives 130
Appendix A: Radial temperature evolution of a fully molten aluminum droplet during single and successive impacts on a steel substrate under thermal spray conditions 131
Appendix B: Stress concentration during the impingement of droplets on the substrate 133
Appendix C: Eulerian Material Assignment (Volume Fraction tool) 136
Appendix D: Multi-particle deposition of Al and mixed Al–Cu particles 138
References 139

LIST OF FIGURES

Figure 1.1 Droplets behavior during the impact ontosolid substrate [1] 4

Figure 1. 2 Droplet impacting onto a solid substrate: (a) Low Weber number. (b) High Weber number [2] 6

Figure 1. 3 Droplet evolution behavior. (a) Re = 100, We = 100, single droplet. (b) Re = 100, We = 10, binary droplets. (c) Re = 100, We = 50, binary droplets [4] 7

Figure 1. 4 Droplet evolution behavior, We = 100 and Re = 500 [4] 8

Figure 1. 5 Spreading time for different Oh number (Re=200 and We=16.384) [5] 9

Figure 1. 6 Wetting states of a liquid droplet [7] 9

Figure 1. 7 Force balance at the contact line 10

Figure 1. 8 Droplets morphology during the coalescence for θ=70° (left side) and θ=120° (right side) (Re=200 and We=16.384) [5] 11

Figure 1. 9 The evolution of splat morphology with the substrate temperature. (a) splash splat at =300 K, (b) disk splat at =723 K, (c) the transition temperature [22] 14

Figure 1. 10 Splashing evolution for the droplet impacts of water and ethanol on dry smooth solid surfaces [23] 15

Figure 1. 11 Influence of angle of impact surface. (Top :15°, middle: 30° and bottom 45°). For We = 970 and Re = 8700 at 3 atm [24] 15

Figure 1. 12 Contact angle of hydrophobic and hydrophilic surfaces [30] 17

Figure 1. 13 Contact meniscus geometry created with spherical asperity [33] 19

Figure 1. 14 (a) A liquid droplet in Wenzel state, (b) A liquid droplet in Cassie–Baxter state [34] 19

Figure 1. 15 Wetting states under both static and dynamic situations on super-hydrophobic surfaces. (a) A sensile droplet in Wenzel state; (b) A sensile droplet in Cassie–Baxter state; (c) Cassie–Baxter state (no impalement at low impact velocity); (d) an area close to the impact zone switches to Wenzel state (high impact velocity) [32] 20

Figure 1. 16 Obliquity parameter of surface topography 22

Figure 1.17 The variation of the droplet heights at the impact with and without solidification [45] 23

Figure 1.18 The spreading with a substrate temperature Tw = 298.15 K . (a) The temperature distribution at different Weber numbers. (b) The temperature distribution at different Stwe. The blue color represents the solidified layer (areas with temperatures below), the other parts are represented with the color bar [48] 25

Figure 1. 19 Solidification microstructure of YSZ lamella [43] 26

Figure 1. 20 Schematic diagram of liquid solidification with supercooling [51] 27

Figure 2. 1 Volume of fluid method [57] 34

Figure 2. 2 Solidification front representations using [63] 36

Figure 2.3 Domain Discretization for Quadratic Shape Function [67] 40

Figure 3.1 Computational domain of droplet impact on solid substrate 44

Figure 3.2 Deposition of molten Al droplet on a solid substrate. (a) Experiment of reference [33] (b) Simulation results 46

Figure 3.3 Evolution of the spreading factor: comparison between the experimental results of [33] and the simulation results of the present study 47

Figure 3.4 Impact of dual aluminum droplets simultaneously, with changing the spacing between the droplets 49

Figure 3. 5 Non simultaneous impact of dual Al droplets 50

Figure 3.6 Successive impact of dual Al droplets 52

Figure 3. 7 Temperature distribution of single and binary droplets at different time intervals 52

Figure 3. 8 The evolution of spreading velocity with the radial position 55

Figure 3. 9 The evolution of pressure over time 56

Figure 3. 10 Comparison of splat diameter during successive impact of droplets at different impact velocities 56

Figure 3.11 The evolution of spreading velocity with the radial position for different impact velocities 57

Figure 3.12 The evolution of pressure with the radial position for different impact velocities 58

Figure 3.13 The temporal variation of temperature corresponding to various impact 59

velocities

Figure 3.14 Comparison of splat diameter during simultaneous impact of droplets at different impact velocities 60

Figure 3.15 The evolution of spreading velocity with the radial position for different impact velocities 62

Figure 3.16 The evolution of pressure with the radial position for different impact velocities 62

Figure 3.17 The temporal variation of temperature distribution corresponding to various impact velocities 64

Figure 3.18 Comparison of splat diameter during the successive impact of droplets for four different solid core percentages 65

Figure 3.19 The temporal variation of the temperature distribution for four different solid core percentages 66

Figure 3.20 The evolution of spreading velocity with the radial position for four different solid core percentages 67

Figure 3. 21 The evolution of pressure with the radial position for four different solid core percentages 68

Figure 3. 22 XY shear stress distribution over time in successive impact for four different solid core percentages 70

Figure 3. 23 The evolution of spreading factor over time for all the cases 72

Figure 3.24 The temperature distribution within the droplet during its deposition on oxidized substrate 72

Figure 3. 25 The evolution of pressure at the point of impact for all the cases 73

Figure 3. 26 XY shear stress distribution over time 73

Figure 4. 1 Bonding mechanisms based on material combinations [76] 77

Figure 4. 2 The schematic diagram of the cold spray system [80] 79

Figure 4. 3 Surface morphology of coating deposition from experiment of reference [87] 80

Figure 4.4 SEM micrograph of the top surfaces of (a) Al 1050 (b) AlSi10Mg, and (c) Scalmalloy powders generated by CS process from reference [88] 80

Figure 4. 5 (a) Cross-sectional SEM image of a single Ni particle deposition on different Al substrates adabted from experiment of reference [89]. (b) Substrate surface region after different surface pretreatments (C1: polished substrate, C2: ground substrate, C3: grit-blasted substrate by small size Al2O3 sand and C4: grit-blasted substrate by large size Al2O3 sand) 81

Figure 4. 6 Single HEA particle depositing onto a 6082 Al alloy substrate from experiment of reference [90]. (a) Surface morphology. (b) cross-sectional view. 81

Figure 4.7 Single Cu particle impact morphologies on both hardened and softened substrates with varying surface roughnesses from experiment of reference [91] 83

Figure 4.8 Cross section micrographs of splats formed at different particle velocities (a) 363 m/s (b) 403 m/s and (c) 469 m/s, from reference [92] 83

Figure 4. 9 Photographs of brittle coating on iron cracked obtained by single particle impact at angles of 30◦ and 90◦ and impact velocity of 100m/s from experiment of reference [93] 84

Figure 4. 10 (a) Geometry of the 2D axisymmetric Lagrangian model. (b) Meshing of the model 90

Figure 4. 11 Surface to surface contact 90

Figure 4.12 Evolution of the equivalent plastic strain (PEEQ) in Al/Al impact: (a) 5ns, (b) 10ns, (c) 20ns, (d) 30ns, (e) 40ns, and (f) 60ns. (a) Results of [77]. (b) Our simulation's results 91

Figure 4.13 Figure 4.13 (a) Geometry of the 3D CEL model. (b) Meshing of the model 92

Figure 4.14 Evolution of the equivalent plastic strain (PEEQ) in Al/Al impact. (a) 3D Lagrangian model. (b) 3D CEL model 93

Figure 4.15 Evolution of the equivalent plastic strain (PEEQ) in CrFeNi-Al impact. (a) Simulation's results of [104]. (b) Our simulation's results 94

Figure 4. 16 Contours of the equivalent plastic strain of Al/Al impact at different speeds 96

Figure 4.17 Simulation profiles of surface erosion of Al substrate impacted by Al particle at 1700 m/s 97

Figure 4. 18 Contours of the temperature of Al/Al impact at different speeds 97

Figure 4. 19 Time evolution of (a) PEEQ and (b) temperature of Al/Al impact at different velocities 98

Figure 4. 20 SEM image (a) and simulation results (b) of a single Al particle deposition at 700m/s 99

Figure 4. 21 The calculation model of the mult-impact 100

Figure 4. 22 Contours of the equivalent plastic strain of dual Al particles impact at different speeds 101

Figure 4. 23 Contours of the equivalent plastic strain of multiple Al particles impact at different speeds 101

Figure 4. 24 Contours of temperature of dual Al particles impact at different speeds 102

Figure 4. 25 Contours of temperature of multiple Al particles impact at different speeds 103

Figure 4. 26 Computational domain of multi-particles impact model 103

Figure 4. 27 PEEQ contour of multi-particles impact at a velocity of 900 m/s 104

Figure 4. 28 PEEQ of Al/Cu, Cu/Al, Cu/Cu and Cu/Ti6Al4V impacts within 60ns at 500, 700 and 900m/s 109

Figure 4. 29 Evolution of particle compression ratio with different velocities 111

Figure 4. 30 Evolution of comparative deformation ratio with different velocities 111

Figure 4. 31 Evolution of substrate crater depth with different velocities 111

Figure 4. 32 Evolution of PEEQ, temperature and von Mises of all cases after 60ns at different velocities 116

Figure 4. 33 Energy evolution process over time at impact velocity of 900m/s. (a) Al/Al, (b) Al/Cu, (c) Cu/Al, (d) Cu/Cu. 117

Figure 4. 34 PEEQ distribution for Cu/Al impact after 60ns, at different particle temperatures 119

Figure 4. 35 PEEQ distribution for Cu/Al impact after 60ns at different substrate temperatures 119

Figure 4. 36 PEEQ distribution for Cu/Al impact after 60ns at different temperatures of whole-model 119

Figure 4. 37 SEM image of Cu/Al impact 119

Figure 4. 38 Evolution of (a) compression ratio, (b) comparative deformation ratio and (c) 120

crater depth of the substrate at different heating temperatures

Figure 4. 39 PEEQ distribution of Cu/Al impact. (a) T= 900 K, V=500m/s and t= 60ns (b) T=900 K, V=200m/s and t=100ns (c) T=1200 K, V=200m/s and t=100ns 121

Figure 4. 40 Cu–Al particles deposition on Al substrate at 700m/s: (a) Equivalent plastic strain distribution. (b) Von Mises stress distribution. (c) Temperature distribution 123

Figure 4. 41 (a) Time evolution of equivalent plastic strain (PEEQ) at point A for Al and mixed Al-Cu particle impacts. (b) Time evolution of temperature at point A for Al and mixed Al-Cu particle impacts. Point A represents the top surface of the first impacting particles, (Cu) 125

Figure 4.42 Cu–Al particles deposition on Al substrate: (a) Equivalent plastic strain distribution. (b) Von Mises stress distribution. (c) Temperature distribution. Critical velocities of Al and Cu particles are taken 600 and 510m/s, respectively 126

LIST OF TABLES

Table 1.1 Contact angle measurements [19] 18

Table 3.1 Properties of the materials used [1] 45

Table 3.2 Droplets deposition: (a) simultaneously (b) non-simultaneously (c) successively. 47

Table 3.3 Properties Fe2O3 oxide layer [33] 70

Table 4.1 Material properties of Aluminum [77] 92

Table 4.2 Parameters of the study 95

Table 4.3 The Johnson-Cook damage model [107] 95

Table 4.4 Material properties 104

Table 4.5 Equation of state (Eos) [108] 105

Table 4.6 Johnson–Cook damage model 105

Table 4.7 Types of impact 105

NOMENCLATURE

Latin letters

A	Initial yield stress [MPa]
B	Hardening modulus [MPa]
Bi	Biot number
C	Strain rate sensitivity coefficient
C_0	Bulk speed of sound
C_p^{eq}	Equivalent specific heat [J kg^{-1} K^{-1}]
d	Diameter [m]
d_o	Intial diameter [m]
d_1	Baseline failure strain
d_2	Pressure sensitivity of failure strain
d_3	Stress triaxiality effect on failure strain
d_4	Strain rate sensitivity of failure strain
d_5	Thermal sensitivity of failure strain
d_{max}	Maximum diameter [m]
D_p	Initial particle diameter
E	Young's modulus [Pa]
E_H	Internal energy on the Hugoniot curve
E_m	Internal energy at the current state
f	Volume fraction
F_b	Drag force [N]
F_{ST}	Surface tension force [N]
g	Gravity [ms^{-2}]
h	Heat transfer coefficient [W m^{-2} K^{-1}]

h_p	Height of the deformed particle
hs	Sensible heat [J]
h^*	Dimensionless crater depth
H	Total enthalpy [J]
ΔH	Latent heat [J kg^{-1}]
k	Thermal conductivity [W m^{-1} K^{-1}]
K	Splashing parameter
K_c	Critical splashing factor
K_f	Splashing parameter on flattening
m	Thermal softening exponent
n	Strain hardening exponent
Oh	Ohnesorge number
P	Pressure [Pa]
p_H	Hugoniot pressure
Q	Thermal source
R_a	Surface roughness [m]
Re	Reynolds number
S	Linear Hugoniot slope coefficient.
S_k	Obliquity parameter
T	Temperature [K]
T_m	Melting temperature [K]
T_r	Reference temperature [K]
T_s	Substrate temperature [K]
T_t	Transition temperature [K]
u	Displacement vector
v	Velocity [m/s]

V_f	Kinematic Continuity
We	Weber number

Greek symbols

Γ	Gruneisen ratio
δ	Dirac function
ε_e	Strain
ε_{pl}	Equivalent plastic strain
$\dot{\varepsilon_0}$	Reference strain rate
$\dot{\varepsilon_{pl}}$	Equivalent plastic strain rate
η	Nominal volumetric compressive strain $(1 - \rho/\rho_0)$
θ	Contact angle [°]
Δθ	Contact angle hysteresis [°]
μ	Dynamic viscosity [kg m^{-1} m^{-1}]
ξ_{max}	Maximum spreadin factor
ρ	Fluid density [kg·m^{-3}]
ρ_s	Density of the solid [g/cm³]
σ	Surface tension [N/m]
σ_e	Stress [N/m²]
σ_{eq}	Equivalent stress
σ_{LG}	Contact angle between liquid surface and gas surface [°]
σ_m	Mean stress
σ_{SG}	Contact angle between solid surface and gas surface [°]
σ_{SL}	Contact angle between solid surface and liquid surface [°]
σ_s	Cauchy stress tensor
τ	Viscous stress tensor
$\emptyset_j$	Trial functions

χ	Roughness ratio
Θ	Volume fraction in phase change

List of Abbreviations

ALLFD	Frictional dissipation
ALLKE	Kinetic energy
ALLSE	Strain energy
ALLPD	Plastic dissipation
AVOF	Algebraic volume of fluid
CDR	Comparative deformation ratio
CEL	Coupled Eulerian Lagrangian
CR	Compression ratio
CS	Cold spray
FSI	Fluid-Structure interaction
GVOF	Geometric volume of fluid
JC	Johnson and Cook
PEEQ	Equivalent plastic strain
SPH	Smoothed particle hydrodynamics
VOF	Volume of fluid

"The secret of a good sermon is to have a good beginning and a good ending; and to have the two as close together as possible."

-George Burns-

GENERAL INTRODUCTION

The deposition behavior of droplets on solid substrates has been extensively investigated over the past decades owing to its critical role in various industrial applications, such as thermal spray coatings. In these processes, the formation of ceramic or metallic lamellae enhances surface properties and improves overall performance. The origins of droplet impact studies date back to 1876, when Worthington first photographed the impact of a water droplet using high-speed imaging techniques. Later, in the early 20th century, Max Ulrich Schoop pioneered the thermal spray process in Switzerland, marking the beginning of a versatile coating technology that continues to attract significant attention. This surface treatment technique involves heating metal powders to a molten or semi molten state and projecting them into the part of the surface to be coated. As the droplets solidify, they form protective layers. In addition to droplet spreading, several physical phenomena may occur during the droplet impingement, including rebound and splashing [1]. The final morphology of the splat (lamella) depends on initial impact conditions (such as impact velocity, droplet shape and size, droplet temperature and material proprieties) and the physical properties of the substrate (oxidation and roughness).

The current study simulates the impact of aluminum alloy 380 (80% Al, 8% Si, 4% Cu, and 2% Fe) onto a steel substrate under various conditions to predict coating quality and optimizing the process parameters, using Computational Fluid Dynamics software.

Over the past few years, interest in cold-gas dynamic spraying (CGDS), commonly referred to as cold spraying, has increased substantially.

Cold spray is another coating technique that is studied in this work. It allows for the formation of dense and well adhered coatings. This technology was discovered in the mid-1980s, by Anatolii Papyrin’s team in Russia. Although both cold spray and thermal spray share the same objective, they are based on distinct physical principles. The CS involves the impact of solid powder, and thus it is a "solid-state deposition process". The powders are at temperature lower than the melting temperature of the material. However, they are projected at high velocities; hence the coatings are achieved through the plastic deformation of the sprayed particles.

The thermal spray process mostly depends on thermal energy (heat transfer between the droplet and the substrate), while the CS relies on the kinetic energy. Since the materials in CS process are below the melting temperature (low temperatures), the thermal issues; like oxidation can be avoided, which makes it suitable for temperature sensitive materials.

Numerical simulation of CS was performed to examine the main factors influencing the morphology of the coating and the bonding mechanisms, such as particle initial velocity, particle /substrate combination material, and preheating temperature.

Chapter 1

Literature review on droplet deposition process

This chapter presents a brief description of droplet dynamics during coating processes. It includes the key parameters that affect droplet spreading, splashing, solidification, and rebound, such as impact dynamics, the contact angle, and substrate characteristics. This chapter covers the phenomena that may occur during the droplet deposition, by previewing the preceding literature.

Introduction

1.1. Droplet impact dynamics

Understanding the mechanics of a droplet's impact is a major challenge in industrial applications such as inkjet printing, biomedical applications, and spray coating manufacture. In addition, it is a common phenomenon in nature, which can be observed in numerous scenarios including rainfall. The study of droplet dynamics on a wet and dry solid surface has gradually developed using theoretical and experimental methods. As the droplet impacts the substrate, it may adhere, rebound, spread, or splash [1], as shown in Figure 1.1. This behavior is dependent on the characteristics of both droplet (size, velocity, temperature, etc.) and substrate (oxidation, roughness, wettability, etc.). This section focuses on the study of droplet's impact and spreading on solid surfaces in order to produce thin metallic or ceramic coatings.

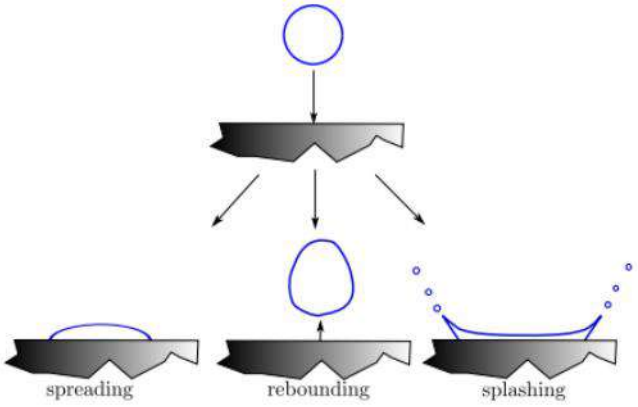


Figure 1.1 Droplets behavior during the impact onto solid substrate [1]

1.1.1. Spreading and recoiling of droplets

In thermal spray process, improving coating properties requires a deep understanding of the dynamics spreading of droplets (molten or semi-molten) on a solid substrate during the formation of the lamella. The spreading and recoil of droplets are primarily characterized by dimensionless numbers of Reynolds and the Weber. In which the Reynolds determines the ratio of inertial forces to viscous forces. The Weber is used to calculate the ratio of inertial forces to surface tension.

$$\mathrm{Re} = \frac{\rho \, v \, d}{\mu} \tag{1.1}$$

$$\mathrm{We} = \frac{\rho\, v^2\, d}{\sigma} \tag{1.2}$$

The Ohnesorge number quantifies the balance between viscous force, inertia, and surface tension force. While the Reynolds and Weber numbers change depending on how fast the particle is moving, the Ohnesorge number is independent of velocity. It describes the fluid's inherent resistance to being deformed or broken up based purely on its physical properties and size. It is defined as:

$$\mathrm{Oh} = \frac{\sqrt{\mathrm{We}}}{\mathrm{Re}} \tag{1.3}$$

The contact angle (θ) that forms between a solid surface and a liquid-gas is another factor that affects the deposition and recoiling of hitting droplets. This angle varies throughout the dynamic phases (advancing during spreading and receding during recoil); once the droplet reaches equilibrium, the static contact angle is determined by Young's equation as follow:

$$\mathrm{Cos}\ \theta = \frac{\sigma_{SG} - \sigma_{SL}}{\sigma_{LG}} \tag{1.4}$$

A. Weber number, We:

Weber number defines the ratio of droplet kinetic energy to its surface energy. Hao Yi et al [2] studied the evolution of molten metal droplets (for both high and low Weber number) impacting onto a cold substrate. When droplets impact the substrate at low Weber number, it spreads to the maximum diameter, and then it begins to retract and returns to its original shape under surface tension forces. In this case, wettability becomes the primary factor in determining droplet behavior. At large Weber number, inertial forces become predominant over surface tension forces, leading to more significant spreading during impact, in this phase, the wettability effects become negligible.

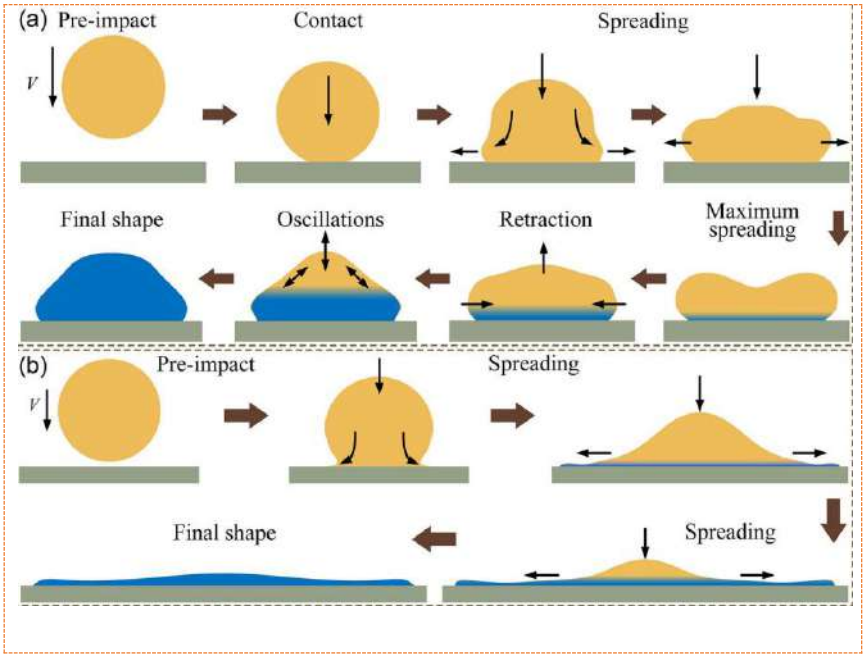


Figure 1. 2 Droplet impacting onto a solid substrate: (a) Low Weber number. (b) High Weber number [2]

In numerous literatures, numerical simulations of impacting droplets on superhydrophobic substrates were investigated for different Weber number values. Yang Ma et al [3] conducted a comparison of the morphology evolution of single and binary droplets when they impact the substrate. The single droplet detaches from the substrate after reaching the maximum spreading. When the droplet/substrate combination has a high contact angle (Super hydrophobic surface), then inertia will act to maintain excess surface energy upon impact and may partially recede the droplet and even bounce off the substrate [1]. At We=10, the binary droplets begin to construct a liquid bridge between themselves, which causes the droplets to merge. These droplets rebound due to the effect of surface tension. However, at high Weber number (We=50), the inertia is dominant at the first instant, and then the rebound occurs due to the surface's low wettability. For high Weber number (We > 200), the wettability is negligible [4].

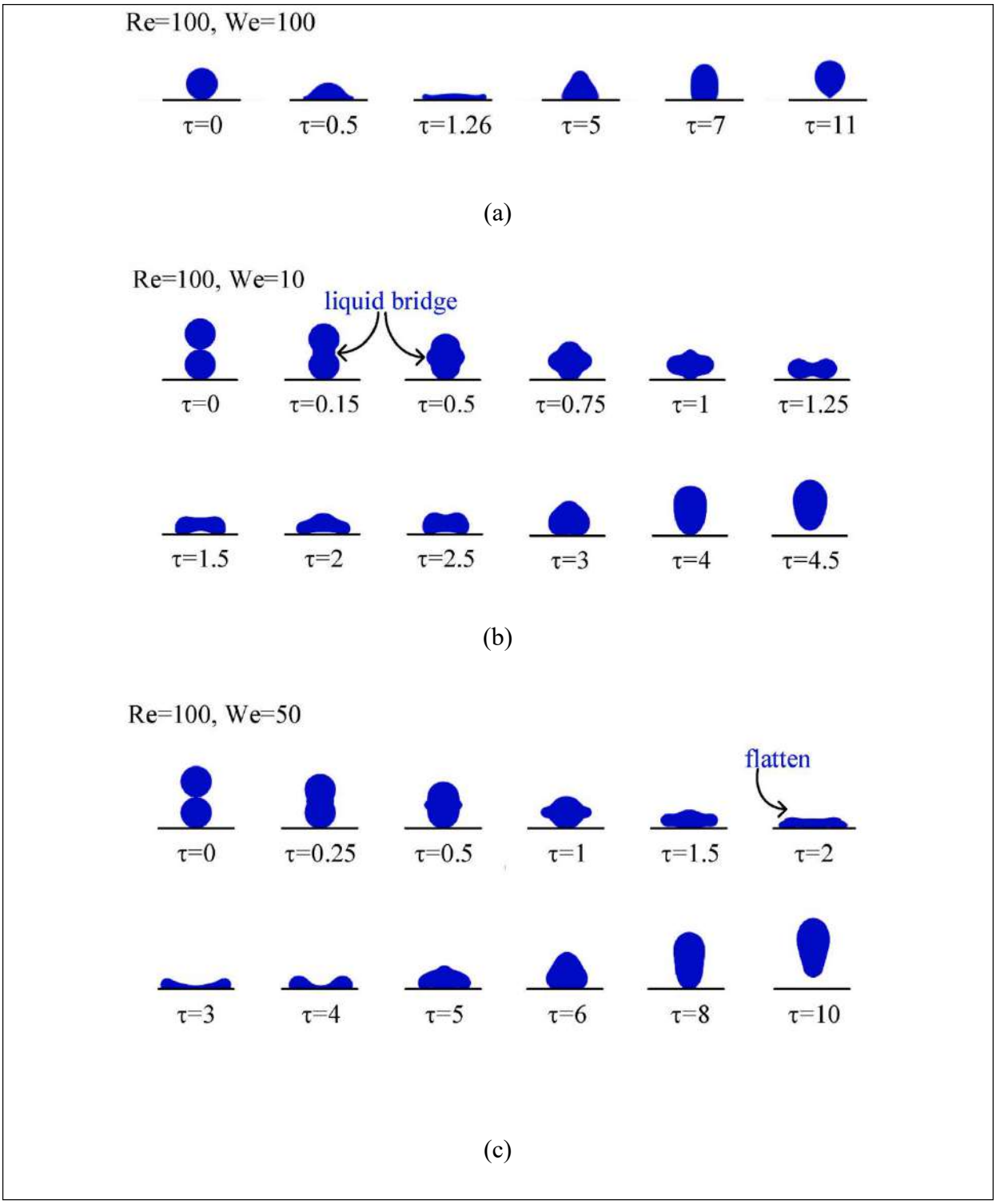


Figure 1. 3 Droplet evolution behavior. (a) Re = 100, We = 100, single droplet. (b) Re = 100, We = 10, binary droplets. (c) Re = 100, We = 50, binary droplets [4]

B. Reynolds number, Re:

The Reynolds number also characterizes the behavior of the impacting droplets (spreading or recoiling). It represents inertial forces to viscous forces ratio. At high Reynolds number,

inertial dominates viscous forces, thus, the droplet spreads rapidly. Conversely, a low Reynolds number indicates that viscous forces play a dominant role.

In highly viscous droplets, the droplet's kinetic energy is dissipated and converted into thermal energy due to the action of the viscous forces, which influence the droplet's spreading by resisting its motion. Additionally, droplet retraction is suppressed as internal friction inhibits its recoil. However, for low viscosity, the recoil is much more pronounced, where the surface tension drags the droplet inward and minimizes the contact area.

Yang Ma et al [3] revealed that on a hydrophobic surface, the droplet's contact line recedes more easily, resulting in more noticeable recoil, even at moderate Reynolds numbers (Figure 1.4).

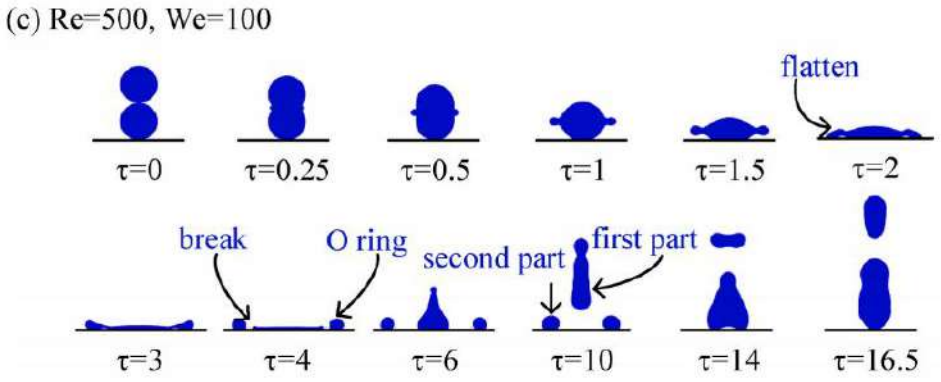


Figure 1. 4 Droplet evolution behavior, We = 100 and Re = 500 [4]

C. Ohnesorge number, Oh:

The Ohnesorge number is another crucial dimensionless parameter that describes the spreading and recoiling dynamics of droplets when they impact a surface, by comparing viscous forces with inertial and surface tension.

A low Ohnesorge number implies that surface tension forces overcome the viscous forces. This causes the droplet to spread rapidly, often leading to a large spreading. At the end of spreading, surface tension forces drive the droplet to minimize its surface and strongly recoil. While a high Ohnesorge number signifies that the viscous forces are dominant, resulting in slower spreading and the recoil is less pronounced.

Kuppa Ashoke Raman et al investigated [5] in their research the effect of droplets Ohnesorge number during the successive impact on a solid substrate. It is clear evident in Figure 1.5 that

the spreading evolution is almost similar in all the examined cases. This is due to the inertia dominated initial stage spreading. It can be observed that the spreading rate is lower at smaller Ohnesorge values.

The Ohnesorge number shows how much energy is dissipated during the spreading stage due to viscosity. When the Oh value is low, the majority of the kinetic energy is transformed into spreading, and when the Oh value is high, most of the energy is lost to viscous forces.

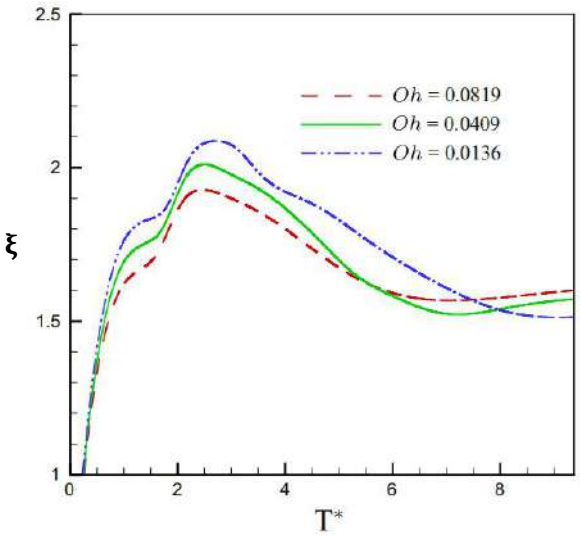


Figure 1. 5 Spreading time for different Oh number (Re=200 and We=16.384) [5]

D. Contact angle, θ:

Wettability of fluid/solid interfacial phenomena is often characterized by measuring the contact angle formed between a liquid drop and a solid surface [6]. It is a dynamic parameter that changes throughout the impact process. A small contact angle indicates good wetting, and the droplet tends to spread more readily on the substrate (Figure 1.6).

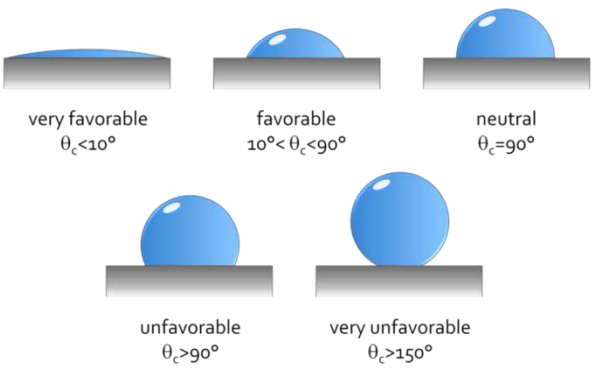


Figure 1. 6 Wetting states of a liquid droplet [7]

When a droplet comes into contact with the substrate, the three-phase contact line forms to replace the original solid–air and liquid–air interfaces [8]. The static contact angle determined at the equilibrium results from the balance of surface tensions at this three-phase contact line, as shown in Figure 1.7. A low solid–liquid surface tension indicates good wettability, allowing the entire spreading of the droplet over the surface (small contact angle). In contrast, a high solid–liquid surface tension reduces wettability (non-wetting behavior). Thus, the droplet forms a high contact angle with the substrate, i.e. minimized contact area.

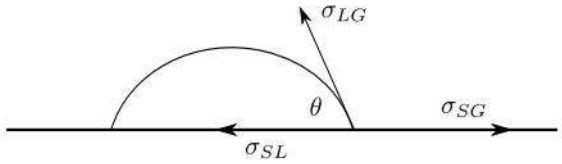


Figure 1. 7 Force balance at the contact line

The angle achieved when the three-phase contact line is pushed forward (advanced) or backward (receded) gives a better indication of solid/liquid interfacial energy [9]. Due to the adhesion force, the droplet advances on the solid surface, while the cohesion force resists the droplet spreading [8]. Advancing and receding contact angles are measured expanding and contracting quasi-statically a drop on a horizontal surface [10], the difference between the two values is referred to as contact angle hysteresis $\Delta\theta$, and it is used as a reference parameter to measure drop mobility on a surface. Contact angle hysteresis determines viscous energy dissipation due to the droplet dynamics.

According to Antonini et al [11], droplet rebound is primarily controlled by the receding contact angle. Until We = 585, the droplet bounce off was only detected on surfaces with a receding contact angle of more than 100°. As this angle increases, the rebound time decreases.

In another work of Carlo Antonini et al [12], the influence of $\Delta\theta$ on the spreading time was examined. Their findings indicate that at high value of hysteresis angle, the transition of the contact angle from the value achieved during spreading to the required one for contact line retraction requires a longer time. Thus, the spreading time increases with θ.

On an inclined substrate, due to the inclination angle, the droplet spreads in one direction and generates an advancing dynamic contact angle with the solid surface, while the droplet recedes in the opposite direction and forms a receding dynamic contact angle with the solid

surface [8]. Kuppa Ashoke Raman et al [5] studied the effect of the contact angle on the deposition behavior of successive droplets. Figure 1.8 depicts the temporal evolution of the impact with θ=70° and θ=120°. As it seen, the receding of the first droplet (or the leading droplet) is hindered due to the capillary spreading effect at 70°. However, for θ=120°, severe recoiling of the droplet was noticed, resulting in an increase in its height. The fusion of the droplets results in the formation of a connecting bridge. The narrow bridge observed at 70° is thicker compared to the one at 120°.

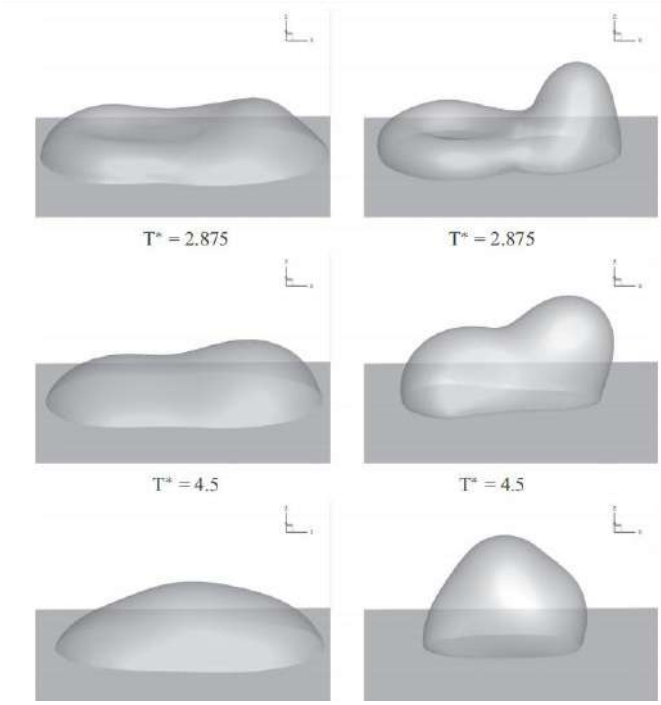


Figure 1. 8 Droplets morphology during the coalescence for θ=70° (left side) and θ=120° (right side) (Re=200 and We=16.384) [5]

1.1.2. Spreading factor, ξ:

The maximum spreading factor is used to describe droplet dynamic as it deposits on the substrate. It is defined by the ratio of the maximum diameter of the final splat and the droplet initial diameter ($\xi_{max} = d_{max}/d_o$). The spreading factor is influenced by the droplet initial conditions (such as velocity, temperature, size...) and the substrate material properties. Numerous theoretical correlations for the spreading factor have been reported in the literature expressed as functions of the Reynolds number, Weber number, Ohnesorge number, and even the contact angle. It is described as follows [13]:

$$\xi = C\,Re^{\alpha} \tag{1.5}$$

Where C takes values that vary from 0.8 corresponding to an average diameter of an extremely uneven lamella, to 1.2941 for a lamella having a regular disk shape. α is equal to either 0.2 or 0.125 or even 0.167.

H. Jones et al [14] is one of the very first authors who determined the maximum spreading factor ξ_{max} (Eq 1.6) of a molten particle projected on a solid substrate. **Both surface energy and solidification** effect were neglected in his model [15].

$$\xi_{max} = 1.16\ \mathrm{Re}^{0.125} \tag{1.6}$$

Scheller and Bousfield [16] proposed a correlation of the maximum spreading factor of **water droplet**s impact on **hydrophilic surfaces** (θ<90°), and it is given by:

$$\xi_{max} = 0.61\ (\frac{We}{Oh})^{0.166} \tag{1.7}$$

During the spreading process, there exist two basic regimes that govern droplet behavior: capillary and viscous regime. The kinetic energy is converted to capillary energy in the **capillary regime**. ξ_{max} is represented by [16]:

$$\xi_{max} = We^{1/2} \tag{1.8}$$

While the initial kinetic energy is converted into dissipation work during the **viscous regime**. ξ_{max} is obtained by Madejski [17] and Roisman et al [18]:

$$\xi_{max} = Re^{1/5} \tag{1.9}$$

Pasandideh-Fard et al [19] proposed a correlation of ξ_{max}, by considering **all energy types** at the maximum spreading.

$$\xi_{max} = Re^{1/4} \tag{1.10}$$

Another correlation of Pasandideh-Fard et al [19]. It is based on balancing energy between the maximal spreading and the moment of the impact, with **taken into account the effect of surface wettability** (Eq 1.11).

$$\xi_{max} = \sqrt{\frac{We+12}{3\ (1-cos\theta) + 4\frac{We}{\sqrt{Re}}}} \tag{1.11}$$

1.1.3. Droplet splashing

When a droplet impacts a solid surface, it can either spread smoothly or undergo splashing (breakup into smaller secondary droplets), depending on various factors such as impact velocity, temperature change, and material properties. Worthington (1876) was the first to study the splashing phenomena that happens when a liquid droplet hits a solid or liquid surface. Droplet splashing occurs if there is enough kinetic energy that causes the ejection of secondary droplets from the edges of the main droplet during deposition [20]. Numerous researchers have documented the phenomenon of droplets splashing.

The splashing parameter K presented in Eq 1.12 was used to determine the break-up phenomenon of the droplet, it was proposed by Mundo et al in 1995 [21], it is composed of both in-flight information (the dynamic characteristics of the droplet as it moves through the air before it hits the substrate) and the physical properties of the droplet. However, K is unable to explain the transition phenomenon in the flattening morphology from splash-shaped to disk-shaped with increasing substrate temperature. Therefore, in 2002, Masahiro Fukumoto et al [22] proposed the splashing parameter on flattening K_f (Eq 1.13).

A critical value of K as a criterion for splashing has been known to be $K_c = 57.7$. If the droplet diameter and impact velocity increase, K increases and splashing tends to occur (K > Kc, splashing occurs). Nevertheless, for low impact velocity, no splashing occurs and the splat has a regular disk shape, which is due to the decrease of the kinetic energy. Additionally, a critical parameter of K_f was introduced as (k_f^c), in the free-falling experiment, k_f^c was estimated to be roughly $k_f^c = 7$, independent of the substrate material, impact velocity, and droplet material. It was found that at $K_f < k_f^c$, a disk splat is formed, while a splash splat at $K_f > k_f^c$.

$$K = We^{0.5}\, Re^{0.25} \tag{1.12}$$

$$K_f = 0.5\, a^{1.25}\, Re^{-0.3}\ \text{K} \tag{1.13}$$

The parameter «a» represents the ratio between the maximum spreading velocity and to the initial particle velocity.

Figure 1.9 represents the transition from a splash splat to a disk splat, as the substrate temperature increases. The temperature of the substrate as the disk-splat fraction reaches 50% is referred to as the transition temperature T_t [22].

The presence of contaminants (which are generally water molecules and other volatile particles such as oils) on the substrate induced the formation of a gas film; this film reduced the quality of droplet/substrate contact and affects the splat morphology (the final coating). The density of contaminants is reduced with the substrate preheating, and the elimination of these contaminants will be completed at T_s=T_t . When operating in a controlled atmosphere chamber (at pressures below the critical value), the contaminants desorb from the surface, and the splat morphology becomes independent of the substrate temperature [15]. As a conclusion the desorption of contaminants leads to the formation of a disk shape [22].

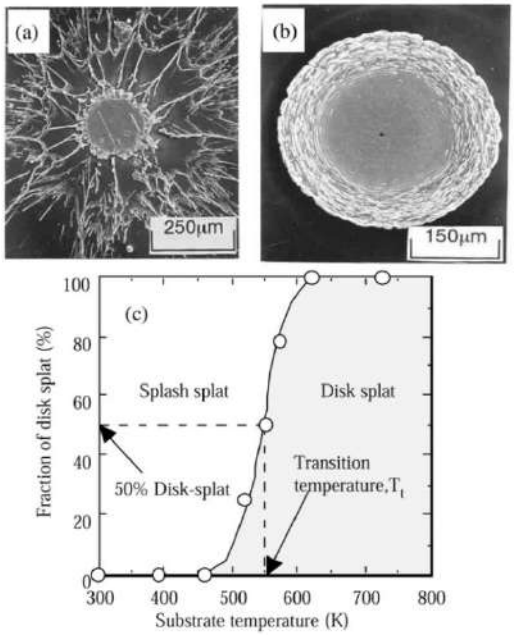


Figure 1. 9 The evolution of splat morphology with the substrate temperature. (a) splash splat at =300 K, (b) disk splat at =723 K, (c) the transition temperature [22]

The impact of droplets on dry smooth solid surfaces is a natural well-known phenomenon, which can be characterized by deposition/spreading and splashing. The splashing phenomenon is additionally categorized into two types of corona splash and prompt splash [8], as demonstrated in Figure 1.10. Furthermore, it can be observed that the water drop spreads along the flat surface with no splashes. For high Weber number (ethanol), secondary droplets are separated from the main structure of the drop. The K-parameter model that describes the droplet splashing dynamics on dry smooth solid surfaces is expressed by Eq 1.14 [23]. It applies the balance of viscous, inertia, and capillary forces.

$$K_f = Oh\, Re^{1.25} \tag{1.14}$$

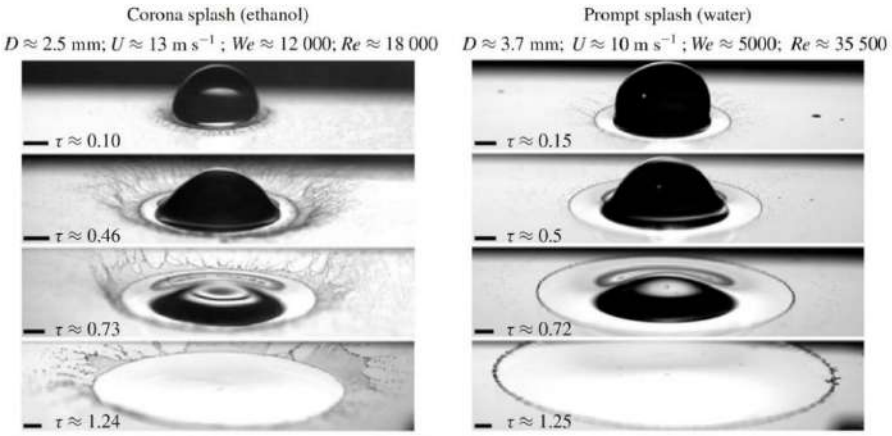


Figure 1. 10 Splashing evolution for the droplet impacts of water and ethanol on dry smooth solid surfaces [23]

Jie Liu [24] investigated the impact of FC-72 droplet onto an inclined Plexiglas surface at angles of 15, 30, and 45°, to analyze the effect impact angle. It was observed that at 15°, the splash occurs clearly on both upper and lower rims (Figure 1.11). As the inclination angle increases (30° and 45°), there is much less splashing; it only occurs in the down rim. However, Zhang et al [25] studied the spreading, splashing and solidification of yttria stabilized zirconia (YSZ) droplet after inclined impact, using smoothed particle hydrodynamics and they found that splashing occurred for a critical impact angle of approximately 44°.

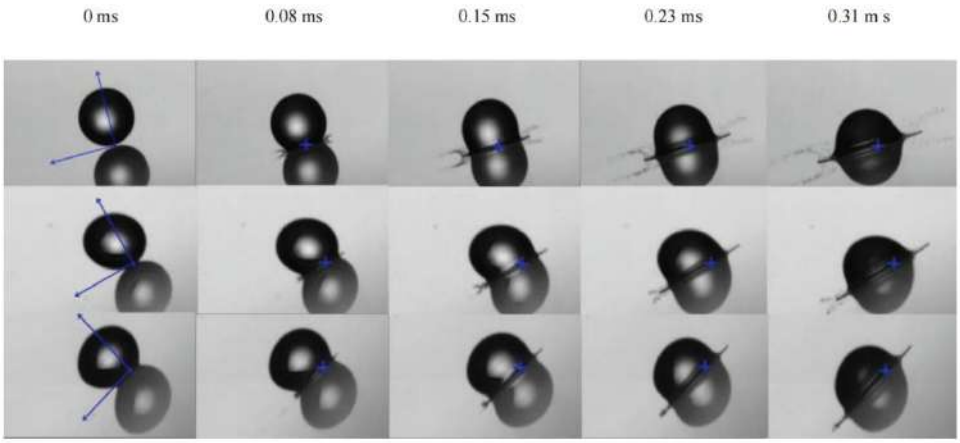


Figure 1. 11 Influence of angle of impact surface. (Top :15°, middle: 30° and bottom 45°). For We = 970 and Re = 8700 at 3 atm [24]

More succinct parameter k was proposed by Chiu et al in 2009 (Eq 1.15) [26], they found that for contact angle θ = π, the splash parameter K =1.5, without considering the substrate properties.

$$k = \frac{We}{\sqrt{Re}} < \frac{3}{4}(1 - cos\theta) \tag{1.15}$$

In another work of Zhang et al [27] investigated the influence of droplet viscosity on the splashing behavior during the impact on a smooth substrate. They found that the splashing of the droplet occurs for low viscosity. While the increase of viscosity prevents droplet splashing.

In 2021, based on a smooth particle hydrodynamic method, Chen et al [28] suggested the splashing parameter K for a metal droplet when it impacts a dry and smooth substrate (Eq 1.16). Their model can predict the impact outcomes for different temperature substrates, and it primarily sets apart between metal and nonmetal droplets.

$$K = Oh\, Re^{1.5346} \tag{1.16}$$

1.2. Substrate characteristics

The behavior of a droplet when it comes into contact with a solid substrate (whether it spreads out, retract, break up (splashes), or solidifies is determined by the properties of the substrate characteristics as well. Surface properties such as wettability and roughness influence droplet/substrate interactions, including deposition and adhesion. Strong de-wetting surfaces (hydrophobic or super hydrophobic surfaces) are necessary in many engineering applications where liquid repellence is needed in order to control the interactions between the droplet and the substrate and prevent surface corrosion, poor thermal performance, or even icing [29]. While hydrophilic surfaces are critical for coating technologies where uniform spreading of liquids is required.

1.2.1. Hydrophilic and hydrophobic surfaces

Understanding how droplets interact with hydrophilic and hydrophobic surfaces permits good coating of surfaces. Hydrophilic surfaces (good wetting) promote droplet spreading, while on hydrophobic surfaces (poor wetting) droplets spread to its maximum, then retract and finally bounce off the substrate. Wetting and de-wetting of Surfaces are determined by the contact angle. As previously discussed, low contact angle ($\theta < 90°$) indicates good wetting (hydrophilic behavior), while high contact angle ($\theta > 90°$) indicates poor wetting (hydrophobic behavior). For contact angle ($\theta > 150°$) and small contact angle hysteresis ($\Delta\theta < 10°$) the surface is considered as super hydrophobic [12]. The droplet/substrate adhesion forces are stronger on hydrophilic surfaces compared to the hydrophobic surfaces, where the cohesive forces (within the liquid itself) are the strongest, preventing further spreading of the fluid. Super-hydrophobicity provides the so-called self-cleaning effect by facilitating water shedding from surfaces and reducing surface pollution [12].

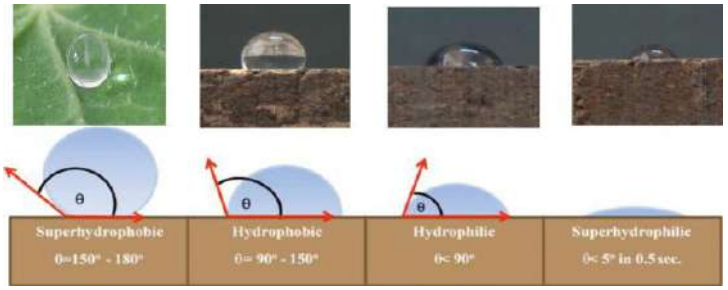


Figure 1. 12 Contact angle of hydrophobic and hydrophilic surfaces [30]

In 1997, Mao et al [31] studied impact on hydrophilic and hydrophobic surfaces with contact angles up to 97°. They found that the rebound of the droplet can be seen on substrates with equilibrium contact angles greater than 90°C. Antonini et al [32] conducted an experimental study on water drop oblique impacts onto hydrophobic and super hydrophobic tilted surfaces. The analysis led to two main findings, on super hydrophobic surfaces, surface tilting facilitated drop rebound from a surface. Also, increasing the tilt angle helped reduce drop rebound time (up to 40%). Differently, on a hydrophobic surface, no rebound was observed above a certain surface tilt angle (a=45°), and the drop stayed on the substrate, either completely or partially.

For hydrophobic surfaces, Xu Yang [4] observed that at the early stage of spreading, droplets impacting with high contact angles generated a higher spread factor than impacting onto hydrophilic surfaces with low contact angles. This is because the inertial effects can be neglected at the first instant of deposition, leaving only adhesive and cohesive forces to affect spreading, thus, the strong liquid/solid interaction on the hydrophilic surfaces prevents further spreading, in contrast to the hydrophobic surfaces' relatively weak liquid/solid interaction. In later stagee of spreading, inertial forces begin to affect the spread of the droplet.

In order to avoid liquid adhesion to the substrate, Arda et al [19] focused on developing super hydrophobic surfaces for which the methods such as: super hydrophobic spray-coating: it uses the coating to produces a surface with exceptionally high water resistance, leading the droplet to roll off the surface with minimal contact, laser-ablation: it involves the removal of material from a solid surface by irradiating it with a laser beam, the material absorbs the laser's energy and either vaporizes, melts, or sublimates, anodization: this technique converts the surface of a metal into a durable and corrosion-resistant oxide layer, and combination of laser-ablation and anodization. Table 1.1 indicates the contact angle measurement for these surfaces. The experiments were performed at surface temperature has of 25°C and 2°C. The results of 25°C indicates that the impact of the droplet onto the combined surface (in the early dynamic

stage of droplet spreading) reveals a greater value of maximum spreading factor than the laser-ablated and anodized surfaces, besides it is lower than the ones of the coated surface. At low surface temperature (2°C), the substrate whose surface was treated using the combined technique had the smallest maximum spreading factor at low surface temperatures.

Table 1.1 Contact angle measurements [19]

Surface	Contact angle	Wettability Status
Smooth surface	82° ± 2°	**Hydrophilic**
Anodized surface	108° ± 2°	**Hydrophobic**
Laser-ablated surface	117° ± 2°	**Hydrophobic**
Combined surface	150° ± 2°	**Superhydrophobic**
Spray-coated surface	158° ± 2°	**Superhydrophobic**

1.2.2. Surface roughness

Surface roughness is another factor that can significantly influence the interactions between the droplet and the solid substrate, as well as having an effect on spreading dynamics, solidification processes, and adhesion. It is determined as the arithmetic average of the deviations of surface peaks from a hypothetical perfectly smooth surface [33], i.e. it measures the irregularities on the surface. Low R_a, indicates a smoother surface which is desirable for uniform coating. While, higher R_a represents a rougher surface, which promotes uneven spreading even though it increases the adhesion. Xue et al [33] suggested an analytical model that characterizes the true contact area between liquid metal and a rough substrate (Figure 1.13). For this ideal surface, the mathematical expression for R_a is given by Eq 1.17. This model was employed to simulate the behavior of the molten droplet during the deposition on solid substrate while calculating contact resistance distribution at the interface of the liquid and the surface. The results show that further variations in contact resistance that cannot be expected from surface roughness alone are likely to be produced by a surface oxide or other impurities.

$$R_a = \frac{\int_0^{2\beta} y(x)\,dx}{2\beta} = \frac{\pi\beta}{4} \tag{1.17}$$

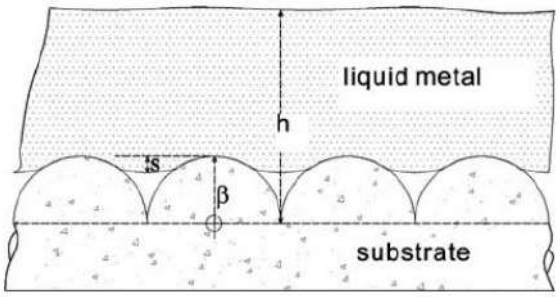


Figure 1. 13 Contact meniscus geometry created with spherical asperity [33]

Two well-known models that explain how liquid droplets interact with rough surfaces, particularly in terms of wettability and contact angle, are the Wenzel and Cassie-Baxter states (Figure 1.14**)**.

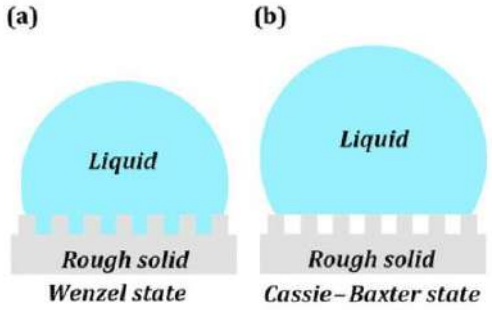


Figure 1. 14 (a) A liquid droplet in Wenzel state. (b) A liquid droplet in Cassie–Baxter state [34]

The droplet completely wets the rough surface in the Wenzel state, indicating that the liquid is entirely in contact with the substrate, even the roughness peaks, and there are no air pockets between the liquid droplet and the solid substrate. According to Wenzel, roughness of the substrate increases the liquid/solid contact. The Wenzel wetting model is represented by the following equation:

$$Cos\,\theta_{Wenzel} = \chi\ Cos\,\theta_{equilibrium} \tag{1.18}$$

Where χ is the roughness ratio.

Based on this equation, the contact angle decreases (high wettability) as hydrophilic surface roughness increases. On the other hand, increasing roughness on the hydrophobic surface results in a higher contact angle and decreased wettability [8].

Cassie and Baxter proposed another model in which the droplet does not completely wet the rough surface, instead sits on top of the peaks, and the air pockets are trapped beneath the

droplet, creating a composite interface of solid-liquid. The Cassie–Baxter wetting model is expressed by the following equation:

$$Cos\ \theta_{\text{Cassie and Baxter}} = \emptyset_1\ Cos\ \theta_{equilibrium} - \emptyset_2 \tag{1.19}$$

Where $\emptyset_1$ and $\emptyset_2$ denote the fraction of the total solid surface area, which is in direct contact with a sitting droplet and forms an equilibrium contact angle $\theta_{equilibrium}$, and the fraction of the total solid surface area, respectively [8]. The presence of air pockets enhances surface hydrophobicity, which results in an increased contact angle.

In the Cassie–Baxter, the droplets impact at low impact velocity; the droplet will rebound after impact preserving the Cassie–Baxter state. However, when velocities surpass a crucial value, droplets may not be able to rebound. In a region close to the impact zone, local liquid penetration into the surface cavities leads the wetting to move from the Cassie-Baxter to the Wenzel state, which is commonly known as impalement [32], as shown in Figure 1.15.

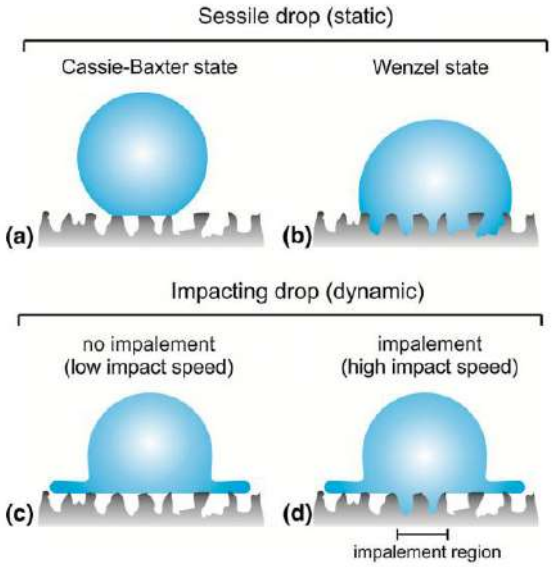


Figure 1. 15 Wetting states under both static and dynamic situations on super-hydrophobic surfaces. (a) A sensile droplet in Wenzel state; (b) A sensile droplet in Cassie–Baxter state; (c) Cassie–Baxter state (no impalement at low impact velocity); (d) an area close to the impact zone switches to Wenzel state (high impact velocity) [32]

Shakeri and Chandra [35] performed an experiment of a molten tin droplet impacting different rough substrates. The molten droplet splashed on the substrate without oscillating due to the large droplet diameter (2 mm) and the large impact velocity (4 m/s). They found that the morphology of the splat is altered due to the substrate roughness and several fingers formed around the droplet's rim on the rough surface.

Tang et al [36] experimentally investigated the change in maximum spreading factor as a function of surface roughness. They employed ethanol, decan, water, and tetradecane as working fluids. They discovered that the maximum spreading factor is reduced with the increase of surface roughness. However, the spreading factor is enhanced with the increase in impact velocity.

S. Tahar et al [37] numerically simulate the impact of successive and simultaneous droplets on a rough surface. They investigated the change in maximum spreading factor with surface roughness. They found that a peak diameter more than 5% of the droplet diameter induces concave roughness that influences mechanical adhesion, thus, the creation of a normal splat.

1.2.3. Oxidation of the substrate surface

Characterizing surface roughness provides insufficient understanding of the substrate's effect. The oxide layer that forms on the surface of the substrates also influences the formation of the coating. This layer can occur naturally due to exposure to air, high temperatures, moisture, or it can be deliberately created through controlled processes like anodizing or oxidation treatments. The oxide layer can act as a protective barrier against corrosion by preventing direct contact with corrosive elements in the environment. Thus, it is beneficial as it helps to increase the durability and lifespan of the lamella-substrate system, thereby improving the overall quality of the coating [37]. The thickness of the oxide layer increases as the substrate temperature increases [38]. High temperature oxidation is a significant issue in gas turbines because without a barrier to oxygen diffusion on the surface of the component, relatively rapid oxidation can occur above 870°C [39]. A. Abedini et al [40] conducted an experiment to determine the elemental composition of the steel substrates and to detect how much oxidation was caused by increasing surface temperature. They found that as a result of increasing the oxygen content from 35% of the total at ambient temperature to over 60% at 350°C, the oxidation increased.

The types of oxidations that form on substrates vary depending on the material, acknowledging the characteristics of these types before any coatings allow better control of the substrate properties. As an example of some common oxides: Iron oxide (FeO_3) that forms on steel, also referred to as rust, it occurs when the steel is exposed to air and moisture. Aluminum oxide (Al_2O_3), this layer prevents further oxidation and corrosion, making aluminum highly resistant to rust. When copper oxidizes, it forms cupric oxide (CuO) and cuprous oxide (Cu_2O).

Fukumoto et al [41] examined the effect of the surface condition on the splat morphology when droplets impact onto two types of mirror-polished 304L stainless steel substrates, one at room temperature, and the other heated to 673 K. The findings show that the formed oxide layer on the cold substrate (at room temperature) is only a few nanometers thick, while that formed on a hot substrate is about ten nanometers.

Preheating a stainless-steel substrate alters its surface topography at the nanometric scale, primarily due to the formation and growth of oxide peaks. These peaks can be characterized by an obliquity parameter called S_k [41], [42], as shown in Figure 1.16. Fukumoto et al [41] found that for substrates of the same nature and the same roughness R_a (a few nanometres) but with different S_k, different splat morphologies: for a positive S_k the lamella has a disk shape and for a zero or negative S_k the lamella tends towards a splash shape.

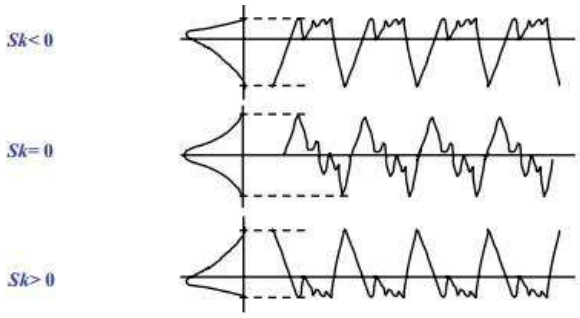


Figure 1. 16 Obliquity parameter of surface topography

The thickness of the oxidation on the metal substrate is determined by the preheated temperature and the substrate's composition. If the oxide layer is only a few nanometers in thickness, it can improve the wettability of the steel surface. However, if it exceeds 50 nm, the splashing occurs with a poor splat/substrate adhesion [15].

1.3. Droplet solidification

Solidification is a complex interplay of nucleation, growth, heat transfer, and microstructural evolution; each process can significantly influence the final characteristics of the coating. It's critical to comprehend how liquid solidification alters the spreading behavior of the droplet after deposition onto a substrate. Madjeski [17] suggests that solidification begins after the total spreading of the lamella, and the droplet kinetic energy is converted mainly into viscous dissipation work. When a molten droplet impacts a solid substrate with a given initial

temperature and a specified velocity, it spreads outward in a radial manner along the surface of the substrate, driven by inertia and opposed by surface tension and viscosity. In the meantime, the droplet temperature rapidly drops, and it begins to solidify as it loses heat to the substrate. This creates a temperature differential within the droplet and promotes the epitaxial growth of columnar microstructures as the droplet solidifies [43]. Pasandideh-Fard et al [44] pointed out that the splashing phenomenon of the droplet would not occur when the molten droplet spreads completely before solidification. The early solidification of the droplet (once it touches the surface) changes the spreading behavior. As the periphery regions solidifies, the material still in flow meets an obstacle and it creates the splashing. Additionally, solidification decreases the time needed to stabilize the thin film, without solidification the fluid spreads more, and then the thickness of the thin layer at the impact location reaches a smaller value (Figure 1.17) [45]. The solidification time value also can influence the final coating, a smooth or a rough surface topology. If the fluid completely freezes before the substrate's equilibrium thickness is achieved. i.e. early solidification, it results in a nonuniform coating relief [45]. The maximum spreading factor ξ_{max} in the case where solidification only begins when the spreading of the droplet is complete is given by Eq 1.20.

$$\frac{3\,{\xi_{max}}^2}{\mathrm{We}} + \frac{1}{\mathrm{Re}}\left(\frac{\xi_{max}}{1.2941}\right)^5 = 1 \tag{1.20}$$

For Reynolds number Re>100 and Weber numbers We>1000, the equation is simplified to:

$$\xi_{max} = 1.2941\, Re^{0.2} \tag{1.21}$$

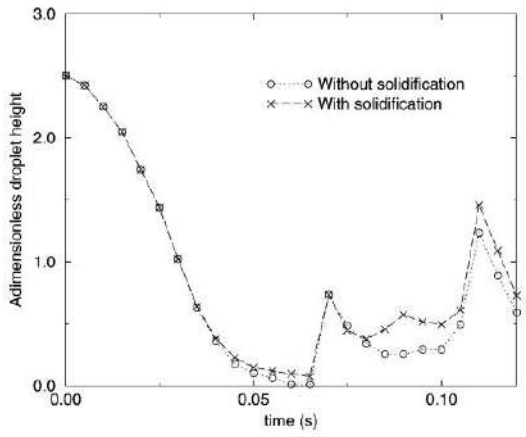
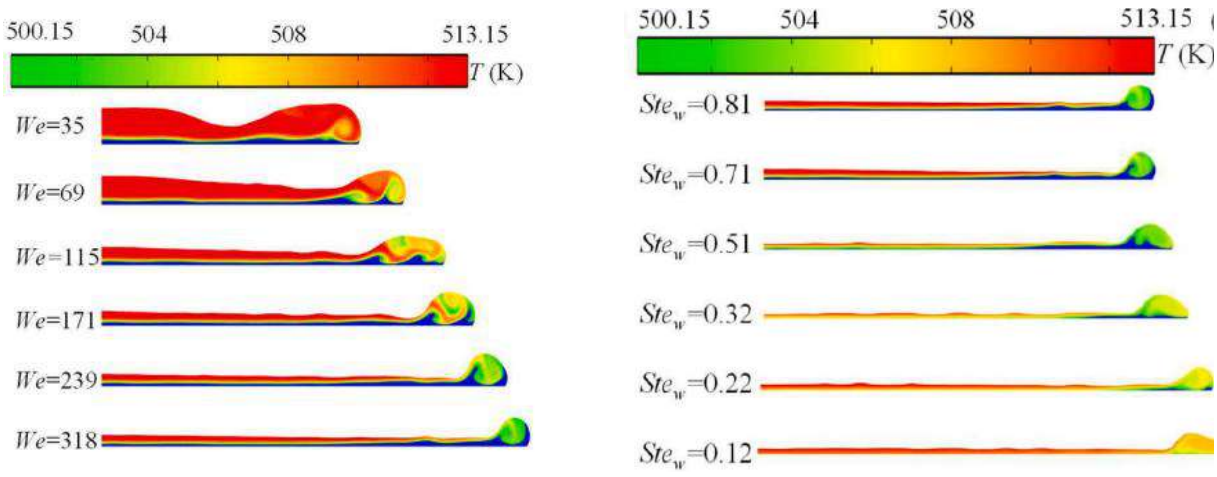


Figure 1. 17 The variation of the droplet heights at the impact with and without solidification [45]

Droplet spreading can be classified as spreading without solidification and spreading with solidification depending on the temperature of the substrate. A molten metal droplet cools and solidifies rapidly when it impacts a substrate that is at a temperature below the droplet's melting point. Conversely, no solidification occurs at substrate temperatures higher than the melting point. Thus, in this case, the droplet spreads to its maximum diameter, then retracts, and eventually bounces off the substrate, this is known as "isothermal spreading" [46].

The experimental results of Aziz et al [47] of tin droplets impacting a solid substrate at temperature of 298,15 K were used to validate the accuracy of the numerical model of Tao An et al [48] describing the solidification of metal droplets. The findings indicate that due to the solidification of the bottom of the droplet, it did not rebound; although the contact angle is high enough. During spreading with solidification, the heat is transferred from the substrate to the droplet; hence, the bottom gradually solidifies preventing the contact line from retracting. In the case of spreading without solidification, the tin droplet contracts and rebounds due to high contact angle.

Additionally, Tao An et al [48] investigate the influence of both Weber and Stew numbers on the solidification rate. As seen in Figure 1.18 (a), the bottom region of the droplet has a lower temperature indicating its solidification. As the Weber number increases, the solidification rate at the bottom accelerates. This indicates that a higher Weber number enhances the solidified layer growth by increasing heat transfer between the substrate and the droplet. Additionally, as the Stefan number decreases, the spreading factor remains unaffected by the presence of the solidified layer. For Stew < 0.12, the solidified layer shrinks and disappears (Figure 1.18 (b)).



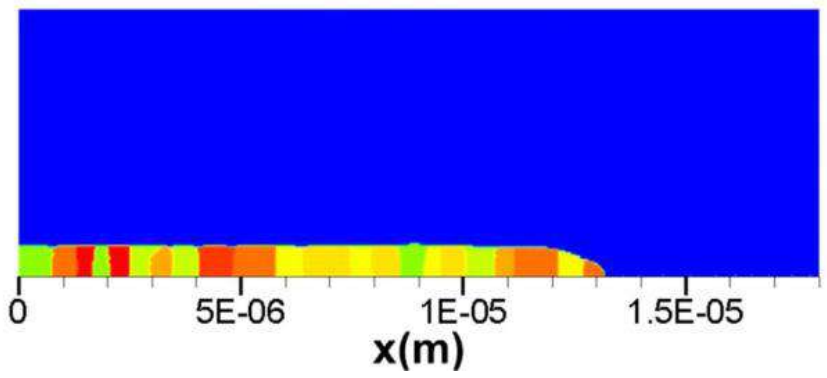
(a) (b)

Figure 1. 18 The spreading with a substrate temperature Tw = 298.15 K . (a) The temperature distribution at different Weber numbers. (b) The temperature distribution at different Stwe. The blue color represents the solidified layer (areas with temperatures below), the other parts are represented with the color bar [48]

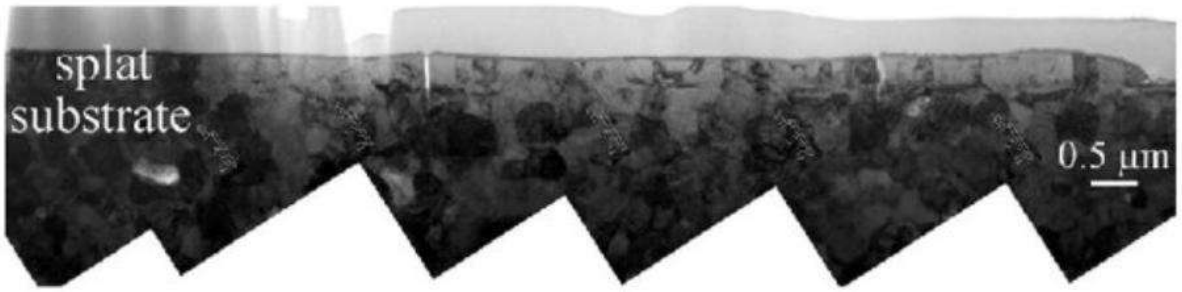
Mostaghimi et al [49] have shown that the flattening ratio is related to the Reynolds and Weber number. The solidification effect on the droplet spreading behavior, however, can be ignored when the Stefan number to Prandlt number ratio is smaller than unity (<1).

In order to study the solidification phenomenon, Amitesh Kumar et al [50] developed a numerical model of Al-33Cu/304 stainless steel substrate impact. The simulations reveal that the liquid film at the splat/substrate interface loses its momentum and merges with the solidified region as the solidification layer grows. Solidification can begin during the spreading process; however, the growth velocity of the solidified layer is significantly slower than when solidification takes place after the droplet has fully spread, which allows the splat to retain radial momentum, enabling it to reach its maximum diameter before solidifying. As spreading and solidification progress, the flow of liquid metal reduced, making surface tension more influential. This creates high-pressure regions at the splat's edges, eventually, the flow is reversed into the center, forming a bump at the rims.

Mingguang Shen et al [43] developed a numerical model of solidification formation of molten yttria-stabilized zirconia (YSZ) droplet during plasma spraying. The results reveal that the spreading droplet's solidification microstructure consists primarily of columnar grains as shown in Figure 1.19. Furthermore, even though there is a significant thermal gradient between the droplet and the preheated substrate, solidification may be safely assumed to occur mostly after spreading, due to the rapid spreading of YSZ droplets along the substrate.



(a)



(b)

Figure 1. 19 Solidification microstructure of YSZ lamella [43]. (a) numerical (b) experimental

The cooling regime that a lamella undergoes can be characterized by the dimensionless Biot number, it is defined as follows:

$$\mathrm{Bi} = \frac{\mathrm{h\,L}}{\mathrm{k}} \tag{1.22}$$

L is the thickness of the splat, k represents the thermal conductivity of the material, and h is heat transfer coefficient.

We can distinguish three cooling regimes depending on the Biot number [15]:

- Ideal cooling corresponding to a Biot number >>1: This occurs when the thermal contact between the lamella and the substrate is perfect. In this case, the heat is controlled by heat diffusion.
- Newtonian cooling corresponding to a Biot number <<1: In this case, heat transfer at the interface controls the cooling. Heat transfer is primarily governed by the lamella/substrate interface, i.e. when two materials are in contact; they exchange heat at their interface.
- Intermediate cooling between these two modes.

In their work, Mabdoua et al [15] define the process of solidification and describe its progression. They examine its stages, detailing the transformation from the liquid to the solid state. Solidification is a phase transition, in which a liquid turns into a solid when its temperature is below its freezing point. It typically involves supercooling, germination, and crystal growth.

Supercooling happens when the liquid is at a temperature below its normal freezing point (supercooled liquid), but without undergoing solidification immediately, due to a lack of nucleation sites. When nucleation sites become available, the solidification of the supercooled

liquid begins. The beginning of solidification is indicated by germination; it involves the formation of tiny solid particles called nuclei. Once nuclei have formed, the crystal growth takes place and it is occurring along with the release of latent heat, i.e. the energy released during phase change.

The release of latent heat leads to an increase in the temperature of the surrounding supercooled liquid. This phenomenon is called recalescence [51] (Figure 1.20). Nucleation decreases as the temperature increases, and the growth of existing nuclei becomes dominant over the formation of new ones. Furthermore, the nucleation process ceases once 67% of the lamella surface in contact with the substrate is covered by nuclei.

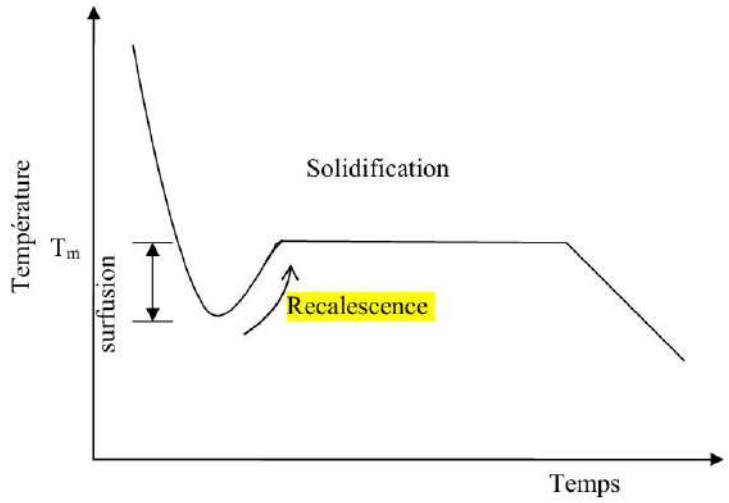


Figure 1. 20 Schematic diagram of liquid solidification with supercooling [51]

Conclusion

This chapter provides an insight review of previous research on the physical phenomena that govern droplet behavior during thermal spraying process. The results indicate that Reynolds and Weber's dimensionless numbers characterize droplet spreading and rebound. High values of these parameters (high impact velocity) lead to more significant spreading. Another factor is the contact angle, which indicates the wettability of the surface. A small contact angle means good wetting, thus high spreading rate. In addition, substrate characteristics were also discussed such as hydrophobicity, roughness, and oxidation. It was concluded that varying surface conditions affect the morphology of the lamella and the droplet/substrate adhesion mechanisms.

A critical review of the literature indicates that droplet deposition is predominantly modeled by treating the fluid and solid domains independently. There remains a lack of comprehensive numerical studies that fully coupled fluid–structure interaction; where the mechanical response of the substrate and the fluid dynamics of the droplet are solved simultaneously. Addressing this gap is essential for a deeper understanding of deposition process in thermal spray. Therefore, building upon the insights established in this chapter and the identified research gaps, the following chapter introduces the numerical methodology used to capture the droplet dynamics, heat transfer, and substrate response during thermal spray process.

Chapter 2

Numerical Methodology

This chapter introduces the numerical methodology used in the simulation of droplet impact, spreading, and solidification on a solid substrate. The simulations are conducted using Ansys Mechanical (APDL) software, implementing the FSI method. The governing equations are described for both fluid and solid domains. The VOF method is applied to determine the droplet/air free interface, in order to model immiscible multiphase flows. Additionally, the FEM is used to solve the equations numerically.

Introduction

Numerical simulations of metal droplets deposition during lamella formation focus on capturing the physics of droplet spreading, solidification, and interaction with the substrate.

Numerical methods for simulating droplets are generally divided into Lagrangian and Eulerian approaches. The Lagrangian approach focuses on tacking individual droplets to follow its motion and deformation, further it monitors solidification at the droplet level. In contrast, Eulerian approach analyses the flow at fixed locations or control volumes in the computational domain and how the fluid (droplet) properties change at these locations over time.

In the present study, the development of a two-dimensional numerical model for the impingement of droplets onto a solid substrate has been conducted using Ansys code. The VOF method that belongs to the Euler approach is applied to determine the droplet/air free interface by studying the volume ratio function. This method is widely used and well suited for simulating multiphase flows involving interface tracking.

Additionally, the finite element (FE) method solves the governing equations of the simulation by discretizing them into a system of algebraic equations, which are then solved numerically.

To investigate the droplet–substrate interaction, a fluid–structure interaction (FSI) approach is employed in the simulation. The FSI has been a topic of great interest in diverse applications such as engineering, science, and medical fields. In surface treatment application, the FSI method is used to model the impact and solidification of molten metal droplets on substrate, allowing for the optimization of material deposition and coating quality. When droplets impact on a solid substrate, the fluid force acting on the structure determines the substrate surface deformations, meanwhile the fluid behavior is determined through the substrate's properties [52].

Honegger [53] proposed the first liquid/solid interaction model, where the impact of a liquid jet onto a solid substrate causes a constant pressure, referred to as the water hammer pressure. This pressure arises from the rapid momentum change of the liquid and is transmitted into the solid as a compressive stress wave, thereby initiating the mechanical response of the substrate. Although his model provides a simplified representation of liquid/solid interaction, it laid the foundation for subsequent studies on fluid–structure interaction phenomena.

The fluid and solid domains interact only at the fluid–structure interface, where specific coupling conditions must be enforced. These conditions include kinematic compatibility, ensuring that fluid and solid velocities/displacements match at the interface, and traction equilibrium, ensuring that forces exerted by the fluid on the solid are balanced by equal and opposite forces from the solid.

In order to simplify the problem of our study and reducing its complexity, we have made some assumptions as follow:

- A two-dimensional geometry and a half spherical shape of the droplet;
- The droplet is initially assumed to be completely molten;
- The droplet impacts vertically on a fixed solid substrate;
- The initial temperature distribution within droplets is uniform;
- The fluid flow is considered incompressible, Non-newtonian and laminar;
- The heat loss of droplets by radiation and convection is neglected. This assumption is justified by the significantly higher rate of heat conduction into the steel substrate compared to the surrounding air. For multi-impacts, ignoring air convection may slightly overestimate the substrate temperature. Future studies could include convective cooling to better capture the thermal history during lamella formation.

This chapter describes the governing equations and numerical methods used to simulate the droplet deposition and its interaction with the substrate, regarded as the basis of the work will be presented in later chapters.

2.1. Governing equations

To accurately simulate the impingement, spreading, and solidification of droplets onto a substrate, a coupled numerical model was developed. This section details the governing equations.

A. Mass and momentum conservation:

The continuity and Navier-Stokes equations describe the fluid motion:

Continuity equation:

$$\frac{\partial \vec{\rho}}{\partial t} + \nabla . \overrightarrow{(\rho v)} = 0 \tag{2.1}$$

Given the incompressible of the fluid, the continuity equation is expressed as:

$$\nabla . \vec{v} = 0 \tag{2.2}$$

Momentum equation:

$$\rho \left(\frac{\partial \vec{v}}{\partial t} + \nabla . (\vec{v} . \vec{v}) \right) = - \nabla P + \nabla . \vec{\tau} + \overrightarrow{F_b} \tag{2.3}$$

P is the pressure and τ is the viscous stress tensor defined as:

$$\vec{\tau} = \mu \nabla \vec{v} \tag{2.4}$$

μ is the dynamic viscosity.

$\overrightarrow{F_b}$ is the body forces which include both gravity and surface tension forces F_{ST}.

$$F_b = \rho g + F_{st} \tag{2.5}$$

ρ is the fluid density and g is the gravitational acceleration vector.

F*st* is the volumetric surface tension force, modeled using the Continuum Surface Force (CSF) approach. This force is calculated as:

$$\mathrm{F}st = \sigma \kappa \nabla \mathrm{f} \tag{2.6}$$

where σ is the surface tension coefficient, $\kappa = \nabla \cdot (\nabla f / |\nabla f|)$ is the interface curvature, and f is the volume fraction (defined in Section 2.2). Surface tension is modeled using the built-in FLUID141 element property (SFTS) in ANSYS APDL.

B. Energy equation:

The energy conservation equation governing heat transfer during droplet impact and solidification is formulated as:

$$\rho C_p^{eq} \left(\frac{\partial T}{\partial t} \right) = \nabla \cdot (k \nabla T) + Q \tag{2.7}$$

Q, K and C_p^{eq} are the thermal source, the thermal conductivity, and the equivalent specific heat, respectively.

The phase change process during droplet impact and solidification is modeled using the equivalent specific heat method. This technique incorporates the latent heat of fusion into an effective thermal capacity, transforming the problem into a single-domain formulation with a nonlinear specific heat over the phase change interval. This method allows the thermal problem to be expressed in temperature [54].

The equivalent specific heat is defined as:

$$C_{p,eq}(T) = C_p(T) + L\,\frac{df_l}{dT} \tag{2.8}$$

Here, L is the latent heat of fusion. The derivative of the liquid fraction, dfl/dT, distributes the latent heat release/absorption over the phase change temperature range [Tsolidus,Tliquidus]. A common definition for the liquid fraction fl is:

$$f_l(T) = \begin{cases} 0 & T < T_{\text{solidus}} \\ \frac{T - T_{\text{solidus}}}{T_{\text{liquidus}} - T_{\text{solidus}}} & T_{\text{solidus}} \le T \le T_{\text{liquidus}} \\ 1 & T > T_{\text{liquidus}} \end{cases} \tag{2.9}$$

Substituting (5) into (4) yields a piecewise definition for $C_{p,eq}$, featuring a sharply increased value within the mushy zone.

This formulation is computationally efficient, as it avoids the need for an explicit latent heat source term and can be readily implemented within standard conduction solvers. The release of latent heat is naturally simulated by the enlarged heat capacity over the transition region, providing a robust solution for tracking the solid-liquid interface.

2.2. Interface tracking method

In 1969, Daly [55] introduced a way for tracking the interface using a collection of marker particles, resulting in a new advance in surface tracking technology.

The VOF (volume of fluid) is a powerful method that is used to track and locate the free surface of two immiscible fluids in a calculation mesh of Eulerian cells, which is easily extended to calculations in three dimensions. It was first reported by Hirt and Nichols in 1975 [56]. It is common to use a single value for each dependent variable that defines the fluid state in each mesh cell. We define a function "f" whose value is unity when the cell is entirely occupied by the fluid phase and zero otherwise. Therefore, the average value of f in the cell represents the fraction of the cell's volume occupied by fluid. Specifically, f=1 indicates that

the cell is full of fluid, while, f=0 means that the cell empties of fluid. While, 0<f<1 signifies the free surface, i.e. the interface between the fluid phase and the other fluids, as it is illustrated in Figure 2.1. Thus, the VOF approach only needs one storage word for each mesh cell [56]. The total fractional volume for all phases equals one.

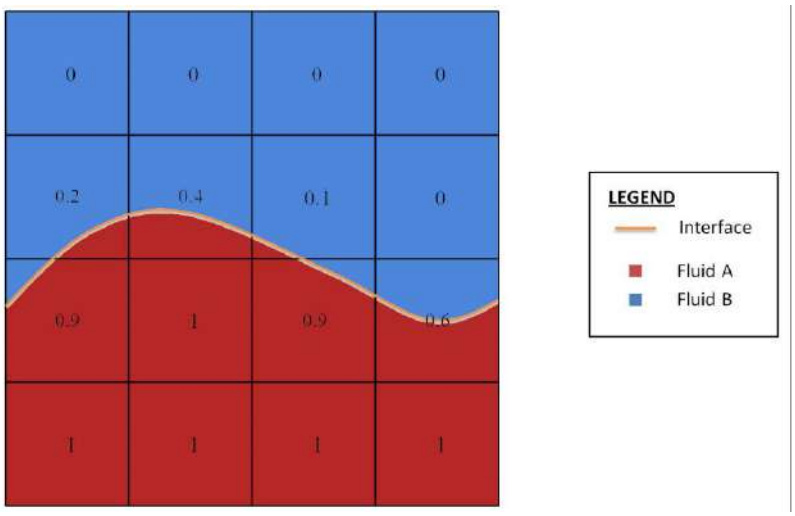


Figure 2. 1 Volume of fluid method [57]

The material properties (density ρ, viscosity μ, thermal conductivity k, etc.) in any cell are calculated as a weighted average based on the volume fraction: $\xi=\alpha\,\xi metal+(1-\alpha)\xi air$

Where ξ represents any transport property. This approach allows for a sharp representation of the interface, as illustrated in Figure 2.1, which is crucial for accurately modeling surface tension effects and heat transfer across the free surface.

In the VOF method, a set of continuity and momentum equations are solved concurrently with a volume fraction transfer equation over the computational domain [58].

The advection equation (Eq (2.10)) controls the volume fraction's temporal and spatial evolution [59].

$$\frac{df}{dt} = -\nabla.(f\,v) \tag{2.10}$$

The volume of Fluid (VOF) method can be categorized into algebraic methods and geometric methods, where each of these approaches has different ways of treating the interface between fluids. The algebraic VOF (AVOF) method uses a function to represent f, while in the geometric VOF (GVOF) method; f is represented by geometry [58].

Algebraic methods tend to be simple and do not require a complex geometry of the interface to be tracked explicitly. It uses the continuum-based partial differential equation (PDE) discretization scheme for the advection of f. In this approach, fluxes are algebraically computed; it is not necessary to recreate the interface. In contrast with AVOF approach, GVOF methods employ geometrical operations to approximate the solution of f. It aims to explicitly track the geometry of the interface between the phases. GVOF includes two steps: interface reconstruction and interface advection [58]. The piecewise linear interface calculation (PLIC) approach is an example of a geometric method [60].

In order to model the phase-change problems, a volume fraction Θ is defined in Eq 2.11 [61]. In the case of solidification of a liquid droplet, Θ tracks the transition from liquid to solid phase. The decreases of Θ from 1 to 0 indicates the progression of solidification.

$$\Theta = \begin{cases} 1 & \text{in fluid} \\ 0 < \Theta < 1 & \text{in phase change front} \\ 0 & \text{in solid} \end{cases} \tag{2.11}$$

A modified fixed velocity method is used in order to model the solidified part of the domain. In this method, a two-phase flow special case is employed, wherein the liquid phase has a volume fraction of Θ, and the solid phase has a volume fraction of (1-Θ). And the solid is treated as a liquid of zero velocity and infinite density. As it seen in Figure 2.2, cells with a value of Θ between 0 and 1, are called ‘‘partial flow cells’’ due to the fact that a portion Θ of their finite difference volume is open to flow, while (1-Θ) the remaining portion is occupied by solid region closed to flow [62].

Θ is added to the two-phase continuum model in order to modify the continuity, momentum and VOF equations, respectively as follow:

$$\nabla.(\Theta\, \mathrm{v}) = 0 \tag{2.12}$$

$$\rho\left(\frac{\partial \Theta\, \vec{v}}{\partial t} + \nabla.(\Theta\, \vec{v}\vec{v})\right) = -\Theta\, \nabla P + \Theta\, \nabla.\vec{\tau} + \Theta\, \overrightarrow{F_b} \tag{2.13}$$

$$\frac{d(\Theta f)}{dt} = -\nabla.(\Theta\, f\, v) \tag{2.14}$$

For $\Theta = 1$, these equations decrease to classical fluid flow equations. Physically, the velocity drops to zero in the front of the phase change [61].

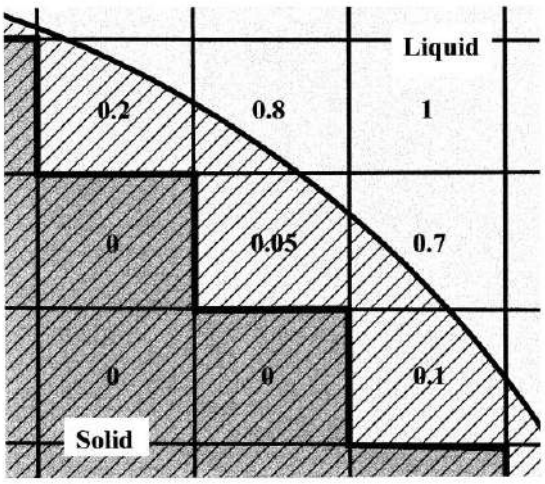


Figure 2. 2 Solidification front representations [63]

2.3. Numerical implementation and fluid-structure coupling

The governing equations were solved using the finite element method implemented within the ANSYS APDL environment. The fluid-structure interaction (FSI) between the impinging fluid (droplet) and the deformable solid substrate was modeled using a two-way coupled approach. The pressure and shear stress fields from the fluid domain are applied as loading conditions onto the structural domain (substrate). The structural response, governed by the equations of motion:

$$M\ddot{d} + C\dot{d} + Kd = F(t) \tag{2.15}$$

(Where M, C, K are mass, damping, and stiffness matrices, and d is displacement), is solved using the Finite Element Method (FEM) in ANSYS Mechanical. The resulting deformation and velocity of the substrate boundary are then fed back to update the fluid domain's boundary conditions, completing the two-way coupling. This iterative process is managed at each time step to capture the dynamic feedback between the spreading droplet and the deforming substrate.

A. Structural governing equations:

The substrate is modeled as a linear elastic solid. The conservation of momentum for the structure, also known as the elastodynamic equation, is given by [63]:

$$\rho_s \frac{\partial u_s^2}{\partial t^2} = \nabla . \sigma_s + f \tag{2.16}$$

Where:

u = displacement vector

σ = Cauchy stress tensor

ρ_s = density of the solid

f = body forces

For a linear elastic material, the stress tensor $\boldsymbol{\sigma}$ is related to the strain tensor ε by Hooke's law:

$$\sigma = \lambda\, tr(\mathcal{E})I + 2\mu_s\, \mathcal{E} \tag{2.17}$$

Where:

- λ and μs are the Lamé coefficients,
- I is the identity tensor,
- $\mathcal{E}$ is the infinitesimal strain tensor,

  $\boldsymbol{\varepsilon} = \frac{1}{2}(\nabla \mathbf{d} + \nabla \mathbf{d}^T)$

- The Lamé coefficients can be expressed in terms of the Young's modulus *E* and Poisson's ratio *ν* as:

$$\lambda = \frac{E\nu}{(1+\nu)(1-2\nu)}, \quad \mu_s = \frac{E}{2(1+\nu)}$$

B. Two-way coupling methodology:

The two-way FSI coupling is achieved by iteratively exchanging data between the fluid solver and the structural solver at each time step. The process within one time step is as follows:

Fluid-to-Structure transfer: The fluid solver computes the pressure and viscous shear stresses on the wetted surface of the substrate. These stresses are integrated to obtain the force distribution, which is then applied as a boundary condition to the structural solver.

Structural solution: The structural solver computes the deformation of the substrate under the applied fluid forces by solving Eq (2.16).

Structure-to-Fluid transfer: The updated displacements and velocities of the substrate surface are transferred back to the fluid solver. The fluid mesh is then updated to accommodate the

new boundary shape (using a dynamic mesh technique in the fluid domain). The boundary conditions for the fluid flow (no-slip or slip conditions) are updated according to the new surface velocity.

Fluid solution: The fluid equations are solved again on the updated mesh, and the process repeats until convergence within the time step is achieved.

This iterative coupling ensures that the fluid forces and the structural deformations are consistent at each time step. The convergence criterion is typically based on the change in the transferred variables (forces and displacements) between two consecutive iterations.

C. Interface coupling conditions:

At the fluid-structure interface, the following conditions are enforced:

Kinematic Continuity:

$$u_f = u_s \tag{2.18}$$

Dynamic Equilibrium:

$$\sigma_s \cdot n = \sigma_l \cdot n \tag{2.19}$$

Where:

n: unit normal vector at the interface

σ : Cauchy stress tensor

Thermal Coupling:

$$-k_f \frac{\partial T}{\partial n} = -k_s \frac{\partial T}{\partial n} \quad \text{and} \quad T_f = T_s \tag{2.20}$$

The structural equations in the solid demain are solved using the Finite Element Method (FEM).

2.4. Finite element method

The finite element (FE) method involves a systematic process to divide the domain into small elements, where physical fields (such as temperature, velocity, pressure, or displacement) are approximated using simple shape functions. Beginning in the 1970s, discontinuous piecewise

polynomial approximations were applied to solve partial differential equations numerically. This method, later called the discontinuous Galerkin method (DGM) [64].

Piece-wise approximation (Galerkin Method) was introduced by the Russian mathematician Boris Galerkin in 1915. This approach is used to capture the droplet dynamic and the formation of thin liquid layers. It improves precision even for basic approximation functions by refining the mesh and increasing the number of elements [65].

The primary steps of the FE solution approach are listed below to provide a general overview of how the FEM works [65].

1. Discretization of the domain: the initial step involves dividing the problem domain into a finite set of smaller elements. The continuous domain is converted into a mesh using a preprocessor program. The description of mesh consists of nodes which are defined at the element boundaries and element connectivity.

2. Selection of interpolation: the field variables within each element are interpolated over the element with interpolation functions. Linear, quadratic, and cubic polynomials are often used for interpolation functions.

3. Determination of element properties: to determine the element properties, it is essential to develop the matrix equation for the finite element that links the unknown function's nodal values to other parameters. It uses variational principles and the governing equations' weak form (such as Galerkin method).

4. Assembly of the global system: to obtain the global system of equations, all element equations must be assembled while maintaining the connectedness between elements and nodes. Boundary conditions not incorporated within the element equations, should be enforced before solution.

5. Solution of the global system, solve the global equation system using appropriate numerical solvers. The solution returns the nodal values of the specified function.

6. Compute additional results: compute additional parameters, such as strains, stresses, and structure deformation in mechanical problems.

Formulation of finite element equations:

If the problem's physical formulation is referred to as a differential equation, the Galerkin method is the most often used finite element formulation technique. It is one of the most powerful numerical method for solving partial differential equations. It relies on expressing the solution as a linear combination of predetermined basis functions. Whereas variational formulation of the finite element equations is employed for the physical problem, that can be expressed as the minimization of a functional [65].

A. Galerkin method

The basic idea of the Galerkin finite element method will be demonstrated on the following second order linear BVPs (boundary value problem). The general formulation of the problem is defined as [66]:

$$-\frac{d}{dx}\left(p(x)\frac{dv}{dx}\right)+q(x)\,v(x)=\ f(x), \qquad a\le x\le b \tag{2.21}$$

Whose boundary conditions (Dirichlet condition and Neumann condition) are as follow:

$$\mathrm{u(a)}=\mathrm{r}_1 \qquad \left(p(x)\frac{du}{dx}\right)_{\mathrm{x=a}}=\tau_1 \tag{2.22}$$

$$\mathrm{u(b)}=\mathrm{r}_2 \qquad \left(p(x)\frac{du}{dx}\right)_{\mathrm{x=b}}=\tau_2 \tag{2.23}$$

Domain Discretization: the domain [a,b] is divided into elements of equal (not necessary) length.

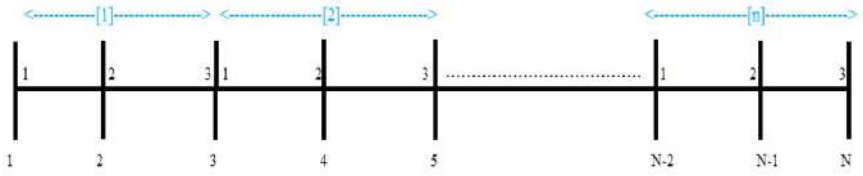


Figure 2.3 Domain Discretization for Quadratic Shape Function [67]

The approximate solution $\tilde{u}(x)$ within each element is expressed as:

$$\tilde{u}(x)=\sum_{j=1}^{n} a_j\,\emptyset_j\,(x) \tag{2.24}$$

x represents the independent variable in the problem, $\emptyset_j(x)$ define the trial functions.

The coefficients a_j are being determined.

The governing equation residual for typical element (e) is minimized in a weighted sense in the domain:

$$\int_{[e]} \left[-\frac{d}{dx}\left(p(x)\frac{d\ddot{u}}{dx}\right) + q(x)\ddot{u}(x) - f(x) \right] \phi_i(x)dx = 0 \qquad (2.25)$$

a⩽ x⩽ b

Reducing the order of derivatives by integrating the term $-\frac{d}{dx}\left(p(x)\frac{du}{dx}\right)$. After simple modification, we obtain the following form:

$$\sum_{j=1}^{n} a_j \int_{[e]} \left[p(x)\frac{d\phi_i}{dx}\frac{d\phi_j}{dx} + q(x)\phi_i\phi_j \right] dx = \int_{[e]} f(x)\,\phi_i(x)dx - \left[-p(x)\frac{d\ddot{u}}{dx}\phi_i \right]_{[e]} \qquad (2.26)$$

This may be written in the conventional matrix form as:

$$\left[K^{[e]}\right]\{a\} = \left\{F^{[e]}\right\} \qquad (2.27)$$

The derivation of the element stiffness matrix and the element load vector is given follow:

$$K_{i,j}^{[e]} = \int_{[e]} \left[p(x)\frac{d\phi_i}{dx}\frac{d\phi_j}{dx} + q(x)\phi_i\phi_j \right] dx \qquad (2.28)$$

$$F_{i,j}^{[e]} = \int_{[e]} f(x)\,\phi_i(x)dx - \left[-p(x)\frac{d\ddot{u}}{dx}\phi_i \right]_{[e]} \qquad (2.29)$$

The assembly process combines all element stiffness matrices and load vectors in order to form the global stiffness matrix and global load vector (Eq (1.30)). By solving this system of equations, we will find the values of a_j. The piece-wise polynomial for each element will then be obtained by putting these values into Eq (1.24).

$$\begin{bmatrix}
K_{1,1}^1 & K_{1,2}^1 & K_{1,3}^1 & 0 & 0 & 0 & 0 & 0 & 0 & 0 \\
K_{2,1}^1 & K_{2,2}^1 & K_{2,3}^1 & 0 & 0 & \vdots & \vdots & \vdots & \vdots & \vdots \\
K_{3,1}^1 & K_{3,2}^1 & K_{3,3}^1+K_{1,1}^2 & K_{1,2}^2 & K_{1,3}^2 & \vdots & \vdots & \vdots & \vdots & \vdots \\
0 & 0 & K_{2,1}^2 & K_{2,2}^2 & K_{2,3}^2 & \vdots & \vdots & \vdots & \vdots & \vdots \\
\vdots & \vdots & K_{3,1}^2 & K_{3,2}^2 & K_{3,3}^2+K_{1,1}^3 & 0 & 0 & \vdots & \vdots & \vdots \\
\vdots & \vdots & 0 & 0 & 0 & \ddots & \ddots & \vdots & \vdots & \vdots \\
\vdots & \vdots & \vdots & \vdots & \vdots & \ddots & \ddots & 0 & 0 & 0 \\
\vdots & \vdots & \vdots & \vdots & \vdots & \vdots & 0 & K_{3,3}^{n-1}+K_{1,1}^n & K_{1,2}^n & K_{1,3}^n \\
\vdots & \vdots & \vdots & \vdots & \vdots & \vdots & \vdots & K_{2,1}^n & K_{2,2}^n & K_{2,3}^n \\
0 & \dots & \dots & \dots & \dots & 0 & 0 & K_{3,1}^n & K_{3,2}^n & K_{3,3}^n
\end{bmatrix}
\begin{bmatrix} a_1 \\ a_2 \\ a_3 \\ \vdots \\ \vdots \\ \vdots \\ \vdots \\ \vdots \\ a_{N-1} \\ a_N \end{bmatrix}
=
\begin{bmatrix} F_1^1 \\ F_2^1 \\ F_3^1+F_1^2 \\ F_2^2 \\ F_3^2+F_1^3 \\ \vdots \\ \vdots \\ F_3^{n-1}+F_1^n \\ F_2^n \\ F_3^n \end{bmatrix} \qquad (2.30)$$

B. Variational formulation

Variational methods are a type of optimization method. The strong variational formulation is created by combining governing differential equations and initial/boundary conditions [67]. Higher solution smoothness is required for this approach to work directly with the governing equations. While the weak form allows the use of basic functions that only need continuity, not smoothness.

Conclusion

In summary, this chapter presents the numerical framework applied to model the impact and deposition of droplet on a solid substrate. The droplet motion was captured using the VOF approach, while the FEM solves the equations numerically. In the FSI modeling, the governing equations were solved to investigate key parameters of the thermal spraying process, such as droplet velocity, temperature, and substrate properties, which are discussed in the following chapters.

Chapter 3

Numerical simulation of molten droplet deposition

This chapter presents the numerical simulation results of droplet deposition on a solid substrate. The simulation was conducted using the ANSYS software, in accordance with the methodology described in Chapter 2. Single and multiple droplet impact investigations were carried out in this study to examine the key parameters influencing droplet dynamics and the final lamella shape, as well as to analyze the droplet behavior in the presence of an oxide layer on the substrate.

Introduction

Numerical simulations of the impact and deposition of single and multiple droplets on a solid substrate are conducted in this chapter. Various factors are considered, such as impact velocity and the molten state of droplet. In addition to the substrate surface condition.

To investigate the transient process of Al droplet impacting a stainless-steel substrate, a two-dimensional model was developed using ANSYS APDL software. Figure 3.1 presents the computational domain, which consists of a substrate with dimensions of 3 mm × 40 mm and an impacting droplet with a diameter of 3.92 mm.

In addition, the boundary conditions are defined as follows: the substrate is structurally constrained (i.e., no displacement is allowed at the substrate boundaries, Ux=0 and Uy=0), the fluid-structure interaction (FSI) describes the coupling between the fluid and solid domains (Figure 3.1). The simulation setup was characterized by an initial droplet velocity of 3 m/s, a temperature of 630°C, and a substrate maintained at 200°C. Gravitational effects were included in the model.

To ensure the reliability of the developed model, this chapter first presents a validation study based on the experimental work of Xue et al [33], before proceeding to the subsequent analyses. Since the results exhibit a good agreement with the experimental findings, the validated model was subsequently used to simulate multiple droplet impacts, both successive and simultaneous, by varying the vertical and horizontal spacing between droplets. The investigation also considered the effect of impact velocity and droplet fusion state on the deposition mechanism and the lamella morphology. The chapter concludes with an analysis of the effect of the oxide layer on the substrate surface.

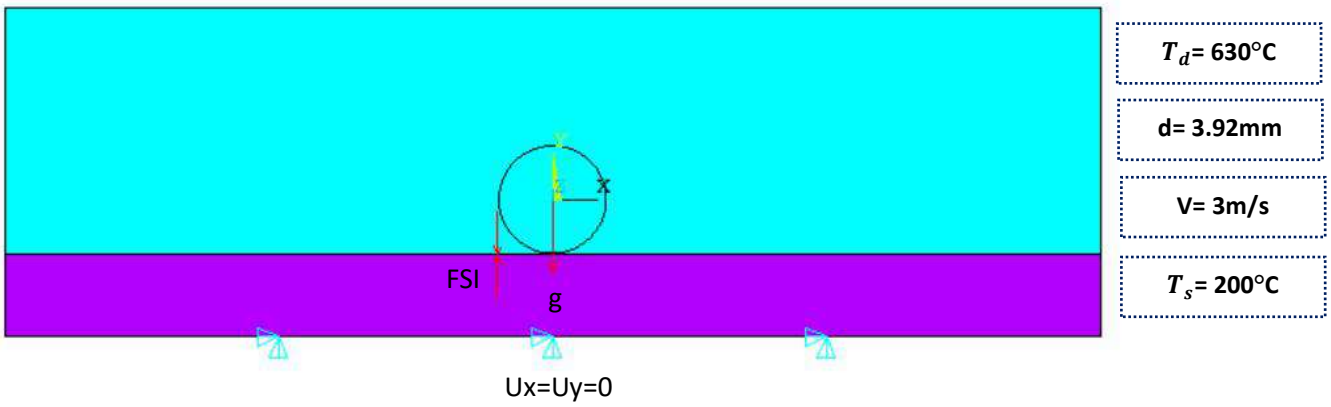


Figure 3. 1 Computational domain of droplet impact on solid substrate

3.1. Model Validation

The first section of the study involves the validation of the numerical model via a comparison between the simulation results and the experimental results of Xue et al [33]. Figure 3.2 represents the outcomes of a 3.92mm aluminum alloy droplet impacting a stainless-steel substrate with velocity of with 3m/s. The initial temperatures of the droplet and the substrate were set at 200°C and 630°C (higher than the melting temperature of aluminum alloy), respectively. The thermophysical properties of the materials are listed in Table 3.1.

Table 3.1 Properties of the materials used [33]

Properties	Aluminium Alloy	Steel H13	unity
Density	2570	7800	(Kg/m^3)
Viscosity (liquid)	°c 200 1500 250 1000 300 600 350 310 400 160 450 70 500 10 550 0.1 575 0.00103 600 0.00101 630 0.001	-	(m^2/s)
Liquid thermal conductivity	70	-	(W/m K)
Liquid specific heat	1000	-	(J/Kg K)
Solid thermal conductivity	°c 400 144 500 147 630 70	°c 27 17.6 427 25.1 649 26.8	(W/m K)
Solid specific heat	°c 100 400 300 500	°c 20 460 200 502	(J/Kg K)

	400 800 570 1050 580 1038	500 550	
Young's Modulus (E)		200	GPa
Poisson's ratio		0.3	

The simulation results of the droplet impact and spreading represented in Figure 3.2 indicate that the droplet starts to spread over the substrate at t= 0.1ms. During this process, heat is transferred from the hot droplet to the cooler substrate. At 7ms, the droplet attains its maximum spreading diameter and subsequently begins to cool. Solidification first occurs at the droplet edges, restricting the liquid flow and resulting in the formation of raised rims. As the droplet solidifies completely, aluminum splat forms on the substrate surface. The droplet's dynamic behavior and final shape seem to be similar to the results found by Xue et al [33] under the same set of conditions [68].

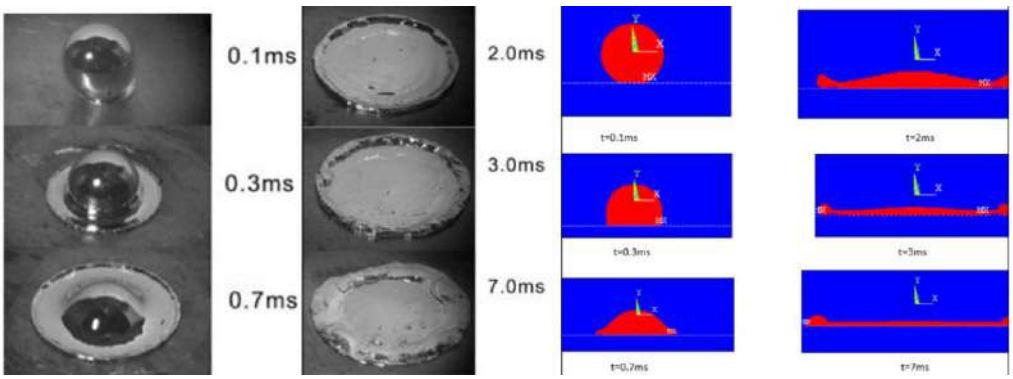


Figure 3. 2 Deposition of molten Al droplet on a solid substrate. (a) Experiment of reference [33] (b) Simulation results

The evolution of the spread factor ($\zeta = d/d_0$) over time is illustrated in Figure 3.3. This factor is defined by normalizing the splat diameter d measured from simulation results by the initial particle diameter d_0. The evolution of the spread factor reveals a good agreement of our results and the outcomes of Xue et al [33] . However, there is a slight discrepancy between the results; this could be elucidated by the numerical model limitations used in this study.

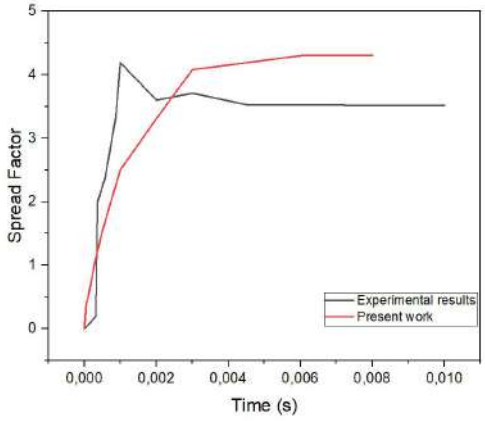


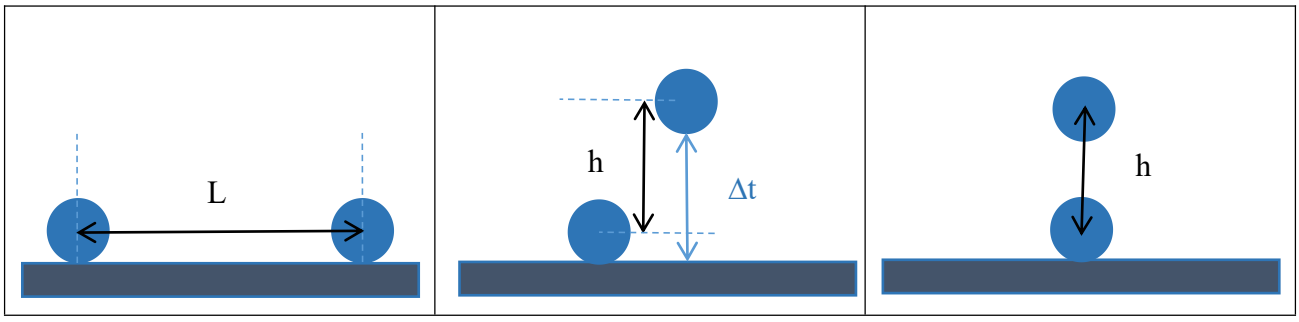
Figure 3. 3 Evolution of the spreading factor: comparison between the experimental results of [33] and the simulation results of the present study.

3.2. Results and discussion

3.2.1. The effect of droplet spacing

The phenomenon of multi-droplets impact on solid substrate is a complex aspect, yet crucial in thermal spraying processes. As it can involve interactions between the droplets as well as the interactions of each droplet with the substrate. Thus, understanding these interactions during splat formation is necessary for improving coating efficiency. Table 3.2 shows three scenarios of multi-droplets impact on a steel substrate. To begin, we consider two identical molten Al droplets colliding with the substrate at the same time, with changing the offset center (L) between droplets. Secondly, the non-simultaneous impact of the droplets is investigated, with varying vertical distances (h) (or time separation). Finally, the successive impact of the droplets is studied. These studies were conducted to achieve a deeper understanding of the effect of changing the impact distance between binary droplets on their interactions and on the formation of the metallic lamella.

Table 3.2 Droplets deposition: **(a)** simultaneously **(b)** non-simultaneously **(c)** successively



(a)	(b)	(c)
Simultaneous	Non-simultaneous	Successive
L≠0	L≠0	L=0
h= 0	h≠0	h≠0
Δt=0	Δt≠0	Δt≠0

A. Simultaneous impact of droplets

Figure 3.4 depicts the behavior of binary Al droplets impacting a stainless-steel substrate with the same velocity of 3 m/s. The distance (L) between the centers of these particles was varied from 6 mm to 9 mm. The findings show that the spreading tendency is consistent across all cases. However, the timing of the first interaction between the two droplets increases with the distance between their centers. This means that the greater the distance between the droplets, the longer it takes for them to interact. A jet of material is observed at the impact point; forming a central vertical sheet. This jet results from the strong inertial momentum. At high Weber number ($We \gg 1$), surface tension plays a secondary role, permitting the formation of this jet. This phenomenon is particularly visible at later times (e.g., at t = 3 ms and t = 7 ms). The sides of the resulting splat continue to spread across the substrate, unaffected by the central jet of material, indicating that radial spreading is primarily governed by the inertia of the droplets. After 7 ms, the ejection of secondary droplets was observed (splash phenomenon). This is due to the onset of solidification around the edges of the splat, which disrupts the flow of the expanding liquid and causes the fragmentation of the material into smaller droplets. For the case of L=6 mm, the jet is less pronounced. The jetting continues to retract over time and becomes thicker as the surface tension force overcomes the kinetic energy, eventually stabilizing into a thin film on the substrate. As the distance between the droplets increases (L = 7 mm, 8 mm, and 9 mm), the central jet becomes more visible and more extended. However, the thickness of the lamella gradually decreases, suggesting that the kinetic energy is more dissipated in the central jet rather than in radial spreading.

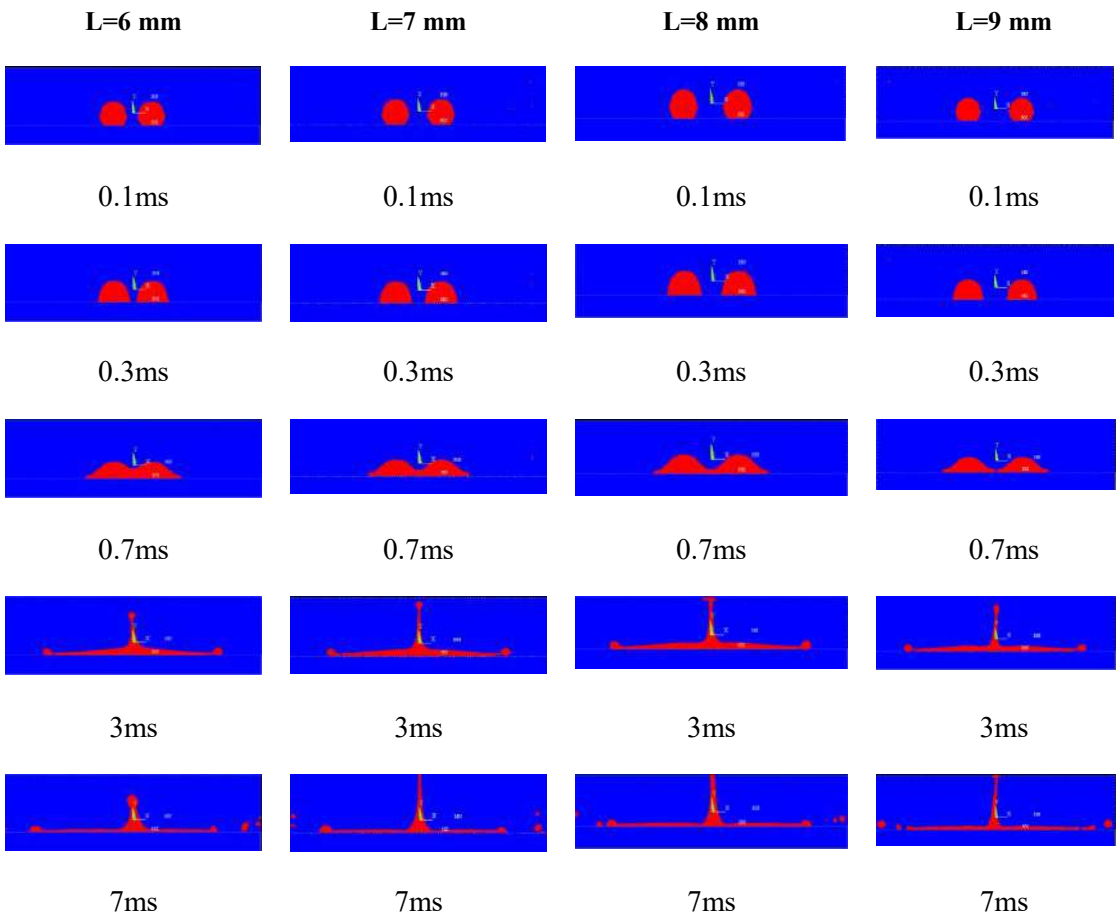


Figure 3. 4 Impact of dual aluminum droplets simultaneously with changing the spacing between the droplets

B. Non simultaneous impact of droplets

This section examined non-simultaneous Al droplets impingement for different time intervals (or different vertical spacing), which means that each droplet impacts the substrate at different times. In the prior study of simultaneous droplet impact, if solidification occurs before complete spreading, the upward sheet results in an uneven layer surface, leading to a no uniform coating. Therefore, to study the non-simultaneous impact, the offset distance was fixed to 6 mm (corresponding to the smaller uprising sheet´s high).

Figure 3.5 illustrates the simulation results for non-simultaneous droplet impact with varying time separations (Δt= 0.3ms, Δt= 0.7ms and Δt= 1ms). As the droplets first collide the substrate, they spread rapidly due to the effect of kinetic energy (high We and Re numbers). At 3ms, the interaction of adjacent droplets produces an ascending jet that extends from the main droplet body, as observed with simultaneous impact. However, as the time interval between the impacts of the two droplets increases, the maximum values of the liquid sheet decrease, and their deviation increases. After a few milliseconds, this sheet breaks up into smaller droplets due to Rayleigh-Plateau instability [69], producing splashes. The upward

ejection of fluid decreases due to the dissipation of kinetic energy over time. After 10.7 ms, the final morphology of the lamella becomes more flatter, closely resembling a circular disk, and similar to that observed in single droplet impacts. However, the surface of the formed layer remains non-uniform.

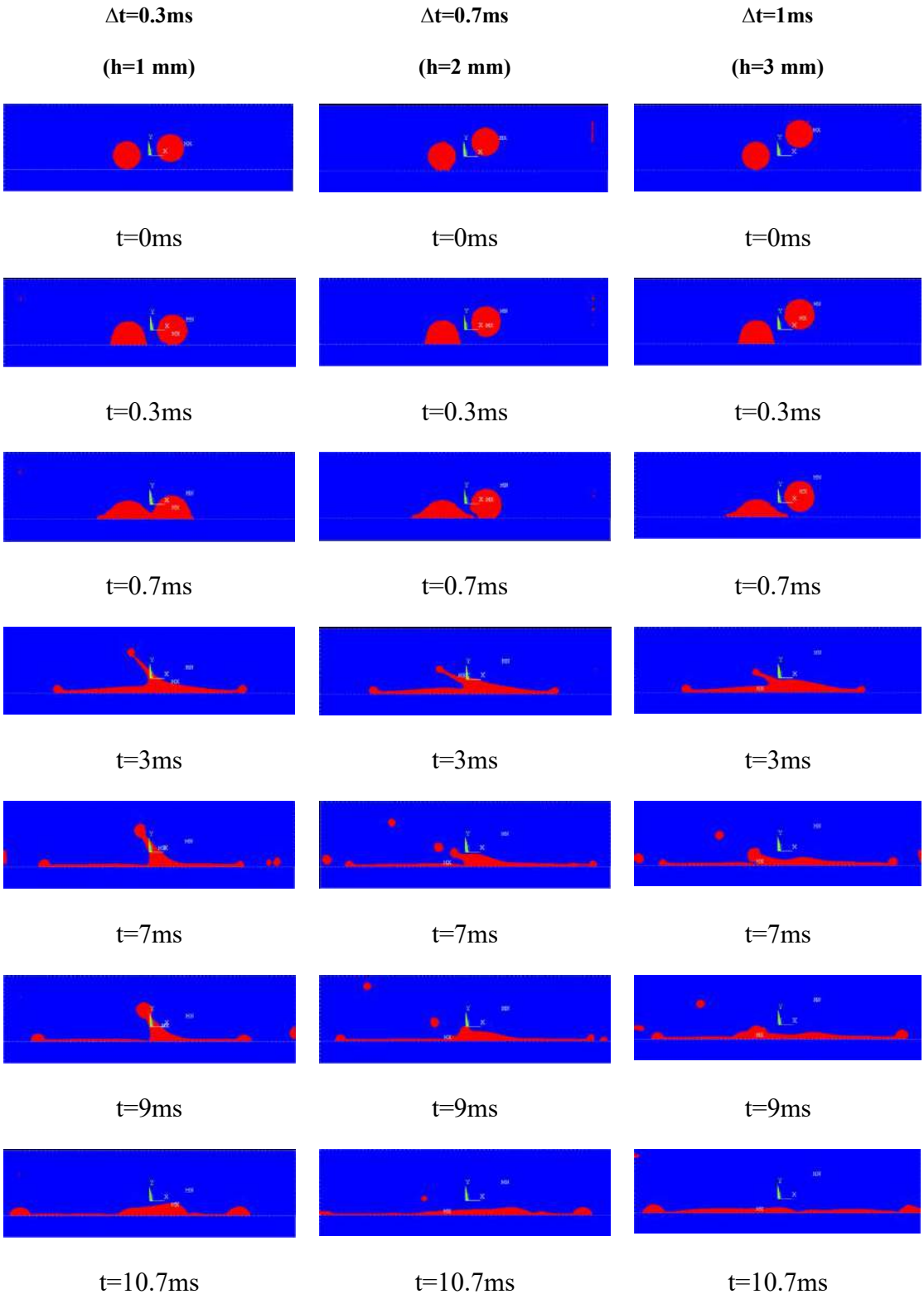
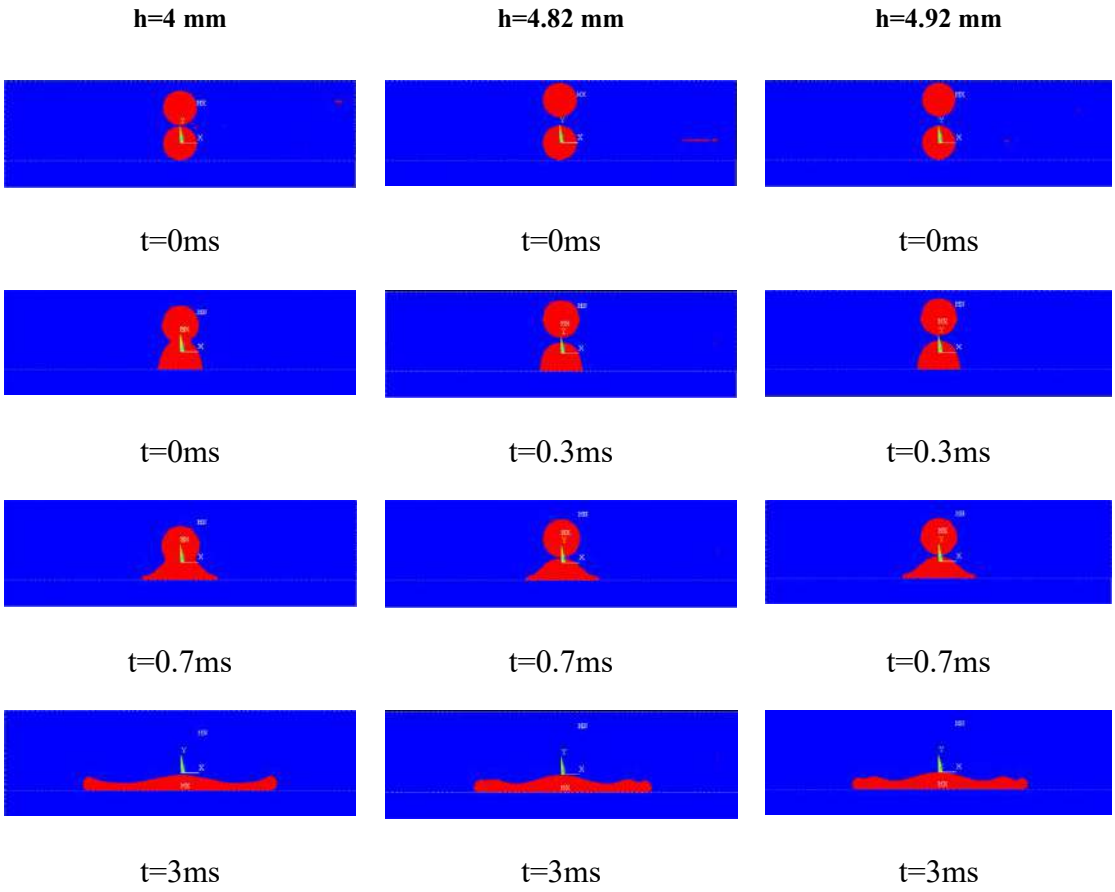
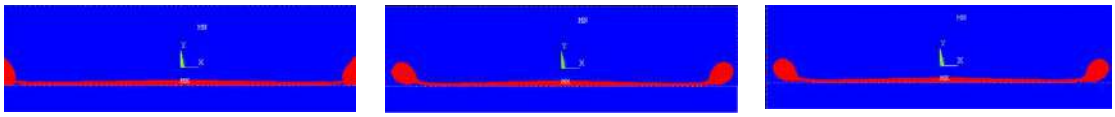


Figure 3. 5 Non simultaneous impact of dual Al droplets

C. Successive impact of droplets

The droplets morphology during the successive impact is illustrated in Figure 3.6. All the different cases of height (h) exhibit similar spreading behavior. After the impact of a new droplet, it merges smoothly with the already deposited droplet. The spreading is then governed by the combined kinetic energy of the two droplets. At the end of spreading, the formed splat is shaped as 'semilunar' with thick rims. It can be observed that gaps were created at the interface (at the splat boundary); due to the air entrapment, these gaps may disappear with increasing the impact velocity [70]. In addition, the spreading rate decreases with the increase of vertical distance between the droplets, in contrast to the non-simultaneous impact (successive impact with L>0). Generally, as the droplets impact at the same location, increasing the time interval between impacts allows the first droplet more time to spread and dissipate its kinetic energy before the second droplet arrives. However, this is not evident in this study because of the small difference in time spacing. Therefore, the evolution of the droplet morphology at different time intervals for three different drop heights (h=4 mm, h=4.82 mm, and h=4.92 mm) indicates that the shape and spreading of the droplets vary over time, with a tendency to form raised edges and cavities due to air entrapment.





t=7ms t=7ms t=7ms

Figure 3. 6 Successive impact of dual Al droplets

D. Temperature distribution

The temperature distribution of Al droplet during its deposition onto a substrate is controlled by the heat transfer at the droplet/substrate interface. When multiple droplets impact the substrate simultaneously, the thermal zones overlap, leading to a temporary concentration of thermal energy between the droplets. This localized heating delays solidification, an effect that can be interpreted in terms of the Stefan number. In contrast, during successive impacts, each droplet arrives at a different time, thus, the new droplet collides a surface that has been preheated by earlier impacts. This results in a dynamic temperature distribution, with a temporary increase in temperature at the interface between the droplets before it gradually decreases as spreading continues.

To better understand these phenomena, we conducted a comparison of the temperature distribution between the impact of binary droplets (simultaneous and successive) and single droplet impact, as displayed in Figure 3.7.

As the droplet impacts the substrate, its kinetic energy is converted into viscous dissipation and surface tension. Upon contact, heat is transferred from the droplet to the substrate surface, leading to droplet cooling. Therefore, the droplet bottom solidifies and adheres to the substrate, followed by solidification that progresses upward from the bottom to the top of the droplet [71].

During the successive droplet deposition, before entirely solidifying, the second droplet comes into contact with the first, leading to an increase in temperature at the interface, then it gradually decreases as spreading progress.

The same thermal behavior was observed when the droplets impact the substrate simultaneously. As they interact, there is a temporary rise of temperature due to the concentration of thermal energy at the meeting region of these droplets. Over time, a solidified layer develops at the droplet/substrate interface. Finally, it is worth noting that the temperature at the edges remains higher in all cases because of the poor thermal contact between the droplet rim and the substrate, leading to less effective heat conduction.

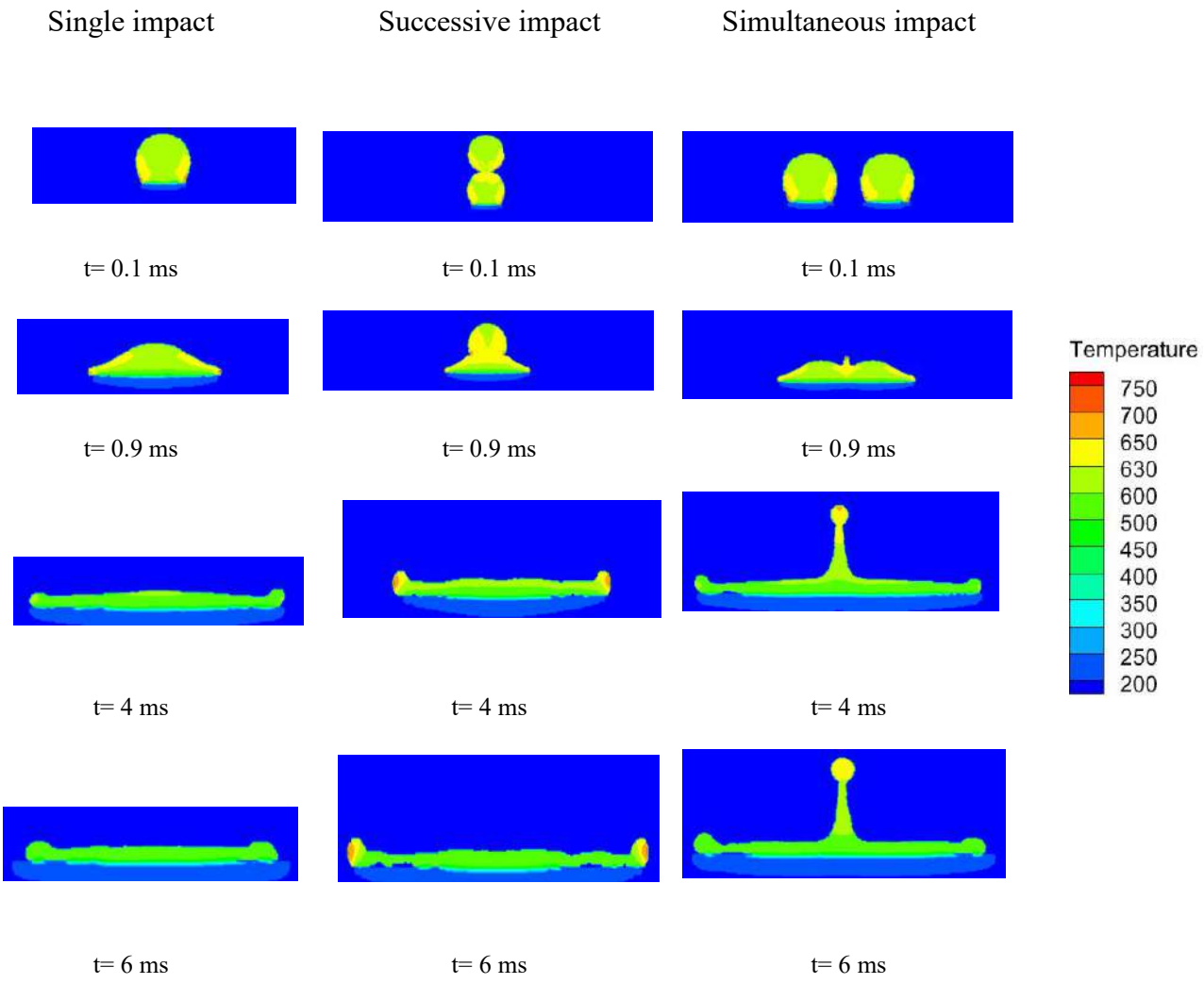


Figure 3. 7 Temperature distribution of single and binary droplets at different time intervals

E. Radial velocity distribution

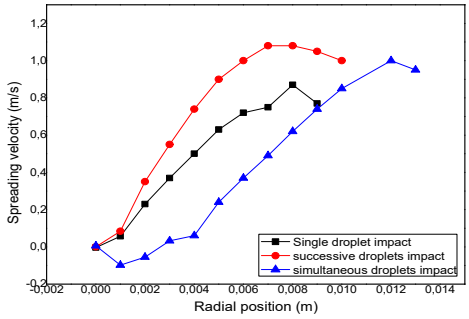
Figure 3.8 shows the evolution of the radial spreading velocity over time. The difference in the radial velocity between single, successive, and simultaneous impact provides critical insight into the dynamics that govern lamella formation and how phase change fundamentally modifies the governing energy balances.

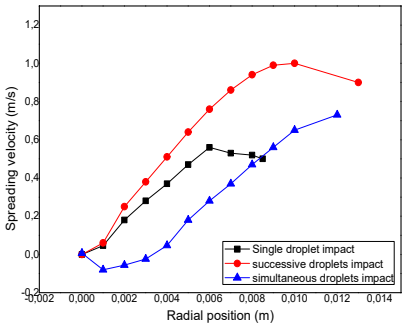
It can be observed that the spreading velocity increases in the radial direction, where the inertial forces drive the liquid to spread outward radially, followed by a deceleration. This decay is a direct signature of solidification induced viscosity increase and the growth of a solid rim at the contact line.

In successive impact, the increase in fluid amount results in greater momentum compared to a single droplet. The second droplet impacts a substrate already thermally affected by the first impact, resulting in a reduced local quenching capacity, allowing a greater portion of the

kinetic energy to remain in the liquid phase, thereby sustaining radial flow. This phenomenon is analogous to the re-melting effect observed in sequential multi-droplet deposition, in which the initial deposit acts as a thermal buffer, prolonging the liquid phase and promoting enhanced spreading.

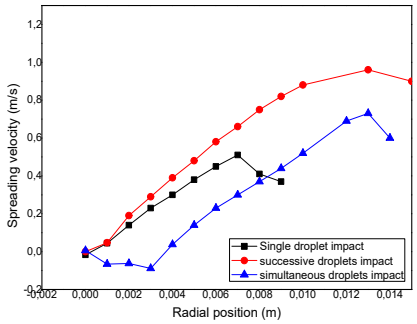
While in the simultaneous impact, a lower spreading velocity is observed. When two expanding lamellae meet, their radial momentum is not simply additive. Instead, the collision creates a vertical stagnation line, converting horizontal kinetic energy into upward jetting. The observed negative velocities signify a local radial pressure gradient reversal, driving flow back toward the impact axis, a phenomenon documented in studies of droplet coalescence on surfaces. In all cases, a reduction in velocity is observed as the droplets cool and solidify.

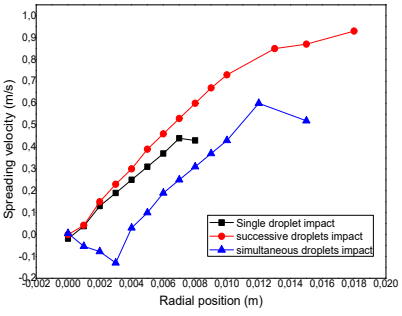




t= 3ms

t= 4ms





t= 5ms **t= 6ms**

Figure 3. 8 The evolution of spreading velocity with the radial position

F. Pressure distribution

The temporal evolution of the impact pressure, presented in Figure 3.9, provides a direct measurement of the momentum transfer governing splat formation and adhesion. The results indicate that the pressure evolution depicts the same behavior in each case. The droplet produces a high pressure at the impact, then it gradually decreases. This pressure profile is a classic signature of liquid droplet impact. The initial peak aligns with the theoretical water-hammer pressure [53]. The subsequent rapid decay signifies the transition to an incompressible hydrodynamic regime, where pressure relaxes as the flow expands radially and kinetic energy is redistributed into viscous dissipation and surface energy. During solidification, this decay is accelerated due to the rapid increase in effective viscosity and the momentum sink created by the growing solid phase.

In the case of successive impact, the pressure is significantly higher compared to a single droplet; this cannot be attributed to simple momentum addition alone. The first droplet heats the substrate, reducing the rate of solidification for the second droplet. This maintains a larger liquid volume in contact with the substrate for a longer duration, sustaining the hydrodynamic pressure. Furthermore, when the time interval between successive impacts is shorter than the pressure relaxation time, the compressive wave from the second impact can constructively interfere with the residual stress field from the first, leading to a cumulative pressure load.

A higher impact pressure promotes a good droplet/substrate adhesion. The initial high-pressure leads to intimate contact formation, minimizing voids and optimizing thermal conduction.

In summary, in successive impacts, the interval must be optimized; too short an interval leads to the beneficial pressure superposition, while too long an interval allows the substrate to cool, reverting to single-impact mechanics.

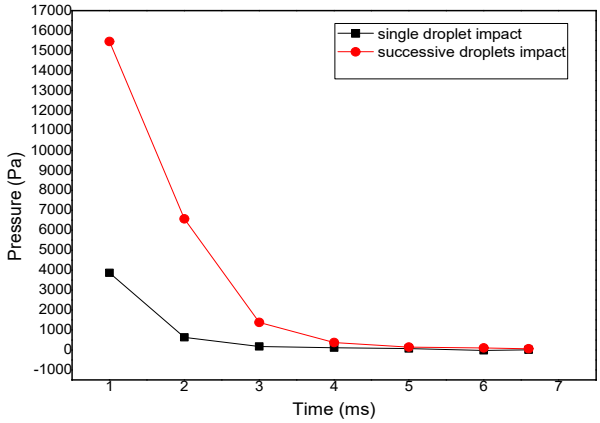


Figure 3. 9 The evolution of pressure over time

3.2.2. The effect of impact velocity

The effect of impact velocity on droplet spreading, spreading rate, pressure evolution, and temperature distribution will be investigated in this section. Furthermore, the interactions between successive droplets will be analyzed to elucidate their mutual influence.

A. Successive impact of Al droplets

Figure 3.10 compares the final splat diameter of successive impact at different velocities (Vy=3m/s, Vy=5m/s, and Vy=7m/s). It can be observed that the maximum value of splat diameter reached after 2.2 ms for 3 m/s is attained only after 1.2 ms and 0.8 ms for the velocities of 5 m/s and 7 m/s, respectively. This indicates that high impact velocities result in a significant spreading rate, because the kinetic energy exceeds the surface tension and viscosity forces. Moderate increases in splat diameter due to higher impact velocity can enhance surface coverage, reducing the amount of fluid required to achieve a uniform coating.

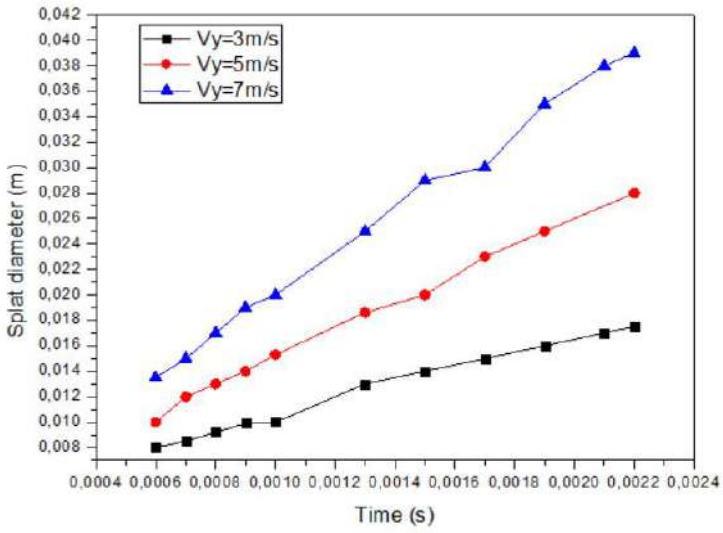
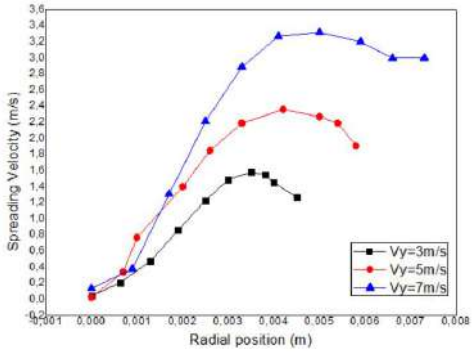


Figure 3. 10 Comparison of splat diameter during successive impact of droplets at different impact velocities

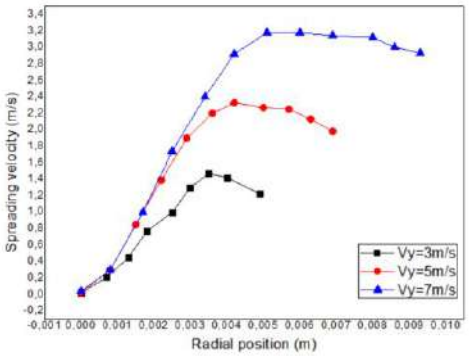
Figure 3.11 illustrates the variation of the spreading velocity (V_x) along the substrate x-direction for different impact velocities at various time instants (t=0.7ms, t=0.9ms, t=1ms, and t=2ms). At the point of impact, the spreading velocity is lower because the motion is vertical on the substrate, then the droplet's initial kinetic energy drives the spreading radially, leading to an increase in the spreading velocity. This increase continues until the kinetic energy dissipates through viscous forces and surface tension.

In addition, a high impact velocity produces a high spreading velocity because of the stronger inertial forces acting during the early stage of spreading. It can be noticed that the spreading velocity decreases over time, since viscous forces resist further motion and spreading of the fluid, as well, surface tension acts as a restoring force and pulls the fluid back toward a spherical shape.

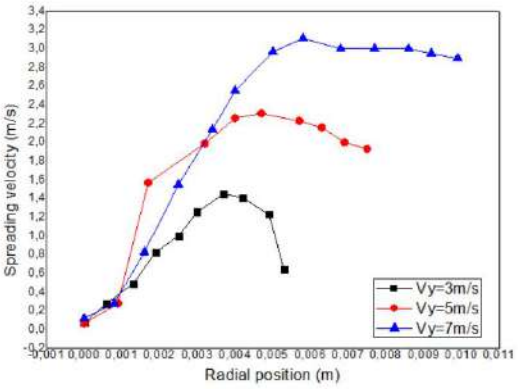
Following that, the pressure dynamics were examined in Figure 3.12. The pressure variation is closely linked to the impact velocity. Upon initial impact, the droplet generates a strong pressure pulse, producing a sharp peak at the contact point; this peak is more pronounced at higher impact velocities. Following the impact, the droplet passes from the inertial-dominated regime to the viscous-dominated regime [72,48] . Once the droplet stops spreading, the internal pressure becomes nearly uniform and tends toward zero.



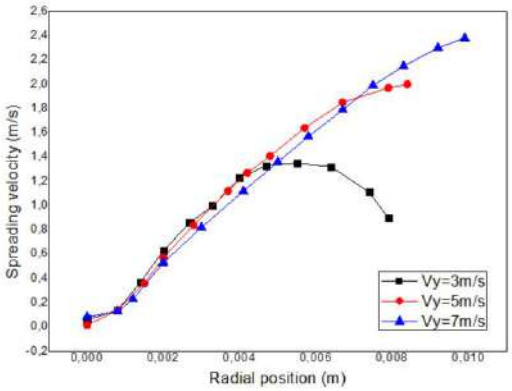
t=0.7ms



t=0.9ms

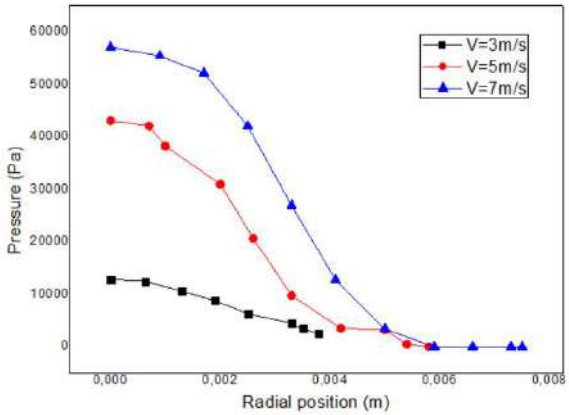


t=1ms

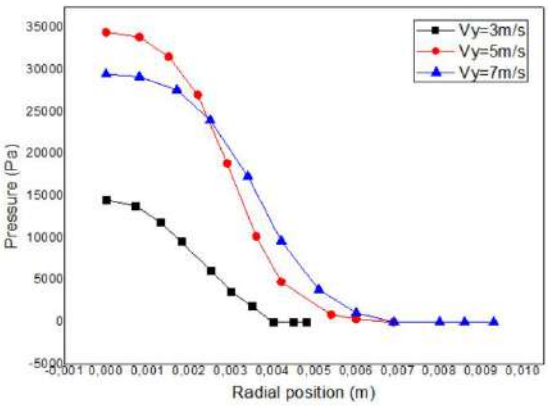


t=2ms

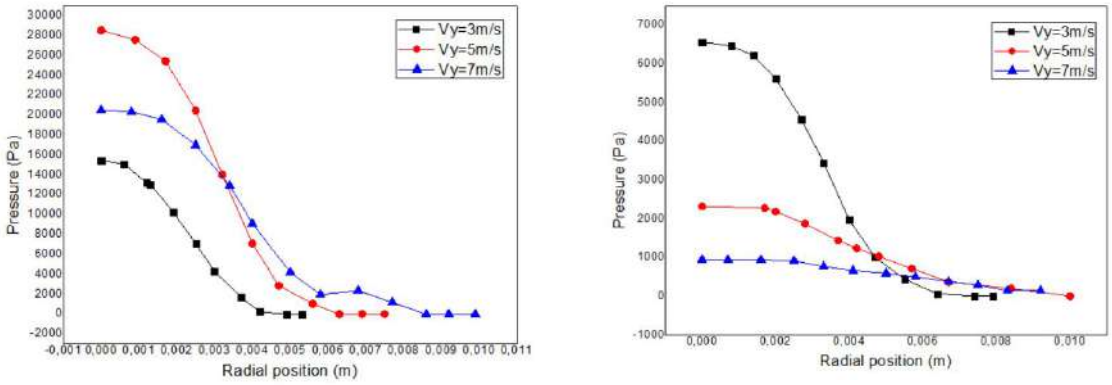
Figure 3. 11 The evolution of spreading velocity with the radial position for different impact velocities



t=0.7ms



t=0.9ms



t=1ms **t=2ms**

Figure 3. 12 The evolution of pressure with the radial position for different impact velocities

The impact velocity effect on the temperature distribution inside the droplet is also investigated (Figure 3.13). Heat transfer between the droplet and the substrate occurs immediately after impact, affected by the temperature difference. As successive droplets impact, their interaction results in localized heat, where a thermal boundary region is developed. The area in contact with the substrate cools rapidly; this can be attributed to the rapid droplet/substrate heat transfer. While the droplet's edges maintain a higher temperature for all impact velocities, since they are not fully in contact with the substrate.

It is evident that the temperature distribution inside the droplet is affected by the initial impact velocity. At higher impact velocities, the droplet possesses greater kinetic energy, which is converted into intense radial flow upon impact. The rapid spreading enhances heat transport inside the molten droplet and increases droplet/substrate contact area. In contrast, at lower impact velocities, the reduced inertial forces resulting limited spreading, which confines the thermal field near the impact center. As a result, the heat remains more localized, and the temperature gradients are steeper. These observations indicate that the impact velocity controls the coupling between hydrodynamic spreading and thermal diffusion.

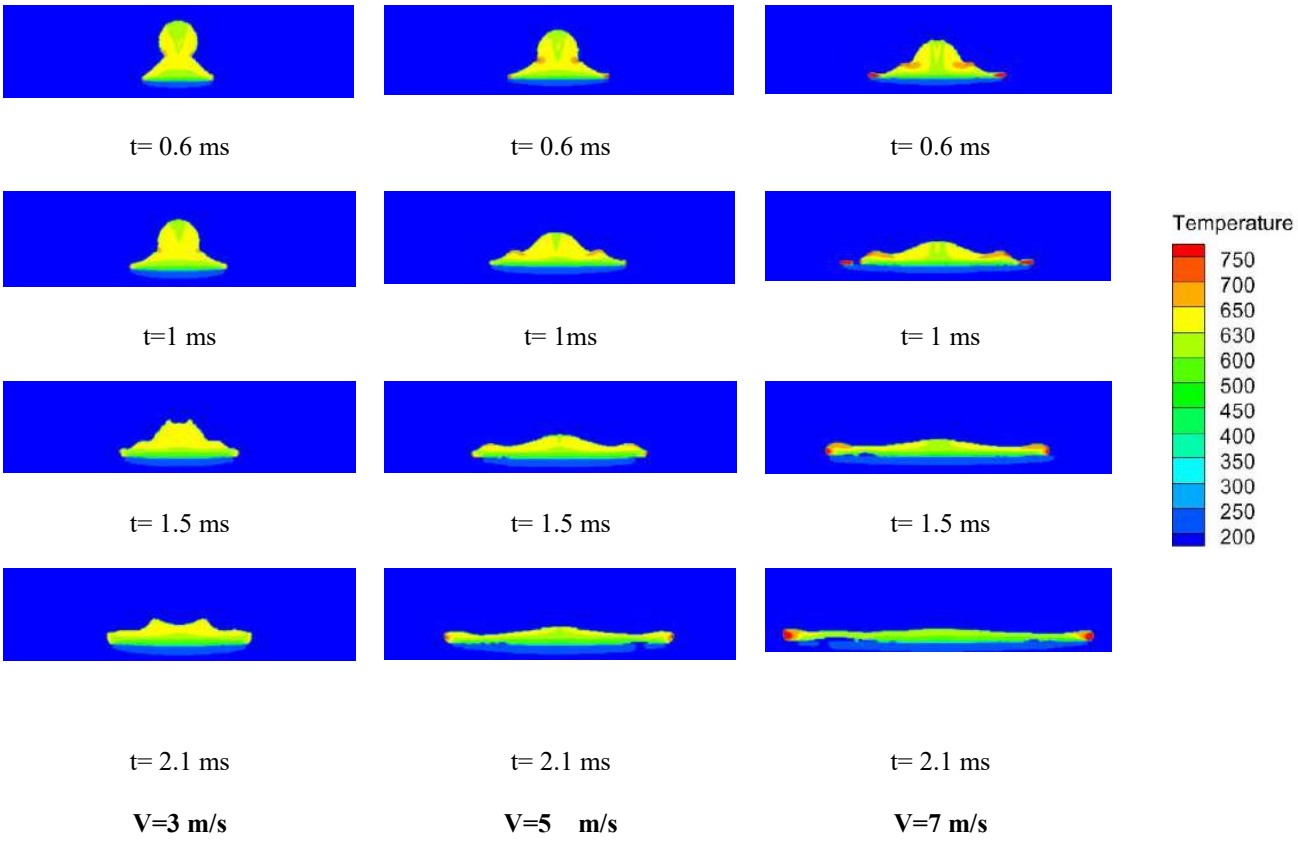


Figure 3. 13 The temporal variation of temperature corresponding to various impact velocities

B. Simultaneous impact of Al droplets

In this section, we repeat the previous simulation while focusing on simultaneous impacts. Beginning with the spreading dynamics, Figure 3.14 illustrates a comparative assessment of the diameter of the resultant splats from simultaneous impact of droplets, at three distinct initial velocities (Vy=3m/s, Vy=5m/s, and Vy=7m/s).

For all velocities, the diameter increases linearly in the early stages, indicating that inertia is the dominant force, and the liquid is spreading freely. It can be observed that at any given time, the 7 m/s droplet has a significantly larger diameter compared to the 5 and 3 m/s droplets. As previously discussed, significant kinetic energy arises from increased impact velocity, leading the droplets to spread more extensively upon impact, thus, an increase in splat diameter. As time progresses, the spreading rate gradually slows down as viscous forces overcome the remaining inertial momentum of the molten droplet, eventually approaching a stable value corresponding to the final splat morphology.

Furthermore, the coalescence of simultaneous droplets results in a greater increase in splat diameter compared to the fusion of sequential droplets (Figure 3.10). Since the interaction

between the spreading edges of the two droplets can result in additional outward momentum transfer, it consequently enhances the overall spreading.

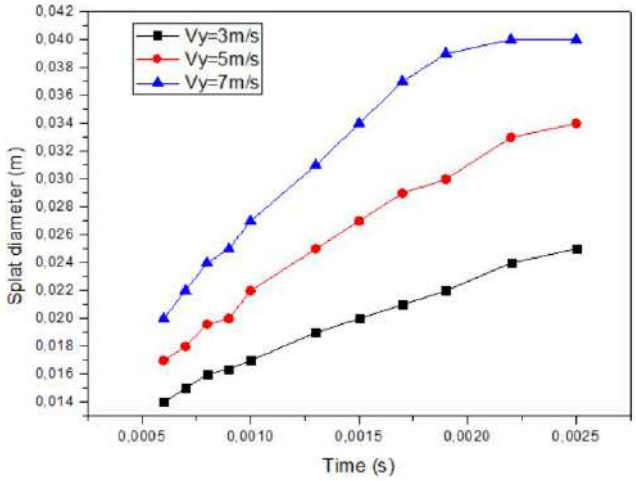


Figure 3. 14 Comparison of splat diameter during simultaneous impact of droplets at different impact velocities

Following that, we investigate the evolution of spreading velocity as a function of radial position with varying the initial velocities, as it is depicted in Figure 3.15.

The spreading velocity exhibits a consistent increase with respect to radial position until it reaches a specific threshold. Then a reduction in the velocity is observed, corresponding to droplet stabilization and the initiation of solidification at the splat bottom.

Negative velocity values near the droplet center at 3 m/s indicates that the kinetic energy of the fluid is converted into a reversed flow. At low impact velocity, the droplet has less kinetic energy, so surface tension becomes dominant, pulling the liquid back toward the center of the droplet.

Furthermore, a higher impact velocity clearly promotes an increase in spreading velocity along the radial direction. As the kinetic energy dissipates, the spreading velocity decreases. The rate of decline is slower when Vy= 7m/s, due to the higher momentum from the impact.

Figure 3.16 shows the variation in pressure with the radial position for different impact velocities over time. The pressure variation is similar to that seen in the successive droplet impact. The impact pressure is strongly influenced by the initial droplet velocity, with lower velocities resulting in reduced peak pressure levels at the first moment of imact (t=0.7ms). Subsequently, the pressure drops precipitously as a function of radial distance in every case. As the droplet spreads radially, the inertial energy is redistributed over an expanding contact area, thereby inducing a temporal decay in pressure. As inertial effects weaken, capillary

forces associated with surface tension become dominant and drive partial retraction of the lamella. This capillary-driven recoil produceses tensile stresses within the droplet, which are presented as negative pressure values.

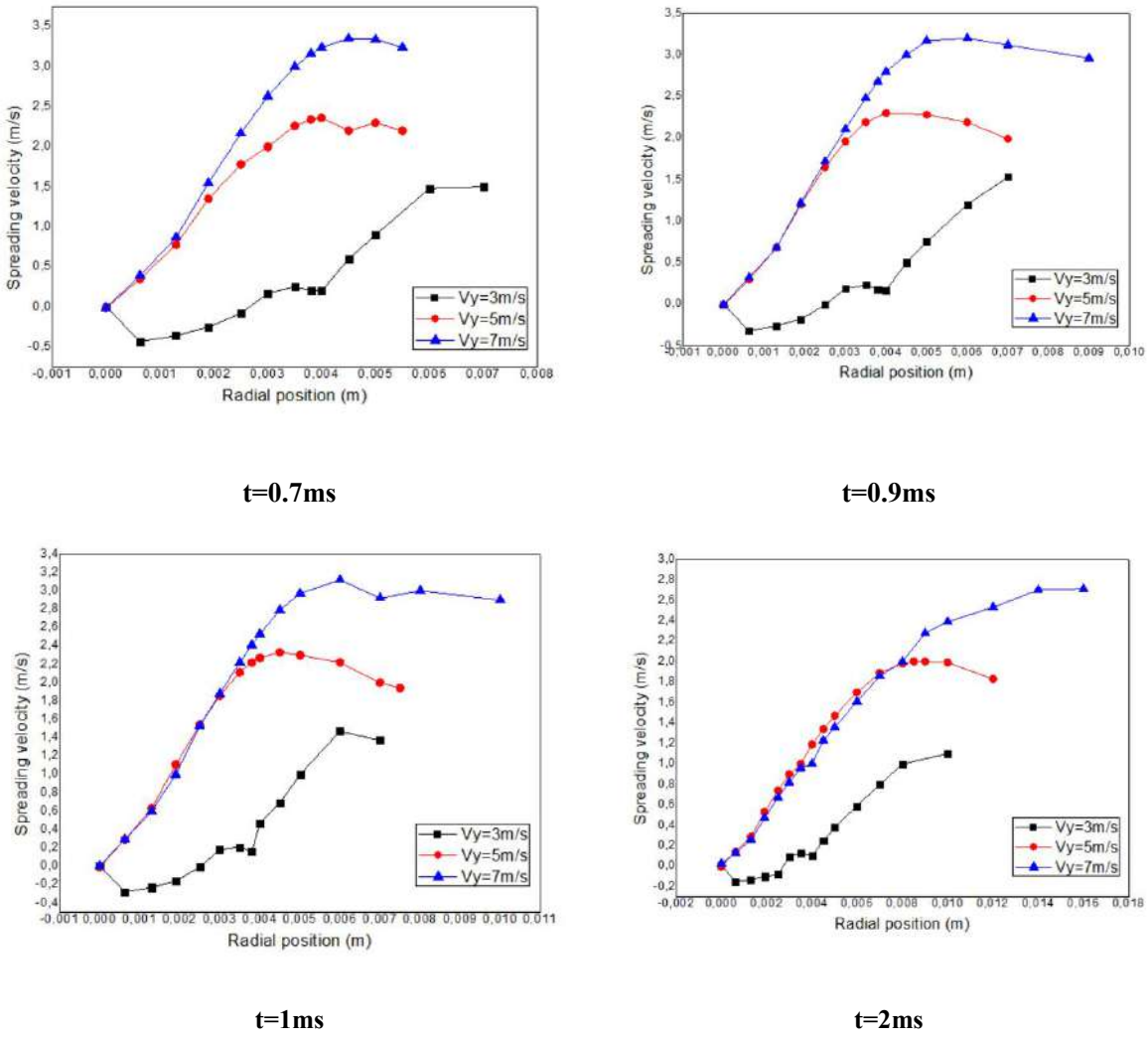
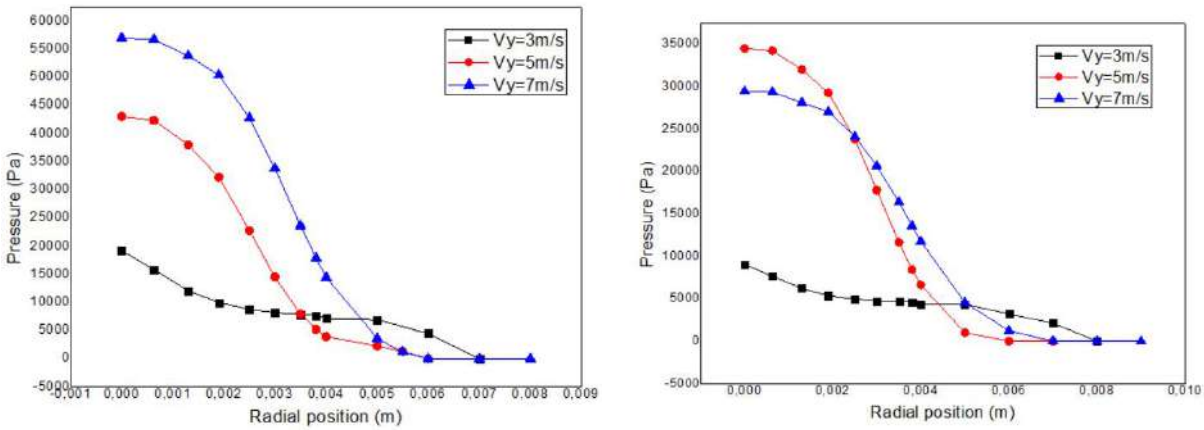
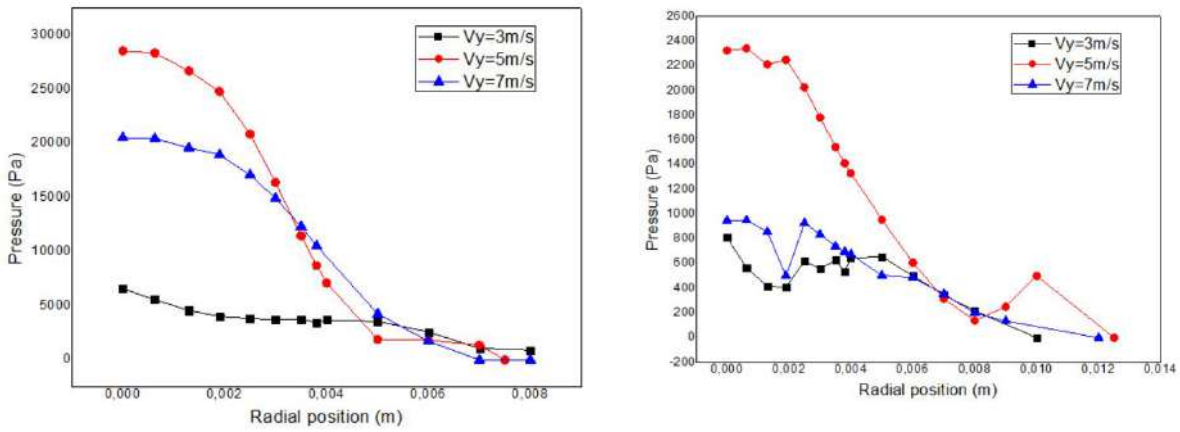


Figure 3. 15 The evolution of spreading velocity with the radial position for different impact velocities



t=0.7ms t=0.9ms



t=1ms t=2ms

Figure 3. 16 The evolution of pressure with the radial position for different impact velocities

The temperature distribution of simultaneous droplets impacting a substrate with different velocities and for different time intervals is illustrated in Figure 3.17. The interaction of the droplets results in a central uprising sheet that increases with velocity. Subsequently, simultaneous impact of droplets creates overlapping heat zones, as it observed at the center where the droplets coalesce. As time progress, the heat transfer to the substrate creates a radial temperature gradient. The contact areas cool more rapidly than the droplet's center, resulting in solidification occurring first at the bottom of the lamella.

In addition, lower velocities produce thicker sheets, thereby preserving thermal energy for a longer time. However, at elevated velocities (Vy ≥ 7), the central sheet may break up into smaller fragments (splashes) as a consequence of Rayleigh-Plateau instability [69]. The rapid cooling of the uprising sheet (early solidification) has the potential to influence the quality of the deposited layer, which is detrimental to coating uniformity.

In this context, it can be posited that increasing the impact velocity during simultaneous impacts may not always be beneficial comparable to those observed in sequential impacts. At higher velocities, this collision between the droplet is more violent, where the fluids push against each other, creating a high-pressure zone between them. This reduces the droplets spreading efficiently and causes the vertical jet, wasting energy that would otherwise be used for surface coverage. Additionally, in simultaneous impacts, the high velocity collision (high Weber number) of two expanding lamellae often leads to splashing at the contact line, where

the liquid breaks into tiny drops that fly off the surface, resulting in a loss of mass and poor deposition quality.

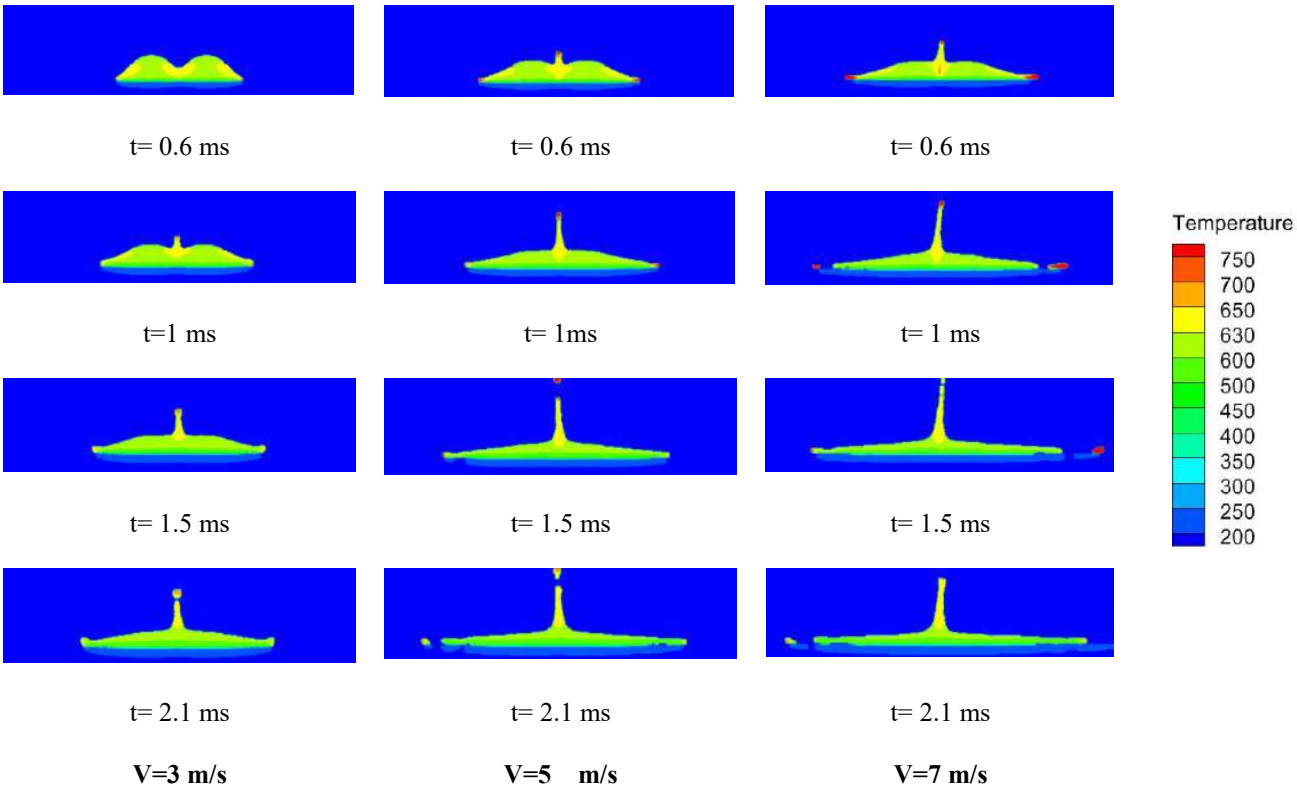


Figure 3. 17 The temporal variation of temperature distribution corresponding to various impact velocities

3.2.3. The effect of solid core within the droplet in successive impacts

In the preceding section, the impact and deposition of completely molten droplets during thermal spray process have been studied. However, real applications often involve the impingement of semi-molten droplets. Therefore, this section focuses on investigating semi-molten droplets and their effect on the resulting coating.

The droplets include a solid core surrounded by the molten material; thus, the spreading and solidification dynamics are predicted to be different compared to the fully molten droplet. In these simulations, the solid core of the particle is considered a highly viscous liquid [73]. Partially molten aluminum droplets with a diameter of 3.92 mm and a solid core of different percentages (25 %, 50% and 75 %) are modelled to impact a solid substrate with velocity of 3 m/s. The temperature of the solid core is set at 200°C in all cases.

To begin, the final splat diameter is measured at each time step for all the cases (0%, 25%, 50%, and 75%) and presented in Figure 3.18. It is evident from the results that the evolution

of the splat diameter shows almost similar trends for all cases, except for the case of the molten droplet (0% of solid core); it exhibits a larger final splat diameter. Therefore, it can be said that the spreading rate is reduced in the presence of a solid core within the droplet, where the unmolten metal prevents further spreading. Furthermore, the fully molten droplet exhibits a lower viscosity [68], hence, the spreading is more pronounced.

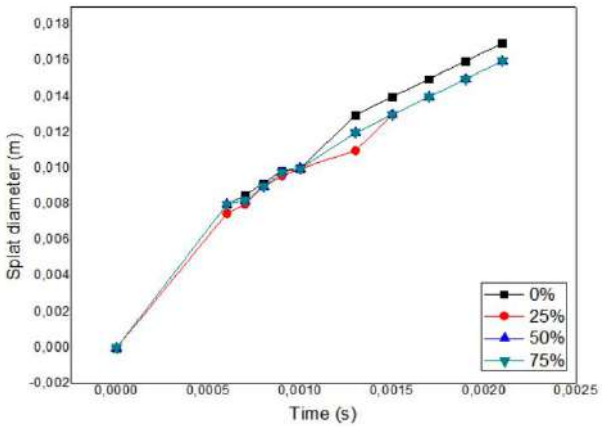


Figure 3. 18 Comparison of splat diameter during the successive impact of droplets for four different solid core percentages

The temperature distribution of the droplets during 2.1ms is presented in Figure 3.19. Regarding the morphological evolution of the droplets, we can observe that for all cases, the spreading efficiency decreases as the solid core percentage increases. However, the 25% solid core droplet shows the most significant lateral spreading. Since a larger volume is a liquid (it has lower viscosity), the impact's kinetic energy has spread the droplet into a wide, thin splat by 2.1 ms. The solid core of the second droplet largely retains its shape during spreading, forming a bump in the lamella´s final shape [73]. In addition, the final splat of the case of 75% is thicker compared to the 25% case, due to large internal solid mass that acts as a structural anchor. Therefore, it can be concluded that the existence of solid core within the droplet results in the undesirable shape of the final coating.

For the thermal distribution, the results indicate that at 1ms, the second droplet is entirely in contact with the first, and the molten layers of both droplets have merged and begin to flow and spread together. The molten layer of the subsequent droplet permitted an increase in the temperature of the first droplet solid core, resulting in its melting. Additionally, the liquid shell begins to cool rapidly upon contact with the substrate, indicating the onset of solidification at the splat bottom, and the hottest regions are pushed to the outer edges (periphery) during spreading.

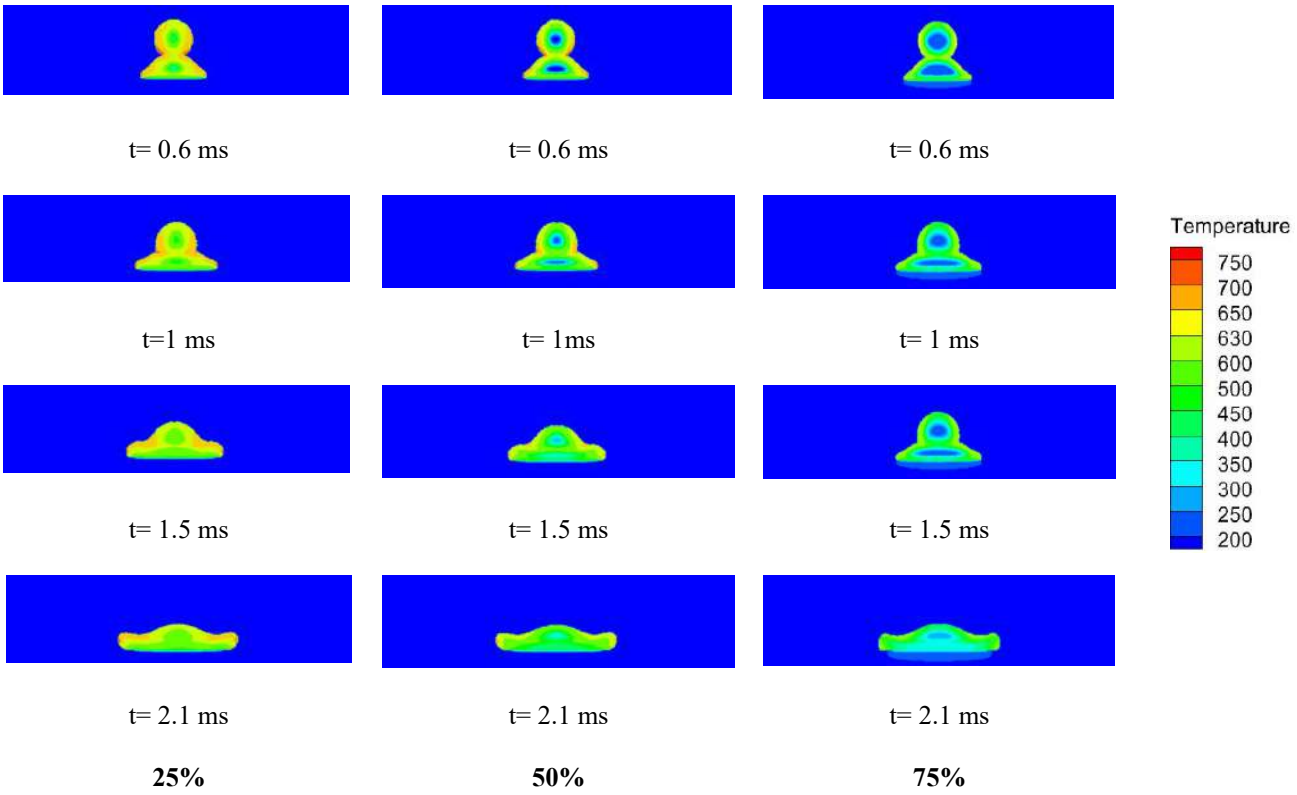
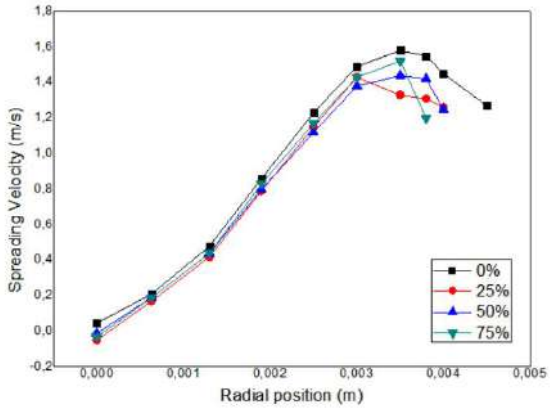


Figure 3. 19 The temporal variation of the temperature distribution for four different solid core percentages

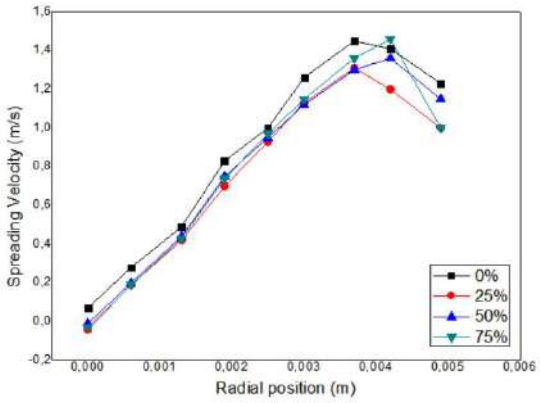
The results in Figure 3. 20 show that the spreading velocity of the completly molten droplet is the highest among all the cases, there is no internal structural resistance. The vertical velocity is converted into radial velocity. During the early stage of spreading, the fluid is driven outward at high velocity, which gradually decreases over time due to the solidification of the bottom splat. This solidified layer anchors the lamella to the substrate. In the case of molten droplet, solidification at the bottom takes longer to halt the momentum because the liquid volume is large.

However, it is evident that the 25% solid core shows a noticeable decrease in velocity compared to the 50 and 75 % cases. This could be explained by the larger solid core in these two cases, which may push the molten liquid layer faster. Thus, the 50% and 75% droplets are behaving like solid projectiles that are squeezing the liquid outward.

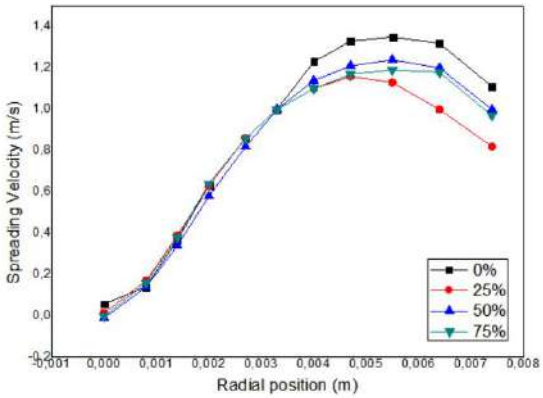
The pressure variation with the radial position is also investigated. As seen from Figure 3.21, the maximum pressure occurs at the center of the impact zone (r=0) in all cases. As the spreading progresses, the pressure drops significantly, where the kinetic energy is dissipated through friction and solidification. The high pressure at the impact improves the droplet/substrate mechanical interlocking, providing a strong adhesion of the coating [68].



t=0.7ms

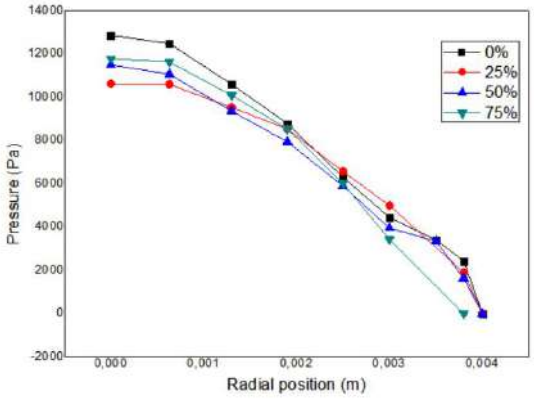


t=1ms

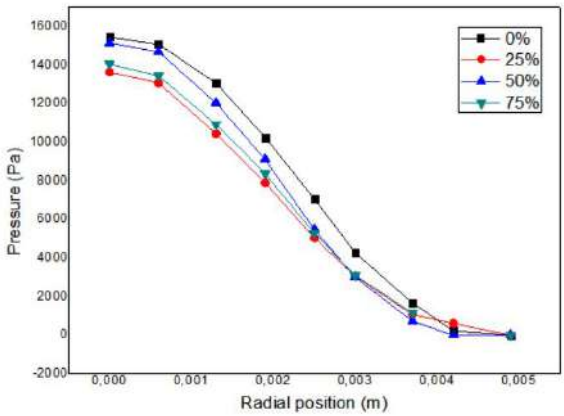


t=2ms

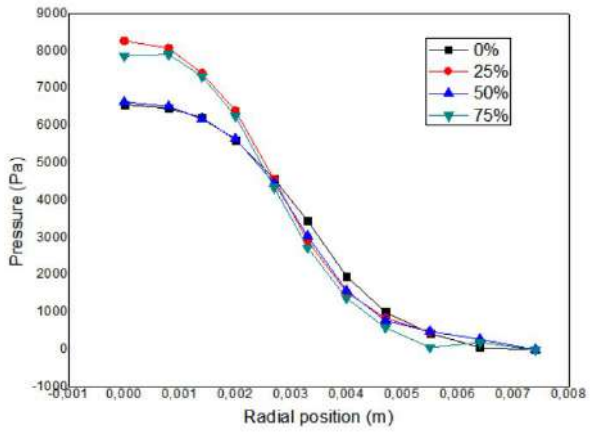
Figure 3. 20 The evolution of spreading velocity with the radial position for four different solid core percentages



t=0.7ms



t=1ms



t=2ms

Figure 3. 21 The evolution of pressure with the radial position for four different solid core percentages

While numerous research in literature has been dedicated to understanding droplet dynamics like spreading, solidification, splashing and rebound. However, there has been less attention concerning the mechanical response of the substrate during droplets impingement process.

This part focuses on the substrate surface behavior during the impact and spreading of droplets with different solid core percentages. The evolution of XY shear stress in the substrate during successive impact of Al droplets with 0%, 25%, 50% and 75 % of solid core is presented in Figure 3.22. Stress concentration occurs when the droplet/substrate contact area is subjected to greater stress than the average stress, resulting in substrate deformation [68].

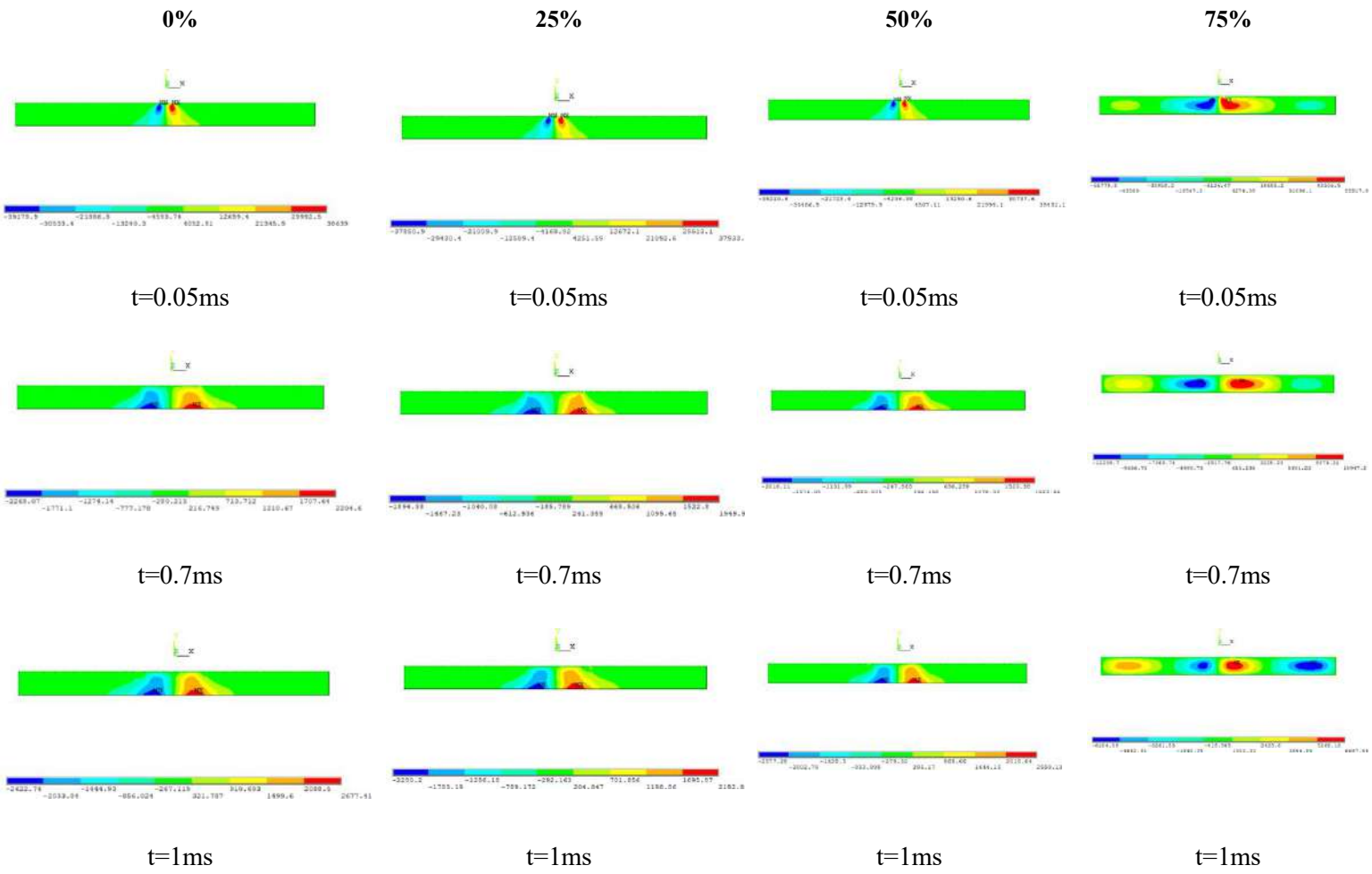
Initially, a Hertzian-type elastic contact field develops during the compressible impact phase, manifested by a concentrated subsurface shear stress maximum. With the onset of spreading, this stress distribution undergoes a significant evolution, extending radially in synchrony with the outward growth of the liquid lamella.

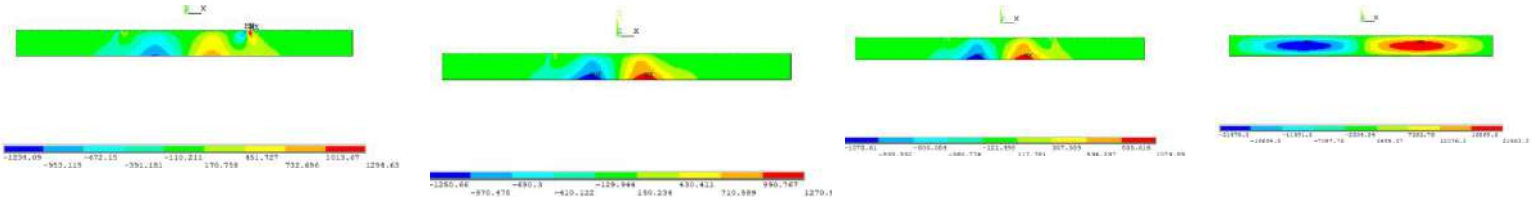
For the case of 0 %, the shear stress is concentrated at the surface of the substrate. Since the droplet is fully molten, it flows easily upon impact, dissipating energy through spreading rather than deep mechanical penetration. As the solid core size increases, the stress concentration becomes more localized. The shear stress magnitudes are significantly higher in the case of 75%, indicating a high-velocity elastic-plastic deformation where the solid mass dictates the substrate's response. +The stress begins to dissipate and relax over time.

Furthermore, in the case of the droplet containing 75% solid core, the substrate exhibits more pronounced and asymmetric XY shear stress distributions compared to the other cases. This

behavior can be attributed to the stronger mechanical interaction at impact due to the higher rigidity of the droplet core, which transmits a more intense impulse to the substrate. The higher solid fraction reduces the droplet's ability to dissipate kinetic energy through deformation, thereby increasing the stress concentration at the droplet/substrate interface. Consequently, a significant portion of this energy propagates through the substrate in the form of elastic waves, leading to the formation of distinct symmetric or mirrored stress zones beneath the impact area.

In successive impacts, the second droplet impacts a substrate that is still stressed and thermally softened by the first impact. The combined effects of stress-wave interference and thermal softening increase plastic deformation and residual stress. While this enhances adhesion through improved mechanical interlocking, it also raises the risk of fatigue damage and interfacial delamination.





t=2.1ms t=2.1ms t=2.1ms t=2.1ms

Figure 3. 22 XY shear stress distribution over time in successive impact for four different solid core percentages

3.2.4. The effect of the substrate oxidation

The surface oxide layer is a key factor governing the splat morphology and overall coating efficiency. This study examines how oxidation influences the behavior of aluminum droplet by considering different oxide layer thicknesses. Oxidation can easily form on the surface of steel substrate, which increases the contact resistance. The properties of the oxide layer (Fe_2O_3) are listed in Table 3.3.

Table 3.3 Properties Fe_2O_3 oxide layer [33]

Density (Kg/m³)	**Thermal conductivity** (W/m K)	**Specific heat** (J/Kg K)
5240	2.9	670

The effect of oxide layers with thicknesses of 0.1, 0.3, and 0.5 mm on the spreading behavior over a steel substrate is evaluated using the temporal evolution of the spreading factor (Figure 3.23). The behavior observed during the deposition on oxidized substrate is similar to that of the non-oxidized substrate [68]. In the early stages of impact, there is a sharp increase in the spread factor, than it begins to decelerate as kinetic energy is converted into surface energy and dissipated through viscous friction. Oxide layers typically act as thermal barriers. In molten metal impacts, a thicker oxide layer usually reduces the cooling rate, which allows for more spreading. However, the results show that the differences between thicknesses are relatively small. This is attributed to the relatively small oxide-layer thicknesses considered in this study, which do not significantly alter the droplet behavior.

The splat morphology and the temperature distribution are shown in Figure 3.24. Splashed splats were obtained in the presence of substrate oxidation. During spreading, the aluminum

lamella becomes thinner and develops a pronounced peripheral edge. This is because the surface energy drags the edges of the splat backward, resulting in boundary formation around the lamella [74]. The presence of an oxide layer causes the splat edges to break off and produce splashes, and as the oxide thickness increases, it further hinders smooth spreading of the droplet, thereby intensifying the splashing behavior.

In addition, the presence of the oxide layer on the surface may serve as a thermal barrier, reducing droplet/substrate heat exchange [75]. Therefore, the Al droplet retains higher temperatures for long duration, due to the cooling delay [68].

The evolution of pressure at the point of impact over time is illustrated in Figure 3.25. High pressure is produced at the first impact with the substrate, reaching approximately 245 kPa at roughly 0.1 ms. This represents the Water Hammer peak. This pressure only lasts for the brief moment before the droplet begins to spread over the substrate. Such pressure levels are sufficient to achieve effective adhesion between the droplets to the substrate, enhancing the mechanical interlocking. The thickness of the oxide layer has no effect on the pressure the droplet exerts on the surface. Therefore, The impact is dominated by the fluid's velocity and density, not the substrate's coating properties.

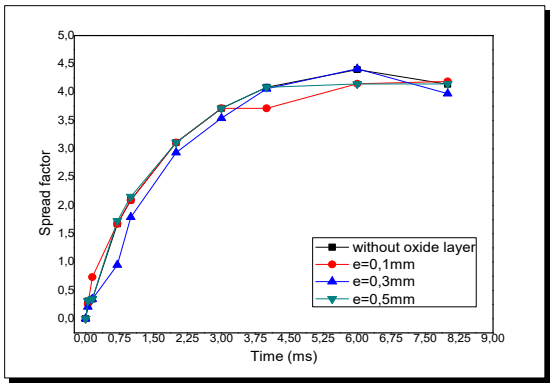


Figure 3. 23 The evolution of spreading factor over time for all the cases

Sans couche d'oxyde	0.1 mm	0.3 mm	0.5 mm

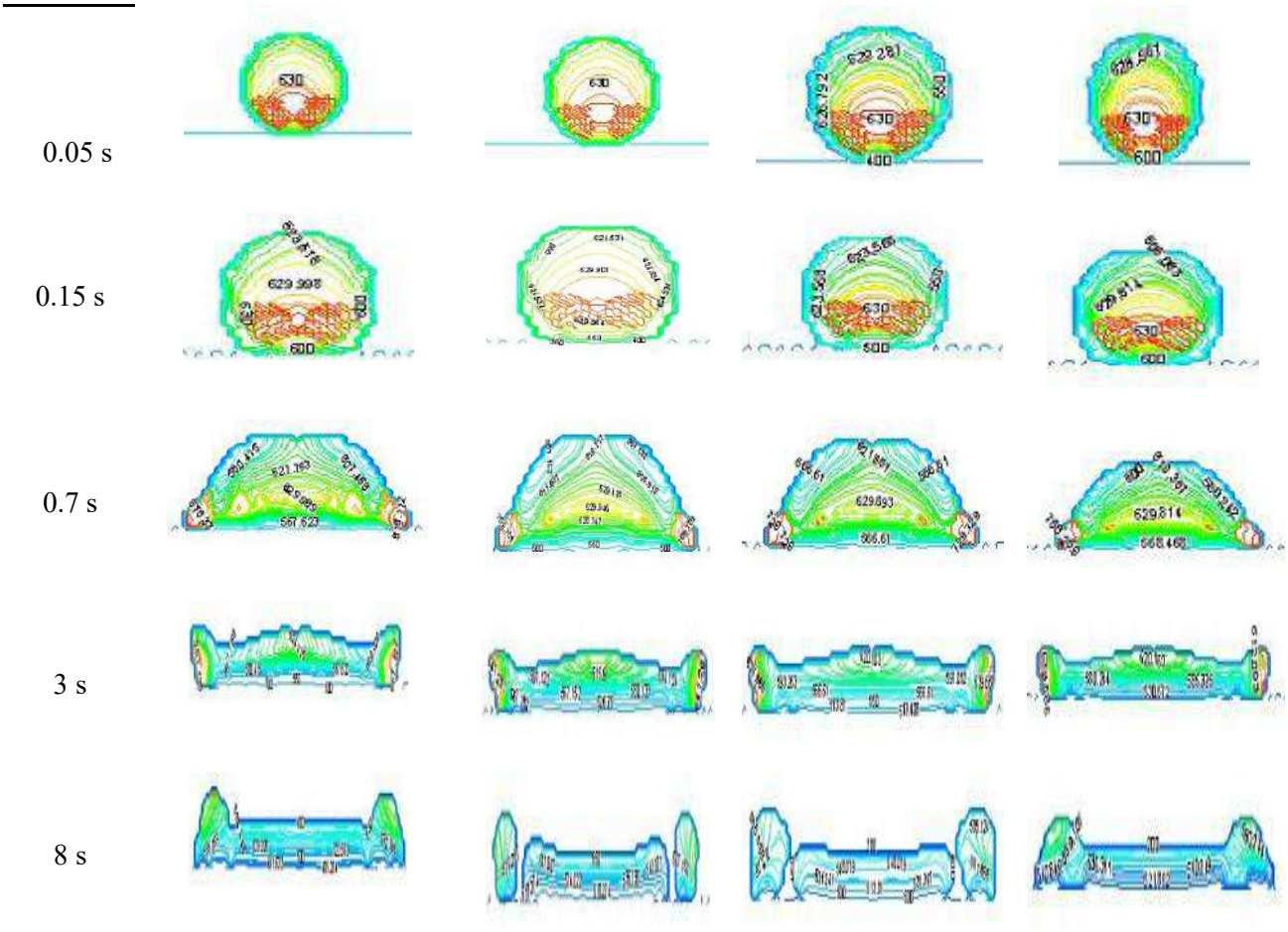


Figure 3. 24 The temperature distribution within the droplet during its deposition on oxidized substrate

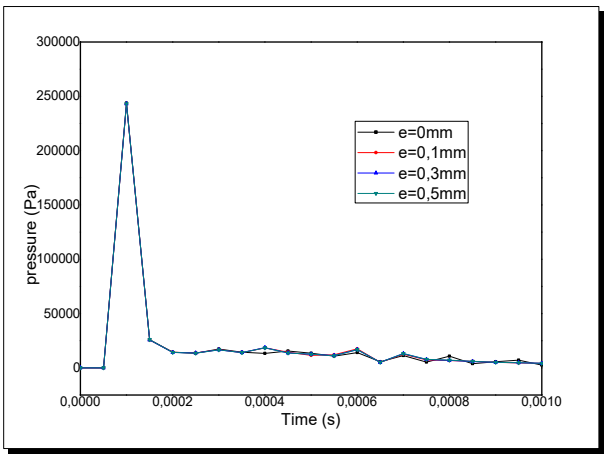


Figure 3. 25 The evolution of pressure at the point of impact for all the cases

In order to assess the influence of the oxide layer on droplet/substrate interaction, shear stress distribution within the substrate is analysed in Figure 3.26. The spatial presentation of the stresses developed in the substrate shows a symmetry of intensity and traveling with the edges of the particle. Also, the shear stress is highly concentrated directly beneath the impact region due to the high-pressure shock upon the impact. As the droplet spreads, the stress concentration moves outward from the center of impact. By t=8ms, the droplet reaches its maximum spread and loses its kinetic energy, thus, the dynamic stresses dissipate, leaving a residual stress field dominated by thermal mismatch and solidification. As the oxide thickness increases from 0.1mm to 0.5mm, a significant increase in the magnitude of XY shear stress is observed within the oxide layer. These elevated shear magnitudes in the 0.5mm case suggest a higher risk of interfacial delamination and residual tensile stress compared to thinner oxidation states. Furthermore, the temporal analysis shows that these stresses peak at approximately 3 ms, coinciding with the maximum radial velocity of the droplet.

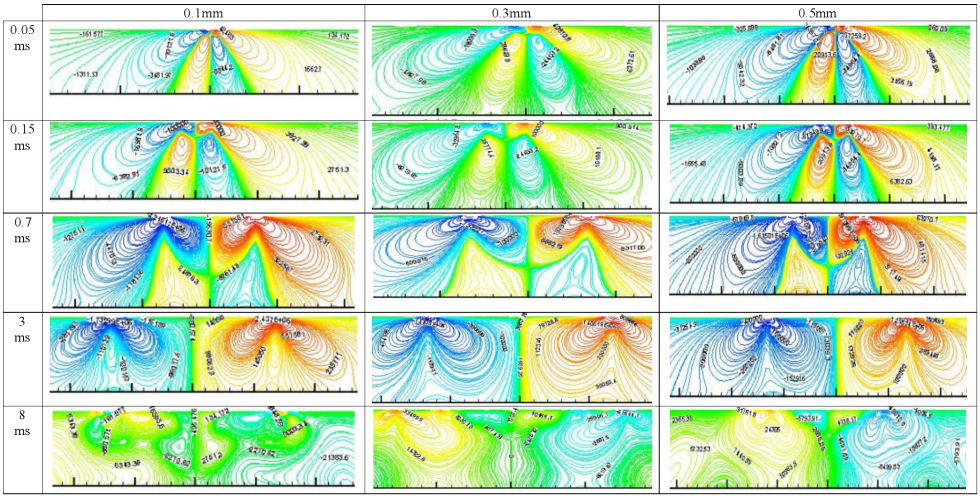


Figure 3. 26 XY shear stress distribution over time

Conclusion

To conclude, the main findings of this chapter are summarized as follows:

- ✧ The simulation results obtained by numerical model developed in the current study agree well with the reference experiment.
- ✧ The vertical and horizontal spacing between the droplets affects the morphology of the lamella. During simultaneous impact, the droplets generate a material jet at the meeting region. In addition, the spreading rate increases with the droplet spacing.

- A high impact velocity leads to a greater spreading rate because the droplet's kinetic energy exceeds the resisting surface tension and viscous forces.
- The spreading of a completely molten droplet is more extensive than that of a droplet containing a solid core. Furthermore, the droplet with 75% of solid core produces a high shear stress at the point of impact.
- The oxide layer increases the contact resistance at the interface, and it can act as thermal barrier.

This chapter focused on the impact, spreading, and solidification of molten and semi-molten droplets in thermal spray processes, where deposition is governed primarily by thermal effects. Alternatively, coatings can be realized through a solid-state process, where bonding is driven by high-velocity impact and severe plastic deformation. This alternative regime is exemplified by the cold spray process. The next chapter extends the analysis from molten droplet deposition to solid particle impact in cold spray.

Chapter 4

Numerical simulation of high-velocity solid particle impact

This chapter focuses on the Cold Spray (CS) process, in which solid particles are deposited onto a substrate at relatively low temperatures (less than the melting temperature of the material) and high velocities (higher than the critical velocity of the material). The process is examined through numerical simulations carried out using the ABAQUS software, using both LAGRANGE and CEL methods. These approaches are described in detail and validated with previous research. The main factors influencing particle/substrate interaction and bonding, such as particle velocity, preheating effect, and material properties, are also discussed.

Introduction

Cold spray has been presented in the literature by different names such as “solid-state deposition”, "kinetic energy metallization”, “kinetic spraying”, or “high-velocity powder deposition”, and others [76]. It was developed in the mid-1980s, by Soviet scientist Anatolii Popyrin, at the Institute of Theoretical and Applied Mechanics of the Siberian Division of the Russian Academy of Science.

Cold Spray is a process of depositing solid particles at temperatures below their melting point on a prepared substrate. These particles (typically ranging from 5 to 100 μm) are accelerated by a supersonic jet of high-pressure gases (such as N2, He, and air). The pressurized gas expands to supersonic velocity, resulting in decreased pressure and temperature [77]. Unlike conventional thermal spraying, the deposition technique focuses mainly on particle kinetic energy instead of thermal energy and kinetic energy combination [78]. Hence, the detrimental impacts of high-temperature oxidation, melting, evaporation, crystallization, residual strains, gas release, and other prevalent issues associated with thermal spray techniques are minimized or eradicated [79].

The adhesion of particles in cold spray is posited to arise from considerable plastic deformation and the associated processes occurring at the interface; as solid particles collide with the substrate, they undergo substantial plastic deformation, achieving a strong bonding with the substrate, thus, resulting in dense and well-adhered coatings with very little porosity [80,81]. In addition, the adiabatic softening of the material at the contact interfacial with the high contact pressures facilitates the development of fitting contacting surfaces by the plastic deformation of these surfaces [77].

When the particle velocity surpasses the critical velocity (minimal velocity required for particle/substrate adhesion), the bonding happens. Nevertheless, increasing the velocity to a hypervelocity (also known as erosion velocity), causes significant erosion in the substrate or the formed coatings, leading to poor coating performance. Since the sprayed material remains in the solid state throughout the process without undergoing melting, the thermal effects on the final coating and the substrate are minimized, preserving their mechanical properties.

Generally, materials of the coating and the substrate can be classified based on their hardness as: hard/hard, soft/soft, hard/soft, and soft/hard, as schematized in Figure 4.1

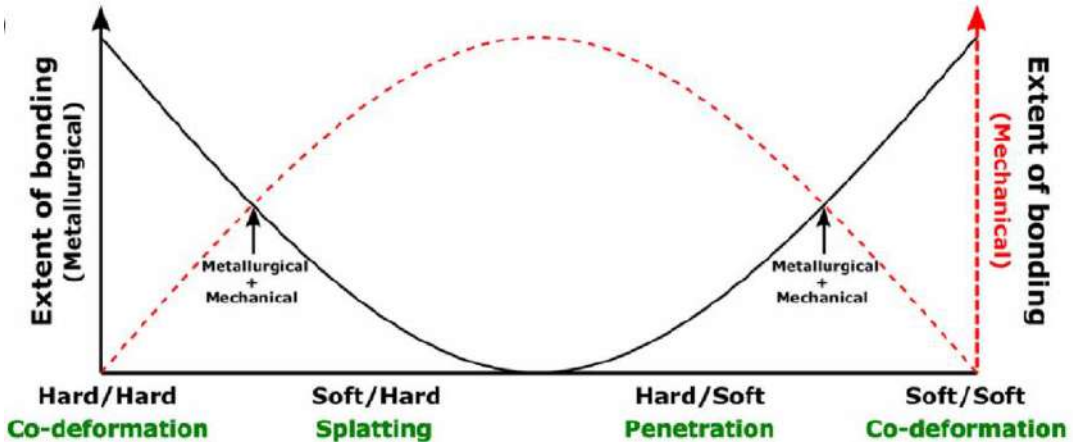


Figure 4. 1 Bonding mechanisms based on material combinations [76]

In CS process, the working gas is previously heated in a chamber, reaching high pressure, passing through specially designed convergent-divergent Laval nozzles, accelerating it to supersonic velocities, and dragging the feedstock powders to impact onto the substrate after exiting the nozzle [81,76], as presented schematically in Figure 4.2. Higher powder feed rates result in reduced particle velocity due to severe gas-particle interaction [82].

Like other material processing technologies, the CS has its own advantages. Since it is a solid-state process (no melting occurs in the material), the particles do not experience extreme temperatures, reducing oxidation, preventing phase change, and minimizing heat transfer to the substrate [77,83]. Very high deposition efficiency (95%) has been achieved with the CS due to the very high velocity put on the particles, approaching supersonic velocity values especially for ductile materials (like aluminum, copper, and titanium), alloys, and composites. Optimizing spray parameters, such as minimizing oxygen content, selecting appropriate particle size, and stress-relieving the powder can significantly enhance deposition efficiency for most materials including refractory metals [83]. Cold spray can also achieve high deposition rate; it can produce 10 mm wide spray beams with sharp edges. This results in fast coating, allowing for the formation of a thick layer (1–2 mm) within minutes.

Cold spray is recognized for its high-density coatings, wherein particles undergo plastic deformation without melting, hence reducing voids. Furthermore, the particles flow and fill the gaps owing to the localized softening.

In conventional thermal spray processes, the substrate is heated by the flame, which can be a problem for materials that are sensitive to high temperatures, and also causes the substrate to

warp, especially if it's thin. While in CS, there is no high-temperature jet; the substrate is not directly heated. It only receives a little amount of heat as a result of high plastic deformation from the particles that impact it. Therefore, CS is appropriate for coatings or repairing parts made from temperature-sensitive materials. CS inhibits materials oxidizing during the deposition due to the relatively low temperature that the material absorbs during the spraying process [84].

While cold spray offers distinct advantages, it also has notable limitations; for instance, pure ceramics and some alloys display inadequate deformation. Furthermore, CS coatings necessitate a ductile substrate to promote plastic deformation and guarantee good adherence. Consequently, when applied to hard or brittle substrates such as ceramics, the bonding strength tends to be weak [77].

A high rate of processing gas consumption is required—helium is often preferred for high-quality coatings despite its high cost [85]; extended spraying procedures may lead to nozzle clogging, resulting in inconsistent deposition rates and diminished coating quality [86]. Additionally, CS is not ideal for very complex shapes or deep internal surfaces.

There are many applications for CS coating, some of them are given below.

- Corrosion and erosion protection (aluminum and titanium coatings for corrosion/erosion resistance);
- Repair and restoration;
- Wear resistant coatings;
- Biomedical: prostheses with improved wear resistance, porous Ti coatings for bone in growth;
- Aerospace and defense;
- Oil and gas (energy): improved corrosion resistance;
- Additive manufacturing (3D printing): rapid prototyping of Al-Ti components;
- Electronics and semiconductors.

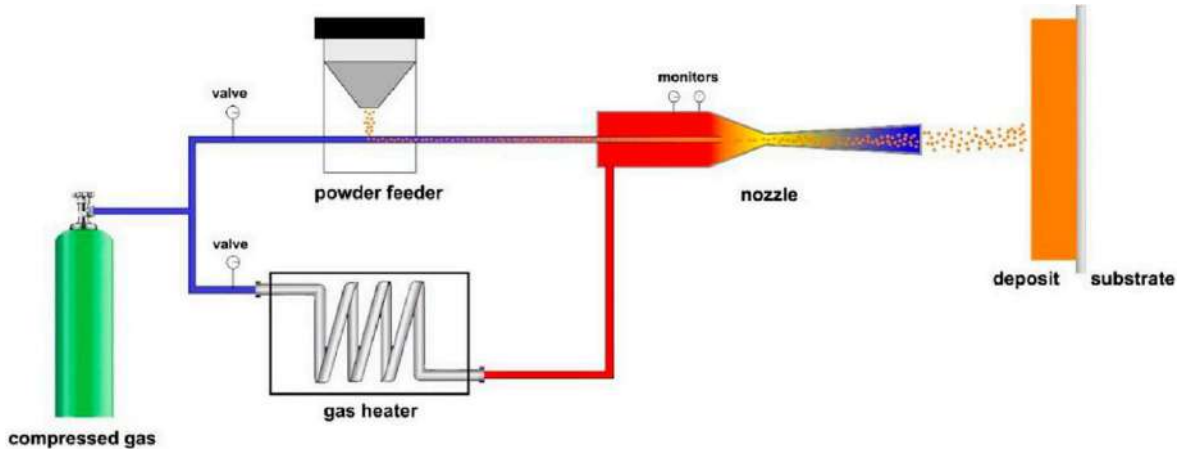


Figure 4. 2 The schematic diagram of the cold spray system [80]

4.1. Previous studies: experimental results

Cold spray technology has gained interest in a variety of industries for its ability to produce high-quality coatings without melting the material. This section summarizes the experimental results of the cold spray process from various scientific studies, highlighting the fundamental mechanisms governing particle/substrate interaction, bonding formation, and coating quality.

Xiawei Yang et al [87] conducted an experimental of single 47.8 μm Al particle deposition on Cu substrate. The parameters used in the experiment are gas pressure of 3.4 MPa with preheating of 300°C, powder feeding rate of 0.6 rpm and spraying distance of 30 mm. The impact velocity of the powders was 620 m/s. As it shown in Figure 4.3, the jet phenomena occur at the particle/substrate interface (the white arrow). This is caused by significant plastic deformation at the interface.

Jiashuo Qi et al [88] investigated the microstructure of the Al 1050, AlSi10Mg, and Scalmalloy coatings, starting from the feedstock powders injection to final coating deposition, to examine the bonding mechanism in CS. They used an Al 7075 T6 plate as a substrate. The impacting solid powders are with a size of about 15~45 μm. As a result, a coating with a thickness of 2 mm is achieved after multiple passes of deposition for each powder. Figure 4.4 shows the top surface shape of three Al materials after the deposit procedure, indicating the typical surface microstructure of atomized powders. Following the impact, all three splats are severely deformed, and the contrast inside the aluminum splats is relatively homogeneous.

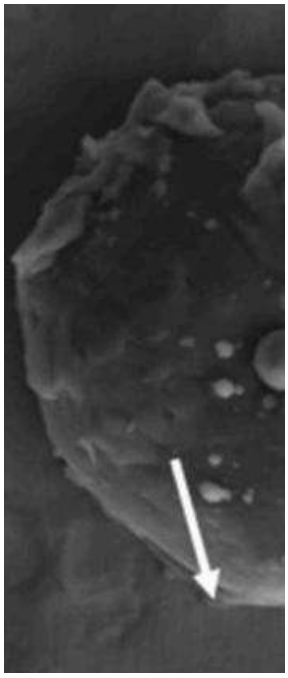
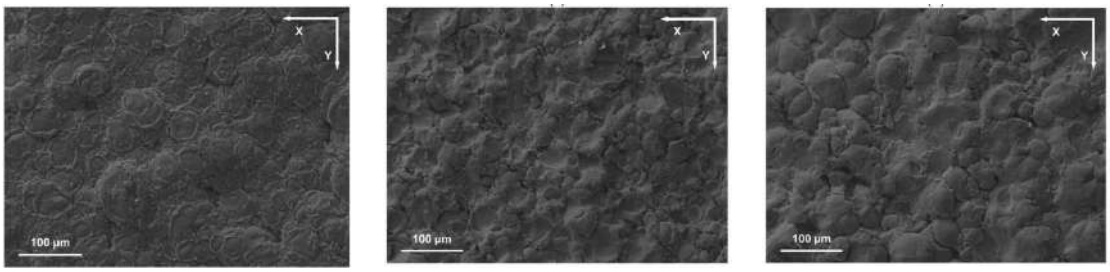


Figure 4. 3 Surface morphology of coating deposition from experiment of reference [87]



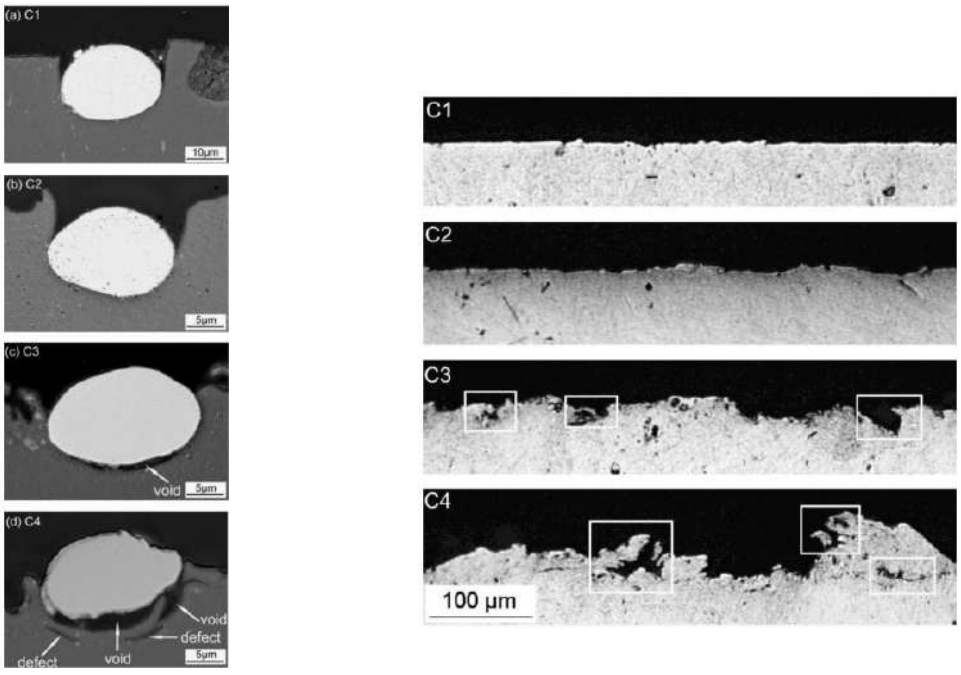
a **b** **c**

Figure 4. 4 SEM micrograph of the top surfaces of (a) Al 1050 (b) AlSi10Mg, and (c) Scalmalloy powders generated by CS process from reference [88]

The influence of the substrate surface pretreatment on the Ni/Al interfacial bonding mechanism during cold spray was investigated by Shuo Yin et al [89]. Single Ni particles impact different Al substrates (polished substrate, ground substrate, grit-blasted substrate by small size Al_2O_3 sand, and grit-blasted substrate by large size Al_2O_3 sand). The pure Ni powder has a spherical morphology and a size range of 10 to 45 μm, and it was deposited at a velocity of 500 m/s, and working temperature of 600°K. Figure 4.5 illustrated cross-sectional SEM image of Ni deposition on different Al substrates. As can be observed, unlike the polished and ground substrates, voids are formed at the particle/substrate interface in the case of the grit-blasted.

Shuo Yin et al [90] studied solid-state cold spraying for the first time to produce FeCoNiCrMn HEA coating. The spherical FeCoNiCrMn HEA powder with a size of 15 to

53um was deposited on a flat 6082Al alloy substrate at working temperature of 300K. The experimental results show that FeCoNiCrMn particle was entirely trapped by the extremely deformed substrate material (Figure 4.6), resulting in the formation of mechanical interlocking between the coating and the substrate, improving their adhesion strength.



a **b**

Figure 4. 5 (a) Cross-sectional SEM image of a single Ni particle deposition on different Al substrates adabted from experiment of reference [89]. (b) Substrate surface region after different surface pretreatments (C1: polished substrate, C2: ground substrate, C3: grit-blasted substrate by small size Al2O3 sand and C4: grit-blasted substrate by large size Al2O3 sand)

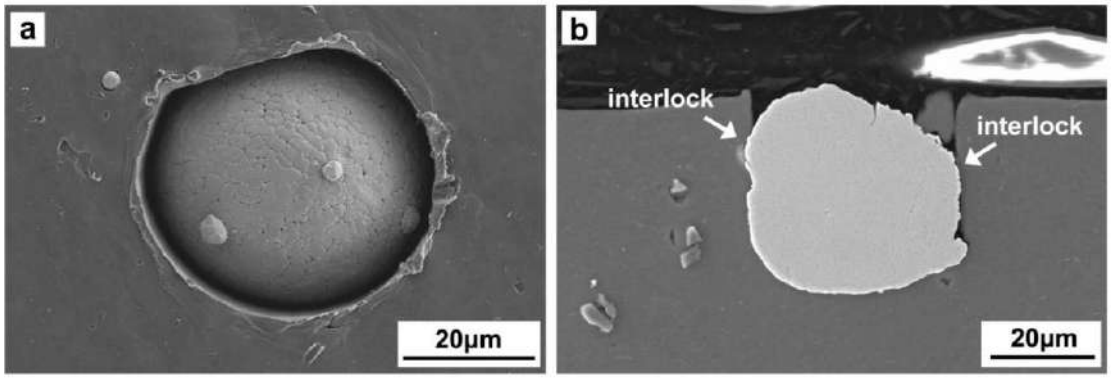


Figure 4. 6 Single HEA particle depositing onto a 6082 Al alloy substrate from experiment of reference [90]. (a) Surface morphology. (b) cross-sectional view

Another study of the substrate effect during the cold spray process was conducted by Alessia Bruera et al [91] in order to examine the substrate hardness and roughness. The focus of their study is the deposition of Cu particles on AISI 304 steel substrates with varying roughness

levels and hardness. The AISI 304 surface was either polished or grit-blasted to different roughness. The results are depicted in Figure 4.7. It was found that the adhesion of the Cu particles with hardened and roughened surfaces is more than on polished surfaces. The bonding increases during the deposition of sprayed Cu particles on roughened and annealed (softened) substrates. The influence of particle velocity on silver coatings was examined by Chavan et al [92], Figure 4.8 depicts cross section micrographs of the coatings obtained at different impact speeds (363 m/s, 403 m/s and 469 m/s). Based on the experiment findings, particle deformation during CS rises as particle velocity increases, as demonstrated by an increase in the aspect ratio of the splats. Figure 4.9 shows photographs of brittle coating on iron cracked by the impact of single particle with 100m/s, at angles of 30◦ and 90◦. Considering the damage behavior induced by the particle impact, Yoshinori Isomoto Oka et al [93] believe that the particle might remove substantial material with a smaller contact angle. Besides, cracks were generated in the outer region of the craters, and the coating films were peeled off just at the edge of the craters.

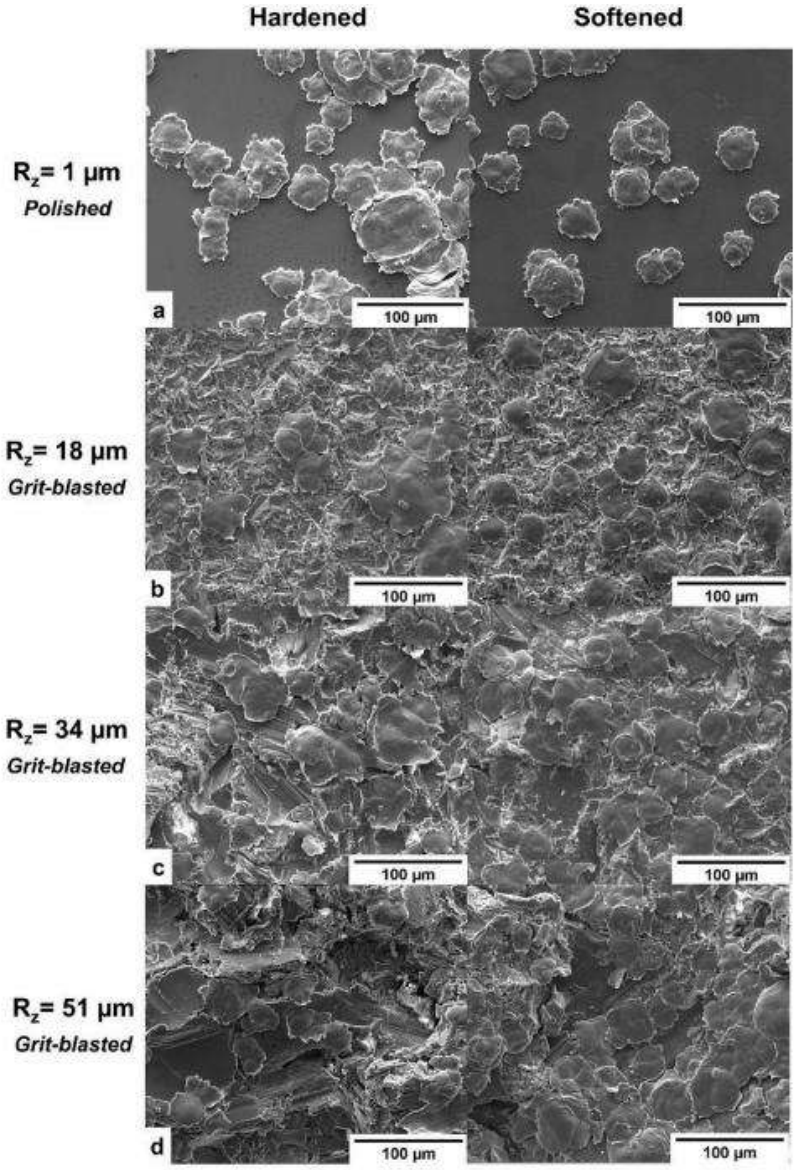


Figure 4. 7 Single Cu particle impact morphologies on both hardened and softened substrates with varying surface roughnesses from experiment of reference [91]

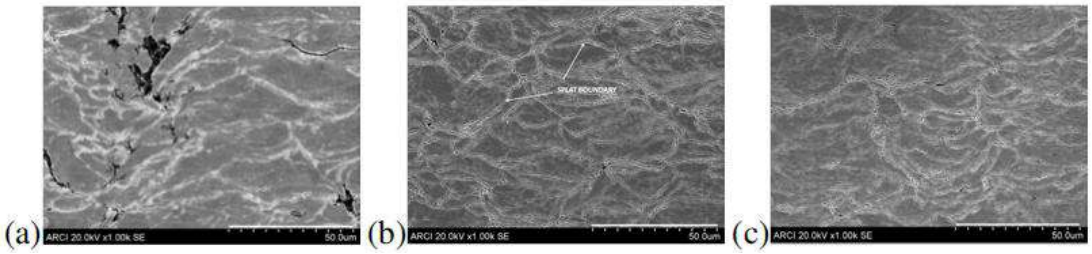


Figure 4. 8 Cross section micrographs of splats formed at different particle velocities (a) 363 m/s (b) 403 m/s and (c) 469 m/s, from reference [92]

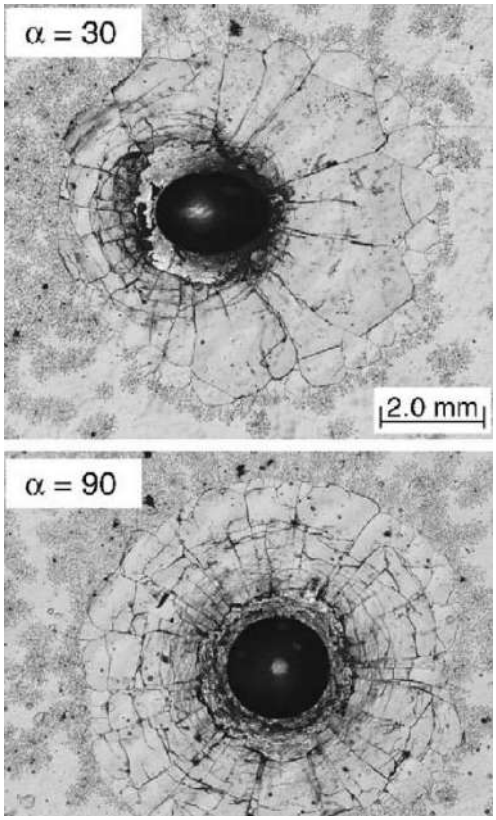


Figure 4. 9 Photographs of brittle coating on iron cracked obtained by single particle impact at angles of 30◦ and 90◦ and impact velocity of 100m/s from experiment of reference [93]

4.2. Numerical approaches

Due to the extremely short time scale of the impact during cold spray, it is highly challenging to observe the particle deformation process experimentally. Consequently, computational simulations of particle/substrate interaction have become a crucial method for clarifying the bonding mechanism involved in the CS process. This section presents a brief overview of the main numerical approaches used in CS simulations.

4.2.1. Lagrangian method

A major advantage of the Lagrangian model is reducing calculation time by assuming symmetrical impacts, allowing for axisymmetric (quarter) models [94]. The Lagrangian method tracks the material in a reference frame that moves along with the deforming material, i.e. the mesh moves with the material [77]. However, it is believed that there exist some limitations in the Lagrangian approach, the Lagrange grids distort excessively, resulting in an abnormal termination of the computation program when using fine mesh or simulating large deformation [95], this requires re-meshing or adaptive techniques. The Lagrange model is more suitable for representing solid-like structures. Its advantages are computation efficiency and capturing localized phenomena (like jetting and crater formation in the substrate).

4.2.2. Eulerian method

The Eulerian method involves two overlapping meshes: a fixed backdrop spatial mesh and material that flows through it [96]. This approach is effective for avoiding mesh distortion issues common in Lagrangian method, making it suitable for high-impact and severe deformation cases. However, due to the fine mesh, it takes long simulation run durations [97]. In addition, the contact properties such as the coefficient of friction cannot be modified in contrast to the Lagrangian method.

4.2.3. Arbitrary Lagrangian Eulerian method

The ALE combines the features of pure Lagrangian and Eulerian analysis to model the cold spray (CS) process more effectively. In the ALE the mesh can move independently of material flow; it allows adaptive rezoning to prevent excessive distortion. In addition, ALE enables continual grid redefinition in predefined and arbitrary ways during calculation, resulting in continuous rezoning facility [77]. It is useful for studying particle bonding, extreme deformation, and thermo-mechanical effects. Compared to the Lagrangian, an additional computing step of rezoning is used, which increases the calculation cost.

4.2.4. Coupled Eulerian Lagrangian method

The CEL approach combines the Lagrangian and Eulerian formulation; it addresses two major challenges faced by traditional simulation approaches: mesh distortion and unrealistic particle deformation in the Lagrangian method. Moreover, the approach facilitates the particle/substrate interface tracking in the Eulerian formulation through the computation of the Eulerian volume fraction at each element (Appendix C). For CEL, Eulerian mesh is created to contain the material of one part of the model, while the other part is modelled using a traditional Lagrangian mesh [77,83,98], where the mesh deforms with the material.

To simplify the Eulerian part of the model, the volume fraction method is used. If a material entirely occupies an element, its volume fraction is one; conversely, if no material exists within an element, its volume fraction is zero. The CEL method solves complex fluid-structure interaction problems including high strain rate deformation problem and allows multiple materials to interact in a shared domain, i.e. Eulerian elements may simultaneously contain more than one material. It was verified that the CEL model is more robust and accurate in higher deformation regimes compared with other numerical methods [77].

4.2.5. Smoothed Particle Hydrodynamics method

SPH method is a mesh-free Lagrangian technique that can handle extensive deformation problems such as the feedstock particles/substrate impact process in CS [99]. It predicts the patterns of droplet deformation in addition to the thermal distribution. The meshless nature of SPH helps to prevent mesh distortion throughout the simulation. In smoothed particle hydrodynamics, the domain is filled with particles, each representing a portion of the material. These particles are distinct from the powder particles utilized to produce the CS Coating.

The SPH approach demonstrated that feedstock particles did not rebound after impact, which may be beneficial for capturing dynamic features at the impact interface [100]. However, this method provides high computational effort and low computational accuracy. Furthermore, high time to obtain accurate results and it is computationally expensive for high-resolution simulations.

4.3. Numerical methodology

Cold spray simulations require accurately modeling the behavior of particles and substrates under high-velocity impact necessitates the use of multiple material models.

The governing equations for deformation of a continuous substance are given by the following equations [101]:

Conservation of mass:

$$\frac{d\rho}{dt} = -\rho \nabla . v = 0 \tag{4.1}$$

v: the velocity vector.

Conservation of momentum:

$$\frac{dv}{dt} = \frac{1}{\rho} \nabla . \sigma \tag{4.2}$$

σ : the internal stress

Conservation of energy:

$$\rho\, C_p \frac{dT}{dt} = \nabla.(k\nabla T) + \dot{q} \tag{4.3}$$

Where C_p is specific heat capacity, k is thermal conductivity, and $\dot{q}$ is internal heat generation rate due to plasticity.

A fraction β (Taylor–Quinney coefficient) of plastic work is converted into heat. Therefore, the rate of inelastic heat generated due to plastic work can be calculated from: $\dot{q} = \beta\ \sigma_e\ \mathrm{d}\varepsilon_{\mathrm{pl}}$

$\beta \approx 0.85 - 0.95$ for high strain-rate impacts, σ_e is the equivalent stress, $\mathrm{d}\varepsilon_{\mathrm{pl}}$ is the plastic strain rate, and $\dot{q}$ is the volumetric heat generation rate.

In this study, given the high-strain-rate nature of the impact in cold spray, the materials behavior was modeled using the Taylor-Quinney relation with a coefficient of β=0.9, meaning that 90% of the plastic work is converted into heat. The remaining 10% is typically stored within the material's microstructure as defects

It is worth mention that only the model's solid domains are covered here. The effects of the surrounding gas are neglected [102].

4.3.1. Johnson-Cook (JC) Plasticity Model

During the CS process, the solid micro particles impact onto the substrate at supersonic velocities, where both particles and substrates undergo sever plastic deformation. The plastic deformation of materials was described by using Johnson and Cook (JC) plasticity model, which is currently the most common numerical material model. In this model, along with strain hardening (work hardening) and its rate, thermal softening effects on flow stress are considered [27]. Nevertheless, the JC model utilized a simple form to combine these three parts, it only considers strain, strain rate, and temperature separately, unable to account for coupling effects and cannot determine particle-substrate bonding types [87]. The flow stress σ can be described as follow:

$$\sigma = (\mathrm{A} + \mathrm{B}\,\varepsilon_{\mathrm{pl}}^{\mathrm{n}})\,(1 + \mathrm{C}\ln\frac{\dot{\varepsilon_{\mathrm{pl}}}}{\dot{\varepsilon_0}})\,(1 - \mathrm{T}^{*\mathrm{m}}) \tag{4.4}$$

$$T^* = \begin{cases} 0 \quad for \quad T < T_r \\ \left(\frac{T - T_r}{T_m - T_r}\right) \quad for\ T_r \leqslant T \leqslant T_m \\ 1 \quad for \quad T > T_m \end{cases} \tag{4.5}$$

The parameters necessary for the Johnson-Cook model of Al are listed in Table 4.1.

4.3.2. The Mie–Gruneisen Equation of State

The Mie-Gruneisen equation of state is used to determine the hydrostatic pressure of the ductile materials. In Abaqus, the pressure P is determined as a function of the density ρ and the internal energy Em:

$$\mathrm{p} - \mathrm{p_H} = \Gamma\rho\ (\mathrm{E_m} - \mathrm{E_H}) \tag{4.6}$$

Where the Hugoniot energy $\mathrm{E_H}$ and Hugoniot pressure $\mathrm{p_H}$ are given as follow:

$$E_H = \frac{\mathrm{p_H}\,\eta}{2\,\rho_0} \tag{4.7}$$

$$p_H = \frac{\rho_0 C_0^2 \eta}{(1 - S\eta)^2} \tag{4.8}$$

The linear Us-Up Hugoniot form is defined in Eq 4.9 [103], which is derived using the linear $U_s = C_0 + sU_p$ relation. Where U_s and U_p are the linear shock velocity and the particle velocity, respectively.

$$p = \frac{\rho_0 C_0^2 \eta}{(1 - S\eta)^2}\left(1 - \frac{\Gamma_0}{2}\right) + \Gamma_0 \rho_0 E_m \tag{4.9}$$

4.3.3. Johnson-Cook (JC) Damage Model

The Johnson-Cook dynamic failure model was used to detect material failure onset. Failure occurs when the damage parameter surpasses a maximum value estimated by damage evolution [104]. Considering the influence of static pressure, strain rate, and temperature, it can be expressed in the following equation [105]:

$$\varepsilon_f = \left[d_1 + d_2 exp\left(d_3\left(\frac{\sigma_m}{\sigma_{eq}}\right)\right)\right][1 + d_4 \ln(\varepsilon^*)][1 + d_5 T^*] \tag{4.10}$$

4.4. Model validation

The current work examines numerically the cold sprayed particle deposition on a solid substrate, to study the interfacial features between the particle and substrate. First, model validation was conducted to ensure the accuracy of the numerical model for further analysis, by comparing our simulation results with those from previous research.

A. Al/Al impact

The reference numerical model of Jing Xie [77], which has been validated in previous research, is used as the validation model in our work. Simulations were performed using ABAQUS/EXPLICIT version 6.14-5 and were run under the same set of conditions of Jing Xie [77].

Initially, the simulation is based on the Lagrangian numerical approach. The aluminum particle impact on an aluminum substrate was modeled using a 2D axisymmetric model. We assumed a perfectly spherical shape of Al particle with a diameter of 20 μm. The substrate's height and radius were 5 times greater than the particle's diameter, as it shown in Figure 4.10(a).

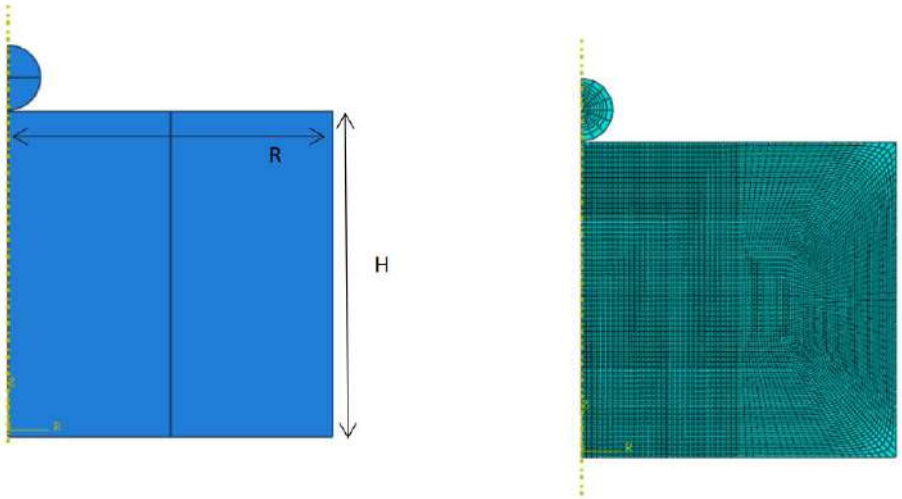
It is important to mention that in the Lagrangian approach the material thermal properties (thermal conductivity and specific heat) are implemented as temperature dependent parameters in Abaqus. The properties of Al used in the model are taken from reference [89]. The material was described using the Johnson–Cook plasticity model, which considers strain, strain rate hardening, and thermal softening. Furthermore, the Mie–Grüneisen equation of state (EOS) is used to model the material's hydrostatic response under high-rate loading.

Cold spray analysis considers strain hardening, strain-rate hardening, thermal softening, and heating from inelastic deformation. Thus, the mechanical and thermal solutions must be considered simultaneously [106]. Herein, the Dynamic Temp-Disp Explicit was considered for the 2D model. The simulation time was set at 60 ns, which was enough to observe the entire impact and bonding/rebound stage.

In ABAQUS/EXPLICIT there are two contact algorithms: general contact and contact pair. In the 2D Lagrangian model, the contact pair algorithm interaction is applied (the surface-to-surface contact). The outer spherical surface of particle (master) and the flat surface of substrate (slave) are the two surfaces included in the contact pair (Figure 4.11). For interaction property, the friction coefficient was set at 0.3, and the contact pressure-overclosure relationship was referred to as the 'Hard contact' contact model. For the meshing,

4-node thermally coupled axisymmetric quadrilateral (CAX4RT) elements were used for the 2D model (Figure 4.10 (b)).

The boundary conditions involved fixing the substrate bottom face in all directions "PINNED (U1 = U2 = U3 = 0)", and considering symmetry about the X-plane applied along the Y-axis "XSYMM (U1 = UR2 = UR3 = 0)".



(a) (b)

Figure 4. 10 (a) Geometry of the 2D axisymmetric Lagrangian model. (b) Meshing of the model

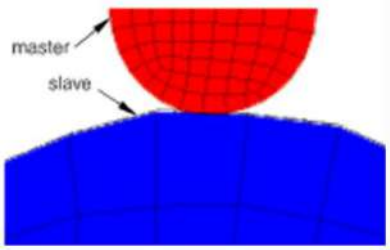


Figure 4. 11 Surface to surface contact

Figure 4.12 shows the simulation outcomes of Jing Xie [77] alongside the results of our proposed model for the deposition of a single Al particle on an Al substrate at a temperature of 300K, and at various times of the 60ns interval. The particle impact velocity and temperature were given as 500 m/s and 300 K. The consistency between both results confirms that the proposed numerical model reliably captures the cold spray behavior obtained from the reference model. As it observed, the deformation of the particle is up to the maximum, which lasts almost 40 ns until the particle rebounds off the substrate. The contact area expands as plastic strain progresses. After the particle rebounds, the contact region remains stable due to

permanent plastic deformation (extending a few micrometers beneath the substrate surface), with less elastic recovery than the plastic deformation energy [77]. The region exhibiting the highest value of PEEQ located at the bottom of the particle or on the top surface of the substrate is defined as "Key Element".

In cold spray simulations, in order to achieve strong adhesion between particles and a substrate, several critical parameters must be considered, such as the impact velocity (using the material's critical velocity required for bonding), the use of adhesion models (like cohesive zone model), selecting compatible materials, using a multiple impact model, or extending the computation time until the particle's oscillation gradually stops.

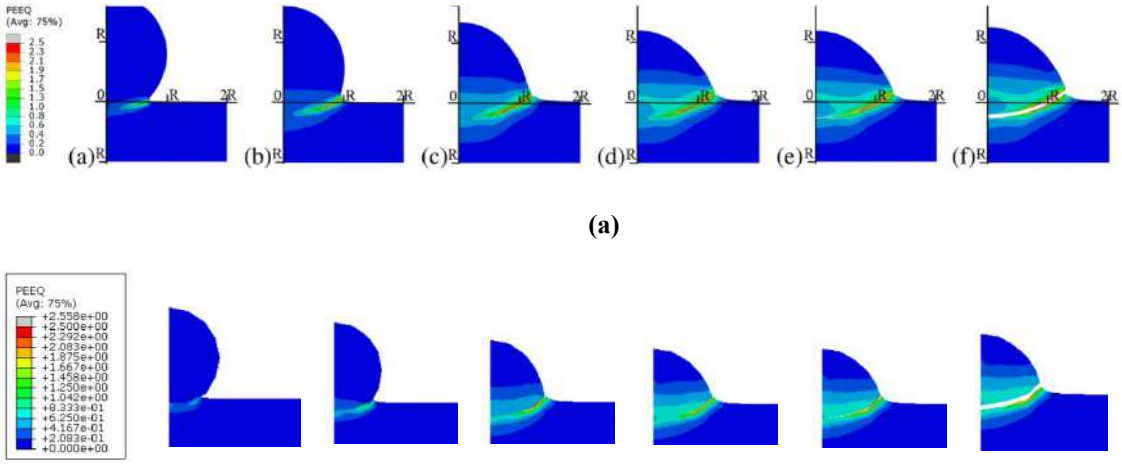


Figure 4. 12 Evolution of the equivalent plastic strain (PEEQ) in Al/Al impact: (a) 5ns, (b) 10ns, (c) 20ns, (d) 30ns, (e) 40ns, and (f) 60ns. (a) Results of [77]. (b) Our simulation's results.

Next, the same simulation under the same set of conditions is repeated using a 3D model with both the Lagrangian and CEL (Coupled Eulerian Lagrangian) approaches.

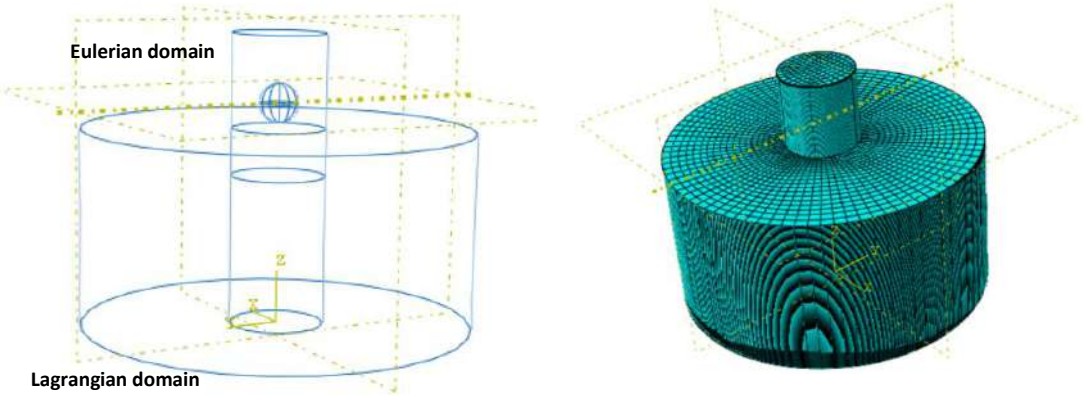
In the 3D CEL model, a general contact strategy was used as contact interaction instead of a contact pair algorithm. For the meshing, an 8-node thermally coupled linear Eulerian brick, reduced integration, hourglass control (EC3D8RT) is applied for the Eulerian part, and an 8-node thermally coupled brick, trilinear displacement and temperature (C3D8RT) for the Lagrangian part (the substrate), as it seen in Figure 4.13 (b).

Besides the boundary conditions, a predefined material assignment field is specified for the Eulerian part instance using the discrete field generated by the volume fraction tool (Appendix C).

In the 3D CEL model, the Dynamic Temp-Disp Explicit was applied, while for the 3D Lagrangian simulation, the Dynamic-Explicit procedure was chosen by taking into account the adiabatic heating effect. The properties of aluminum used in the CEL analysis are presented in Table 4.1.

Table 4.1 Material properties of Aluminum [77]

Properties (unit)	Aluminum
Density, $\rho(\mathrm{kg/m^3})$	2.7×10^3
Shear modulus, G (GPa)	27
Thermal conductivity, $\lambda(\mathrm{W/m \cdot K})$	237.2
Specific heat, $c(\mathrm{J/kg \cdot K})$	898.2
Sound velocity, $c_0(\mathrm{m/s})$	5386
Slope of U_s versus U_p, s	1.339
Grüneisen coefficient, Γ_0	1.97
Yield stress, A (MPa)	148.4
Hardening constant, B (MPa)	345.5
Hardening exponent, n	0.183
Strain rate constant, C	0.001
Thermal softening exponent, m	0.895
Melting temperature, $T_m(\mathrm{K})$	916
Reference temperature, $T_0(\mathrm{K})$	293



(a) **(b)**

Figure 4. 13 Geometry of the 3D CEL model (a), and meshing of the model (b)

Figure 4.14 depicts the evolution of the equivalent plastic strain (PEEQ) in both Lagrangian and CEL approaches. It can be observed that the aluminum particle rebound off the substrate, which indicates that the impact velocity (500 m/s) remained below the critical threshold

required for successful deposition. Thus, the kinetic energy was insufficient to trigger the adiabatic shear instability (ASI) necessary for material bonding.

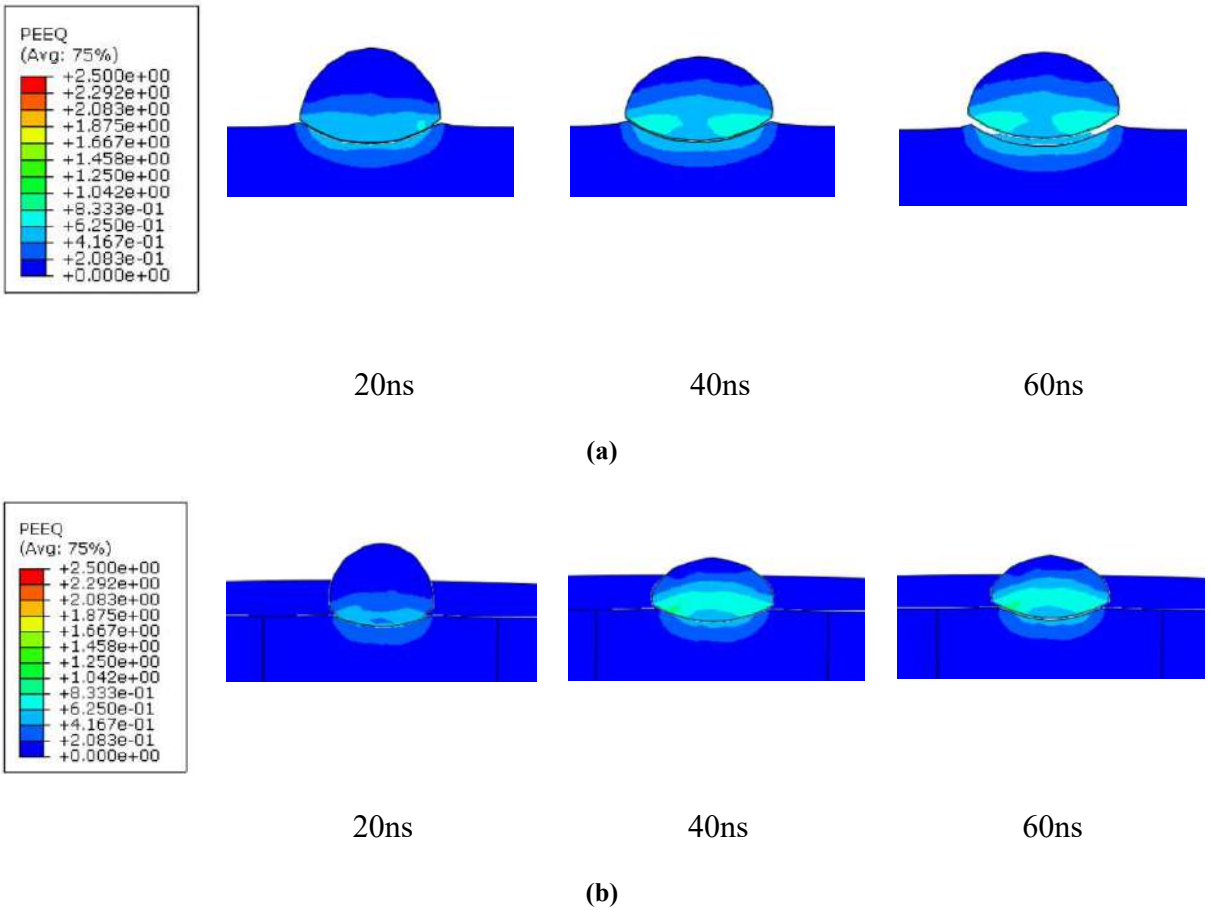


Figure 4. 14 Evolution of the equivalent plastic strain (PEEQ) in Al/Al impact. (a) 3D Lagrangian model. (b) 3D CEL model

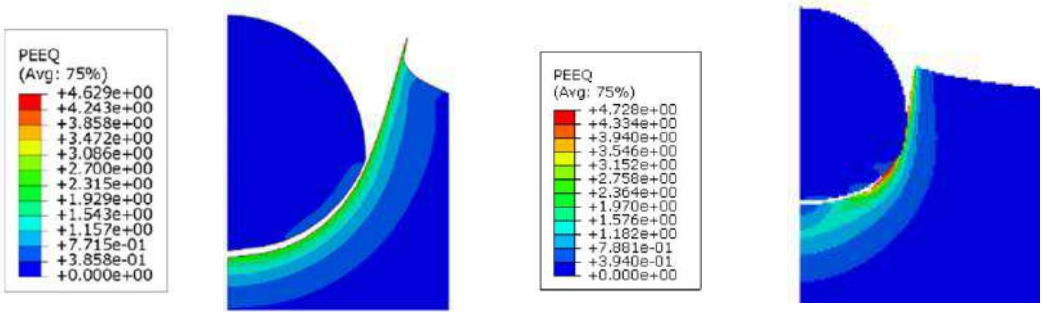
B. CrFeNi/Al impact

In this section, the single particle impact of CrFeNi on Al substrate is simulated in 2D ABAQUS/Explicit with the Lagrangian formulation to validate our numerical model using Nima Zehtabi et al [104] model as a reference. In order to compare the results, all the set-up information is the same (particle diameter of 20µm, impact velocity of 500 m/s, the friction coefficient is 0.3, and the initial temperature of particle and substrate are both 298 K).

The property parameters for Al and CrFeNi used in this simulation can be found in reference [104]. The elastic behavior of materials was described by Young's modulus and Poisson's ratio. Furthermore, in this study, unlike the Al/Al impact (first section of validation), the Johnson–Cook damage model was employed to determine the onset of material failure.

For the 2D model, the Dynamic Temp-Disp Explicit was considered; with the total solution time set as 60 ns. The contact pair algorithm with hard contact model was used as contact interaction, and friction coefficient of 0.3 with penalty formulation. Regarding meshing, CAX4RT "4-node thermally coupled axisymmetric quadrilateral" elements were used was selected for the substrate, and CAX3T "A 3-node thermally coupled axisymmetric triangle, linear displacement and temperature" for the particle. The simulation results are illustrated in Figure 4.15.

The CrFeNi particle showed significant deformation and exerted pressure on the soft Al substrate, resulting in the formation of deeper craters. As can also be noticed, there is a jetting of the matter due to the thermal softening effect. Our model exhibits a good agreement with the reference model. The observed discrepancies in the jet of matter may be attributed to the difference in meshing at the substrate between the two models. A finer mesh typically captures jet formation more accurately.



(a) **(b)**

Figure 4. 15 Evolution of the equivalent plastic strain (PEEQ) in CrFeNi/Al impact. (a) Simulation's results of [104]. (b) Our simulation's results

4.5. Results and discussion

Successful bonding in cold spray depends on several key parameters, including impact velocity, the particle/substrate material combination, and the initial temperatures of both the particle and the substrate,etc, some of which are examined in this study.

Numerous studies have proven that CEL approach analyses are more accurate in higher deformation regimes. Therefore, the CEL is applied for the following analysis of particles deformation during the spraying process. This considered, where the particle first deforms elastically, and then yields plastically, and it becomes more rigid as plastic deformation increases. The general contact algorithm is utilized in particle/substrate interactions because of the dynamic material within the Eulerian domain; it automatically detects and establishes

contact between all surfaces in the model. The volume fraction (VF) method is used to assign materials to Eulerian part instances in the CEL approach. The friction coefficient between the particle and substrate is consistently set at 0.3 for all cases.

4.5.1. The influence of impact velocity

The deformation behavior of the aluminum particle during the impact at different velocities (500, 700, and 900m/s) is modeled in this section in order to predict the critical velocity, which corresponds to the minimum particle velocity necessary to ensure effective bonding at the metal-to-metal interface. The material properties of Aluminum and the cold spray conditions can be found in Table 4.1 and Table 4.2, respectively. The Johnson-Cook damage model is utilized to express the ductile failure of the Al metal (Table 4.3) [107].

Table 4.2 Parameters of the study

	Material	Temperature (K)	Diameter (μm)	Velocity (m/s)
Particle	Al	300	25	500-900
Substrate	Al	300	-	-

Table 4.3 The Johnson-Cook damage model [107]

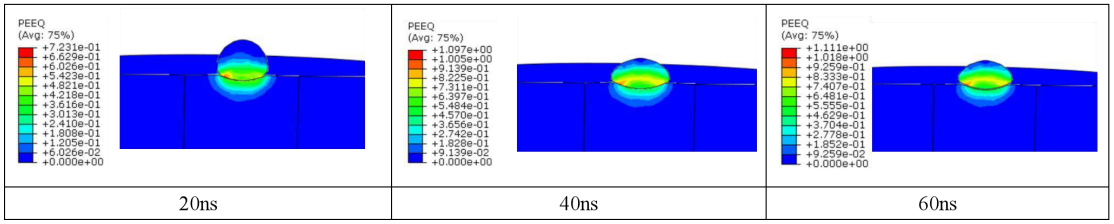
d1	d2	d3	d4	d5	Melting Temperature	Transation Temperature	Reference Strain Rate
0.071	1.248	-1.142	0.147	1	916	293	1

The plastic equivalent strain (PEEQ) is investigated to calculate the accumulated plastic deformation in the material. The contours of PEEQ are depicted in Figure 4.16. The simulation time was set to 60 ns, which was enough to observe the entire process from impact to adhesion or rebound. The high-velocity impact produces severe plastic deformation in both the particle and the substrate. As particle velocity increases, the resulting deformation increases due to the conversion of kinetic energy into plastic strain energy and the subsequent thermal softening of the material.

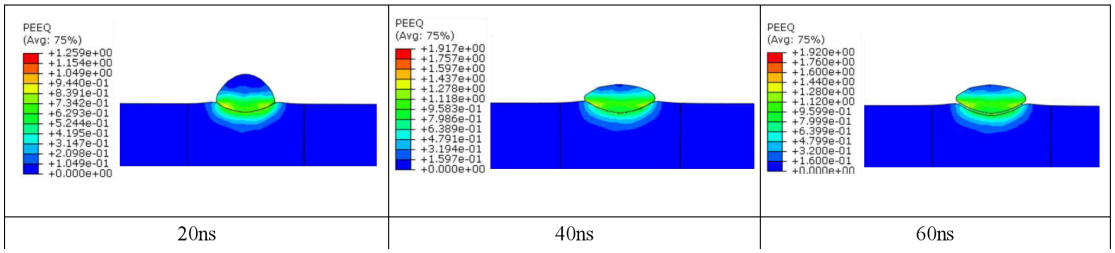
It can be observed that the Al particle lacks sufficient momentum due to its low density to achieve deep penetration into the substrate. Instead, it flattens on the surface. Consequently, no crater features are formed to provide mechanical interlocking. Despite the impact velocity

exceeding the experimental critical velocity threshold of 600–700 m/s reported for Aluminum in literature [106], particle rebound was consistently observed in the simulation. This discrepancy between the numerical results and experimental predictions can be explained by using the CEL approach used in the simulation that relies on a purely mechanical contact algorithm without an intrinsic cohesive zone model.

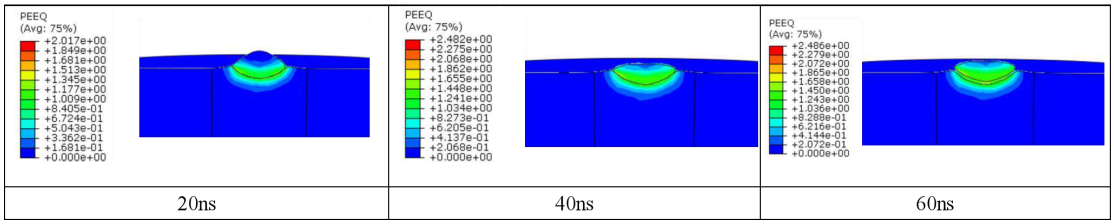
Significantly increasing the particle velocity do not necessarily guarantee adhesion. In fact, it can lead to erosion of the substrate material, as is observed in Figure 4.17. Upon increasing the impact velocity to 1700 m/s, the particle surpassed the established erosion threshold for Aluminum, which is typically cited at approximately 1250m/s [106], the particle impacts the substrate with greater energy, resulting in pits on the substrate surface due to material removal. Therefore, it can be concluded that single Al particle impacts are not recommended in our study [108].



V=500m/s



V=700m/s



V=900m/s

Figure 4. 16 Contours of the equivalent plastic strain of Al/Al impact at different velocities

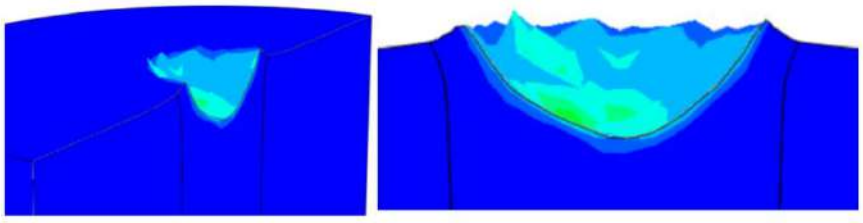


Figure 4. 17 Simulation profiles of surface erosion of Al substrate impacted by Al particle at 1700 m/s

Although cold spray is considered a solid-state process that does not really depend on the thermal energy; the temperature increase at the particle/substrate interface cannot be neglected. As seen in Figure 4.18, higher particle velocities produce greater kinetic energy, which generate localized heating; this is known as thermal softening. If the thermal softening is high enough (greater than the material's ability to harden), the material loses its structural integrity, allowing extreme deformation, and shear instability occurs [109]. Generally, in shear bands, the solid acts almost as viscous fluid, improving particle/substrate metallurgical bonding.

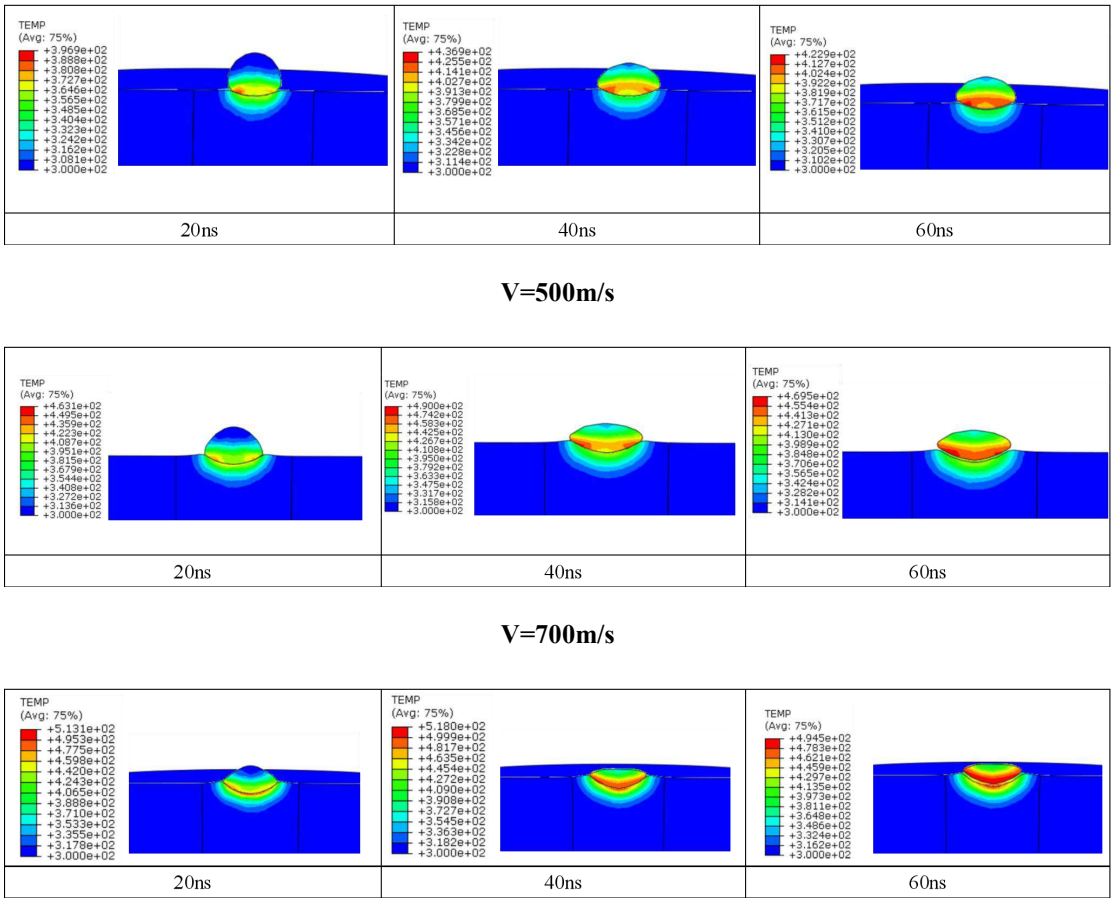


Figure 4. 18 Contours of the temperature of Al/Al impact at different speeds

In addition, the results of the temperature evolution is depicted through graphical representations in Figure 4.19. The results indicate that the temperature increases initially, this due to the adiabatic heating. Due to the short duration of the impact in CS (nanoseconds), the process is considered thermally adiabatic. The kinetic energy of the particle is converted into thermal energy; the generated heat by plastic deformation remains localized at the interface. Subsequently, the heat flows away from the interface and into the cold bulk of the substrate and the particle, once the deformation stops. The peak temperature increases with impact velocity, reaching approximately 580k at 900m/s.

Figure 4.20 (a) and (b) represent SEM photographs [110] and simulation results of Al/Al impact with 700 m/s, respectively. It can be seen that there is a high degree of similarity between the two images. They both exhibit a convex shape, which will flatten on the substrate with higher impact velocity.

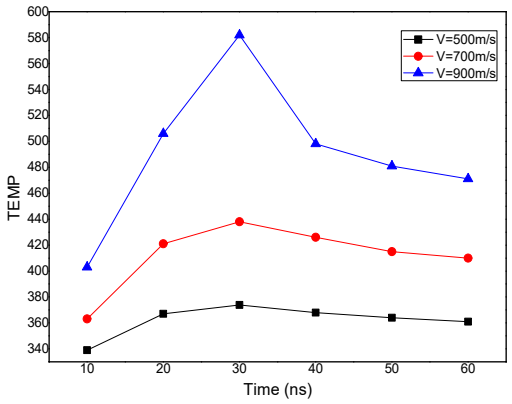
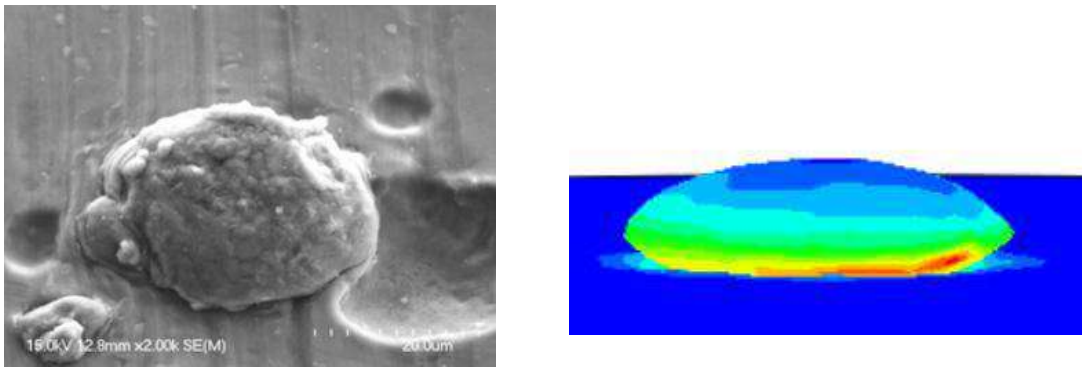


Figure 4. 19 The temperature evolution of Al/Al impact at different velocities



(a) **(b)**

Figure 4. 20 SEM image (a) and simulation results (b) of a single Al particle deposition at 700m/s

Simulation of multiple impacts:

As observed earlier, the single impact of Al particle on the Al substrate did not result in required adhesion. Thus, multi-particle impacts were simulated in this section to investigate the bonding mechanism of subsequent impacts. The multi-particle impact process indicates that following the initial coated layer, the subsequent impacts can be regarded as particles colliding on the same material, irrespective of the substrate being coated [95]. Initially, the simulation of dual successive particle impacts was conducted, under the same processing conditions of single impact, including the impact velocities and the initial temperature.

Subsequently, the study focuses on simulating multi-particle impacts. The CEL approach was used to avoid mesh distortion. The interaction between the particles is estimated using the VF method. The calculation model is given in Figure 4.21. These simulations aim to investigate whether the accumulation of thermal and kinetic energy achieved through multiple particle impacts enhances the interfacial bonding in multi-Al impact compared to single particle interactions.

Figure 4.22 and Figure 4.23 show the contours of PEEQ after the impact of dual and multiple particles at different velocities. As can be seen, the subsequent particles impact the first layer of the formed coating. Thus, the behavior observed during the second impact is quite similar to that of a single particle impacting the same material. It can be observed that the following particles compress previously deposited particles into irregular shapes, while particles in the top layer deform similarly to single-particle impacts [77]. In contrast to the single impact, no rebound was observed after 60 ns. In multi-particle impacts, subsequent particles exert a compressive force on the preceding ones, forcing more mechanical interlocking and increasing the contact area, which leads to better bonding. This is known as the tamping or

hammering effect. In addition, as the number of aluminum particles increases, so does their kinetic energy, resulting in a greater PEEQ. It is worth mentioning that distinct critical velocities were determined for the dual and multiple impact cases [95].

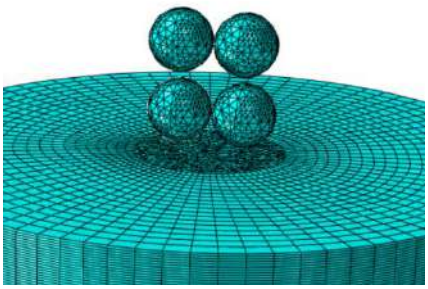
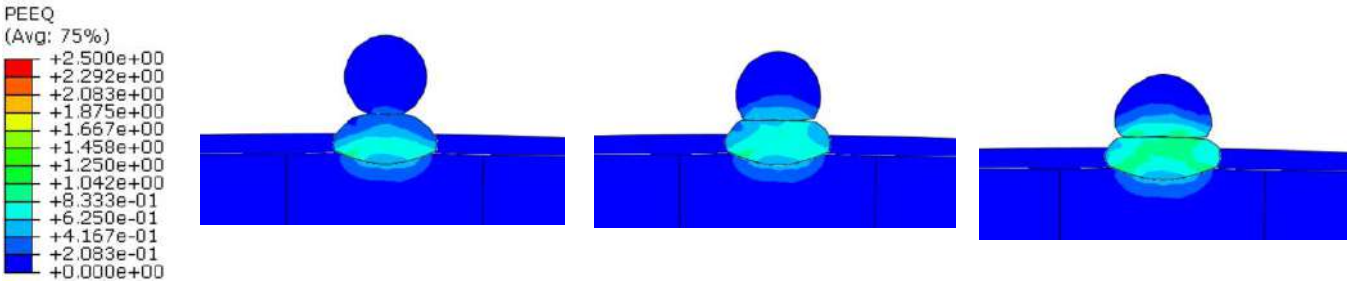
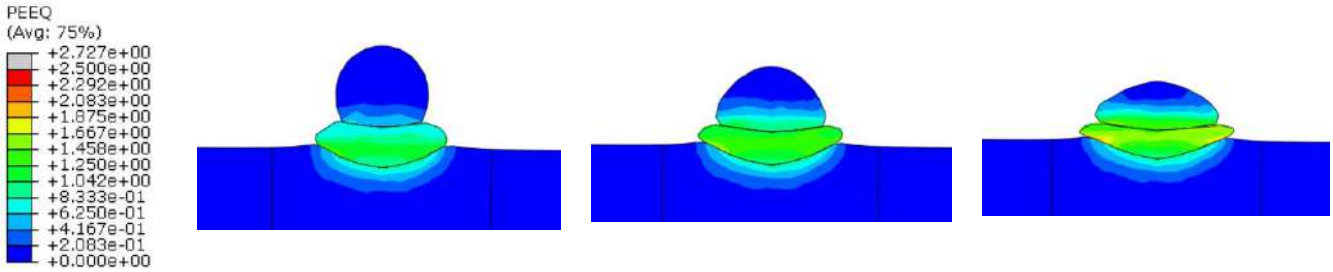


Figure 4. 21 The calculation model of the multi-impact



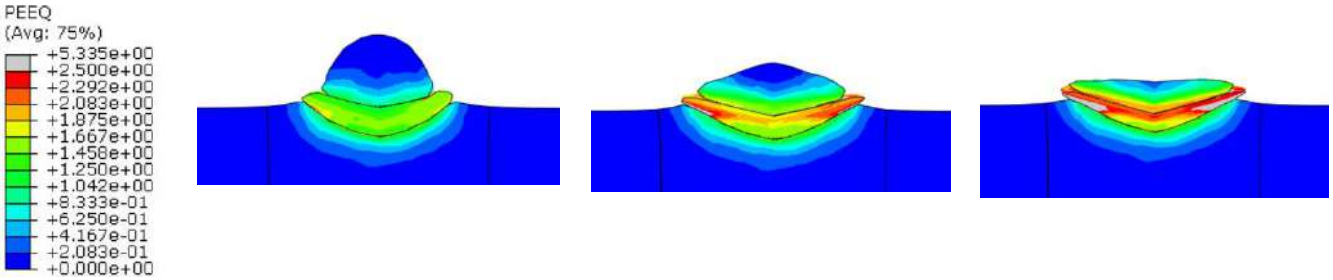
40ns 50ns 60ns

V=500m/s



40ns 50ns 60ns

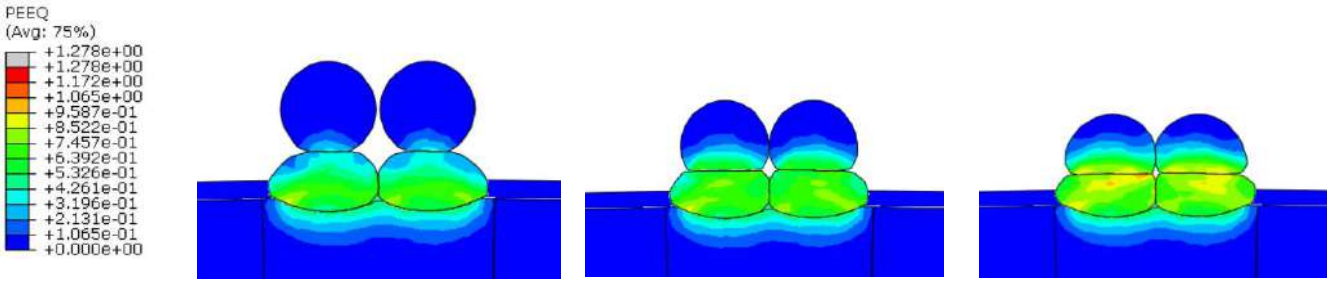
V=700m/s



40ns 50ns 60ns

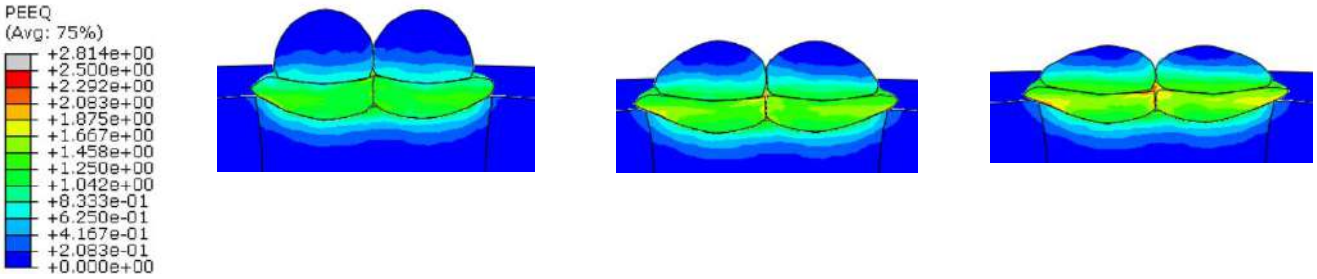
V=900m/s

Figure 4. 22 Contours of the equivalent plastic strain of dual Al particles impact at different speeds



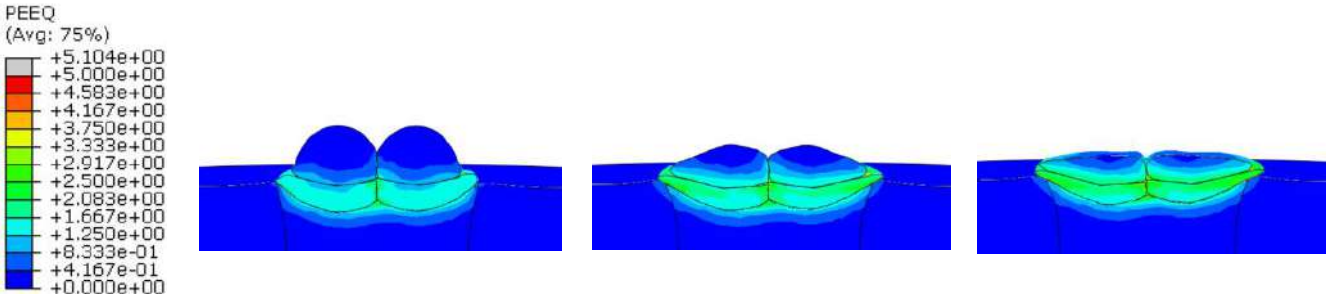
40ns 50ns 60ns

V=500m/s



40ns 50ns 60ns

V=700m/s



40ns 50ns 60ns

V=900m/s

Figure 4. 23 Contours of the equivalent plastic strain of multiple Al particles impact at different speeds

Furthermore, the contours of the temperatures in both cases are illustrated in Figure 4.24 and Figure 4.25. The findings indicate that the temperature increases not only with the particle

velocity but also with the number of impacting particles. The accumulated plastic work leads to localized thermal softening, evidenced by the formation of material jets at the edges, enhancing particle/substrate metallurgical bonding.

Additionally, the findings reveal that there is a void between the impacting particles, which leads to less effective deposition. Therefore, a smaller Al particle at the range of 15um was included in the numerical model (Figure 4.26). The result in Figure 4.27 shows a better deposition of the particles.

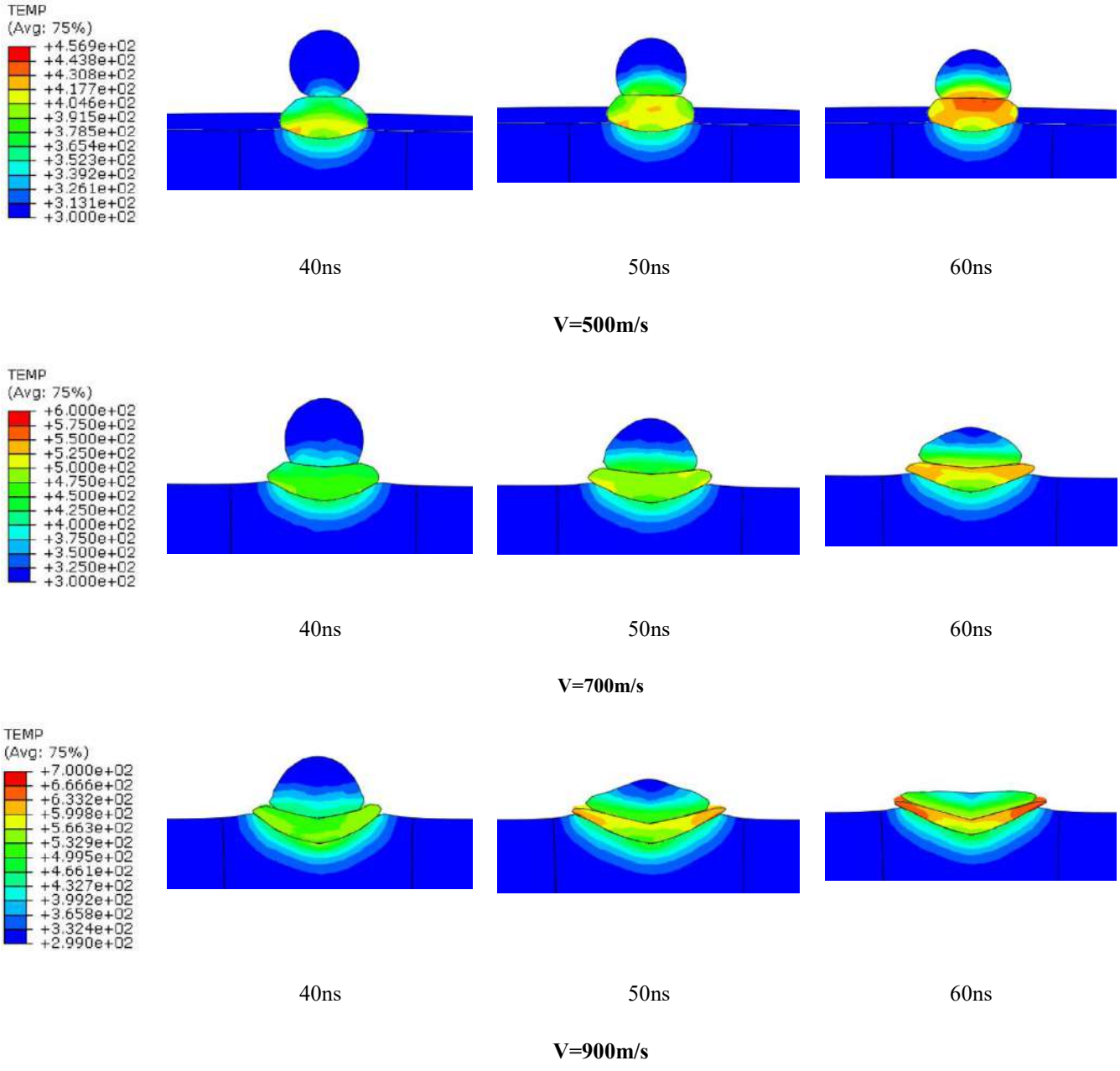
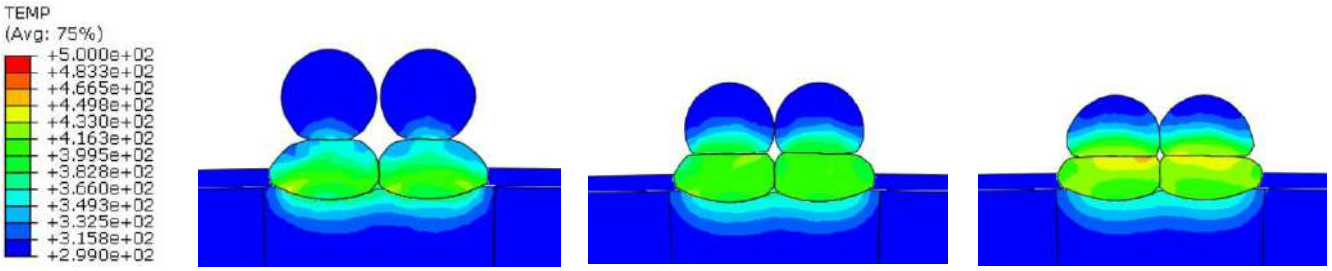
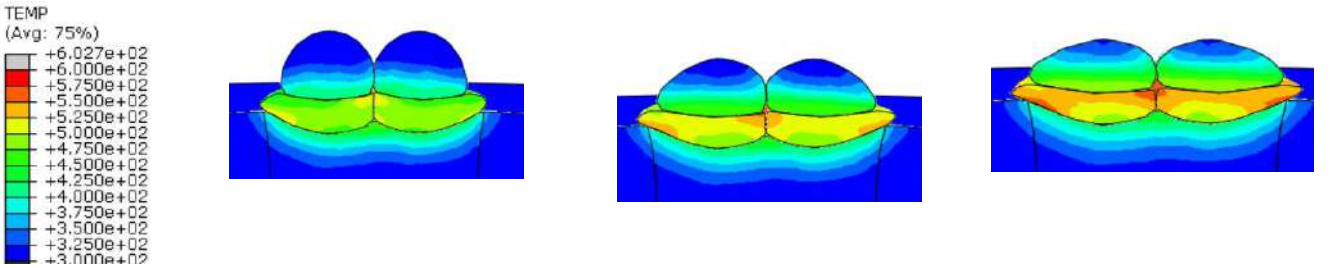


Figure 4. 24 Contours of temperature of dual Al particles impact at different speeds



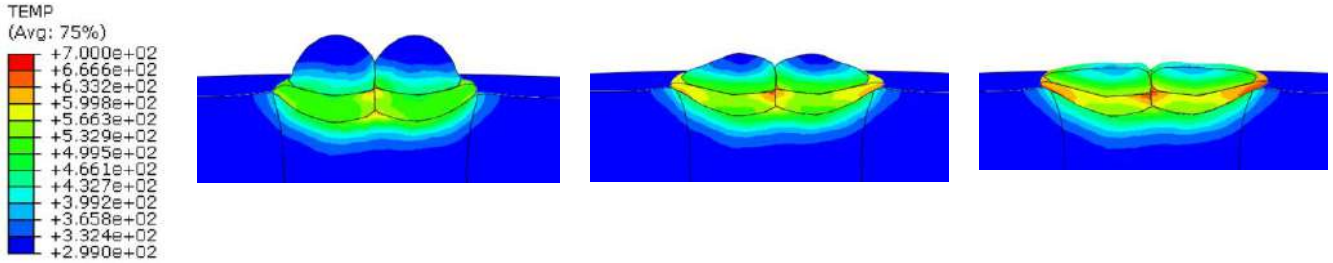
40ns 50ns 60ns

V=500m/s



40ns 50ns 60ns

V=700m/s



40ns 50ns 60ns

V=900m/s

Figure 4. 25 Contours of temperature of multiple Al particles impact at different speeds

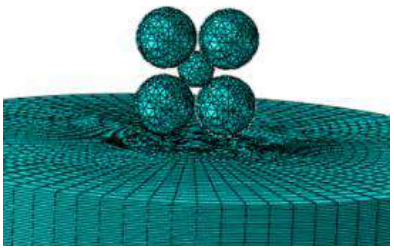


Figure 4. 26 Computational domain of multi-particles impact model

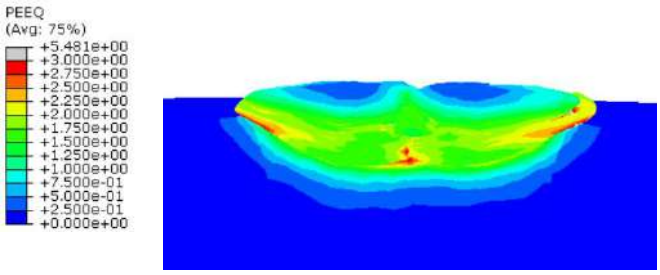


Figure 4. 27 PEEQ contour of multi-particles impact at a velocity of 900 m/s

4.5.2. The influence of particle-substrate material combinations

In this section, the investigation is expanded to include dissimilar materials. Simulations of various material combinations were conducted to determine the appropriate materials for the CS. As mentioned before, to avoid the excessive mesh distortion that leads to termination of the calculation after a short time, the CEL is employed.

Generally, in CS there exist four types of impact depending on the materials properties; these impact cases are classified as follows: soft/soft, hard/soft, soft/hard and hard/hard. Additionally, it has been defined in literatures different impact modes resulting from this combination: co-deformation (soft/soft and hard/hard), splatting (soft/hard) and penetration (hard/soft). The Al/Al impact can be considered as a soft/soft impact according to the hardness of the substance. We extend the study to include Cu/Al, Al/Cu, Cu/Cu, and Cu/Ti6Al4V impacts (Table 4.7).

The properties of the materials used in these simulations are listed below (Table 4.4).

Table 4.4 Material properties

	Al [111,112]	Cu [111,113]	Ti-6Al-4V [108]
Density (kg/m^3)	2700	8960	4500
Thermal properties			
Heat capacity (J/kg K)	920	383	612
Thermal conductivity (W/m K)	236	386	7.955
Inelastic heat fraction	0.9	0.9	0.9
Mechanical properties			

Shear modulus (GPa)	27	44.7	44
Poisson's ratio	0.3	0.34	0.3
Yield strength, A (MPa)	148.4	90	862
Hardening coefficient, B (MPa)	345.5	292	331
Strain hardening exponent, N	0.183	0.31	0.34
Softening exponent, M	0.895	1.09	0.8
Melting temperature (K)	916	1356	1878
Reference temperature (K)	298	298	298

Table 4.5 Equation of state (Eos) [108]

	Al	Cu	Ti-6Al-4V
Sound velocity ms^{-1} , C	5386	3940	5130
Slope, S	1.339	1.489	1.028
Gruneisen coefficient, Γ	1.97	2.18	1.23

Table 4.6 Johnson–Cook damage model

	Al [107]	Cu [108]	Ti-6Al-4V [108]
d_1	0.071	0.54	-0.009
d_2	1.248	4.89	0.25
d_3	-1.142	3.03	0.5
d_4	0.147	0.014	0.014
d_5	1	1.12	3.87
Reference strain rate $\boldsymbol{\varepsilon}$ (s^{-1})	1	1	1

Table 4.7 Types of impact

Material pair	Al/Al	Al/Cu	Cu/Al	Cu/Cu	Cu/Ti-6Al-4V
Type	softs/soft	soft/hard	hard/soft	hard/hard	hard/hard

A. Evolution of equivalent plastic strain

The effectiveness of coatings in CS process does not only rely on the impact velocity but also the combination of the materials used. Initially, to elucidate the deformation characteristics of

particles in various coating materials, this study examines their behavior under different impact configuration and velocities. Figure 4.28 illustrates the contours of the PEEQ after the impact of Al/Cu, Cu/Al, Cu/Cu, and Cu/Ti-6Al-4V at velocities of 500, 700, and 900 m/s. It is important to mention that the particles and substrates are considered to be oxide-free in all cases.

It is evident from the results that the particle deformation is highly reliant on particle velocity and material properties. As seen in Figure 4.28, in the soft/hard case, the particle appears to be on the point of rebounding, indicating that it has not reached the critical velocity. However, the particle attaches to the substrate as the impact velocity increases. At 900 m/s the particle is flattened and the copper substrate does not exhibit a large deformation, which indicates the splatting mode. The results agree well with the numerical outcomes of the references [77,87] and the experiments of reference [114]. The substrate's hardness causes the soft particle to deform. The impact energy dissipation occurs via a combination of interfacial plastic flow and adiabatic heating, facilitating the thermal softening necessary for material jetting. In addition, there is no sign for substrate erosion at 900 m/s, it can be suggested a maximum PEEQ plateau at this velocity , where any further increase in velocity does not show a significant increase in the plastic deformation [115].

For the case of hard/soft, the bonding occurs at velocity of 500 m/s. A similar result was observed in reference [116,117]. The crater depth in the Al substrate significantly increases as contact time increases, and due to the substrate's softness, it does not induce substantial deformation of the Cu particle; rather, the particle penetrates the substrate, signifying the penetration mode. Additionally, strong mechanical interlocking is observed.

In the hard/hard (Cu/Cu) impact, the results show a strong particle/substrate bonding for all velocities. Thus, it can be concluded that the critical velocity is less than 500m/s, which is consistent with numerical analysis obtained by the works in references [115,118]. It can be observed that at 900 m/s, the substrate surface is severely eroded, hence it may be stated that this velocity can be characterized as the erosion velocity; consequently, the efficacy of the coating is compromised as a direct result of the erosion.

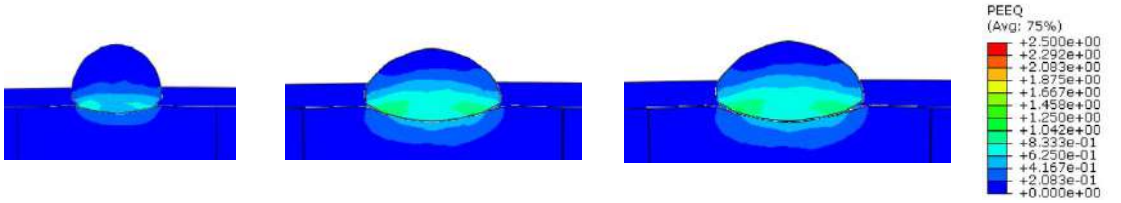
It is important to note that the particle/substrate deformation mechanisms are different between the combination of dissimilar materials and identical material. For the Al/Al and Cu/Cu cases, it is evident that the particle’s deformed shape (its height-to-width ratio)

primarily corresponds to the substrate's crater depth, indicating that the co-deformation impact mode is predominant.

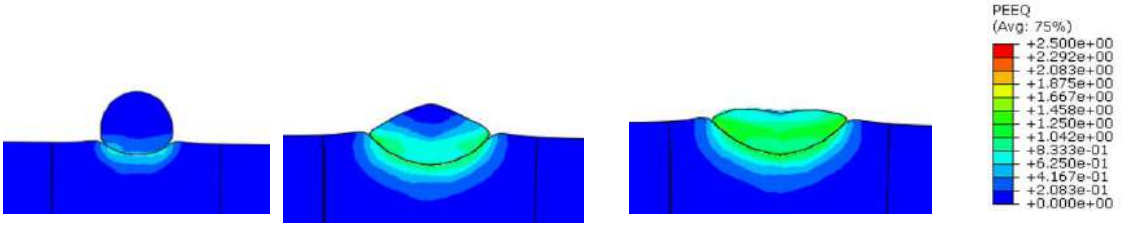
Additionally, we examined hard/hard impact involving different materials, Cu particle and Ti6Al4V substrate. At 500m/s, after 60 ns, the particle is flattened without penetrating the substrate, which is consistent with the simulation results of Hu W. J. [108], although a different approach (smoothed particle hydrodynamics, SPH) was used in their work. As the velocity increases, the particle bounce off the substrate, and the substrate does not develop a deep crater due to the high yield stress of the material. However, this is not the case when using the SPH method, where the deformation depth of the substrate increases due to stiffness of SPH particle.

It can be concluded from these findings that the physical and mechanical properties of the particle and substrate, (e.g. density and hardness), have a significant impact on the coating deposition during the CS procedures.

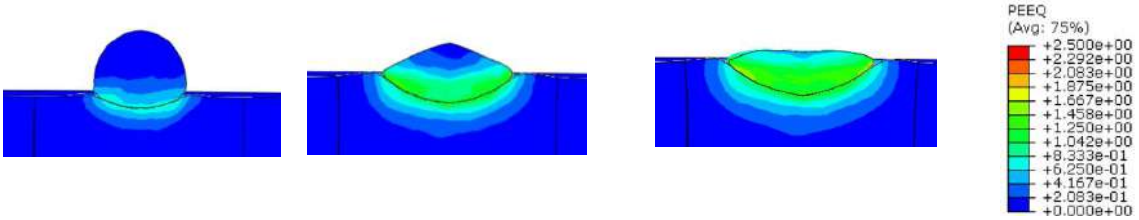
Al/Cu



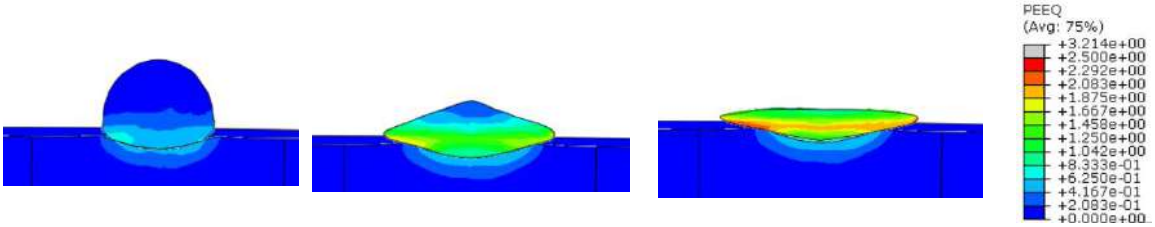
Cu/Al



Cu/Cu



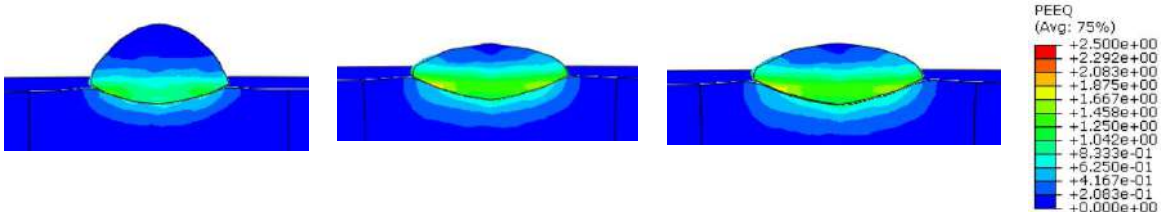
Cu/Ti6Al4V



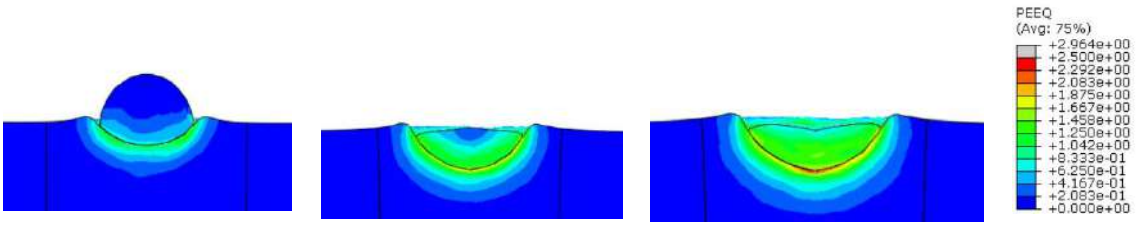
t=20ns t=40ns t=60ns

V=500m/s

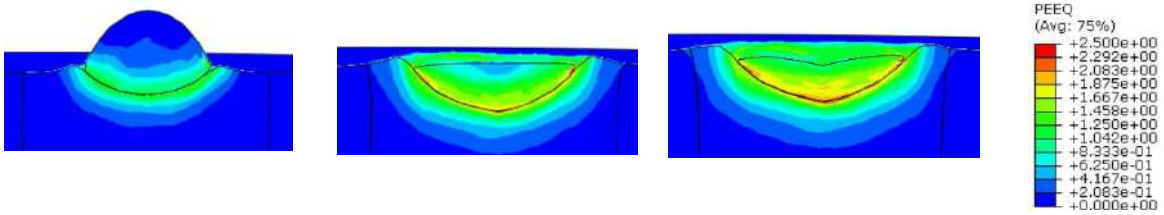
Al/Cu



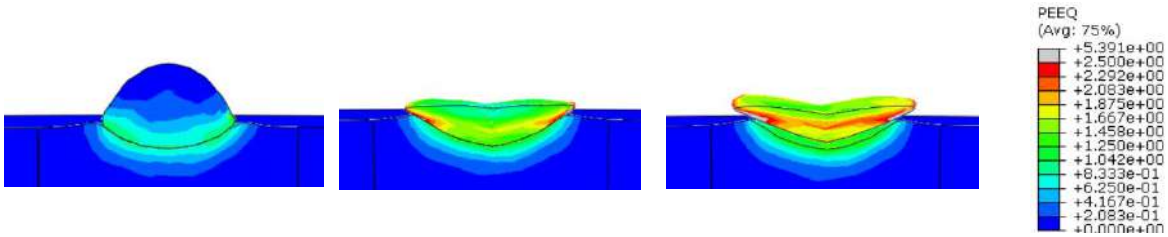
Cu/Al



Cu/Cu



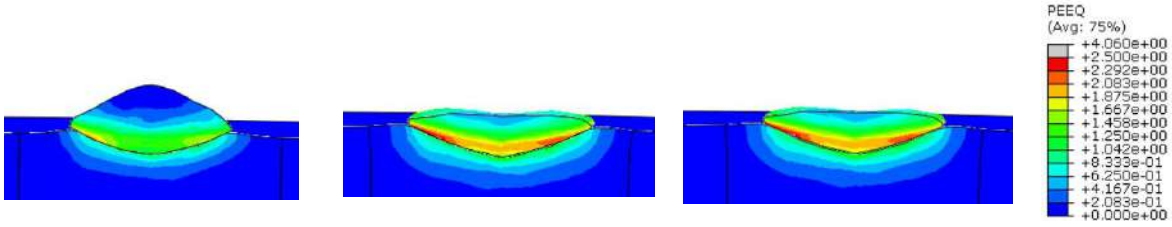
Cu/Ti6Al4V



t=20ns t=40ns t=60ns

V=700m/s

Al/Cu



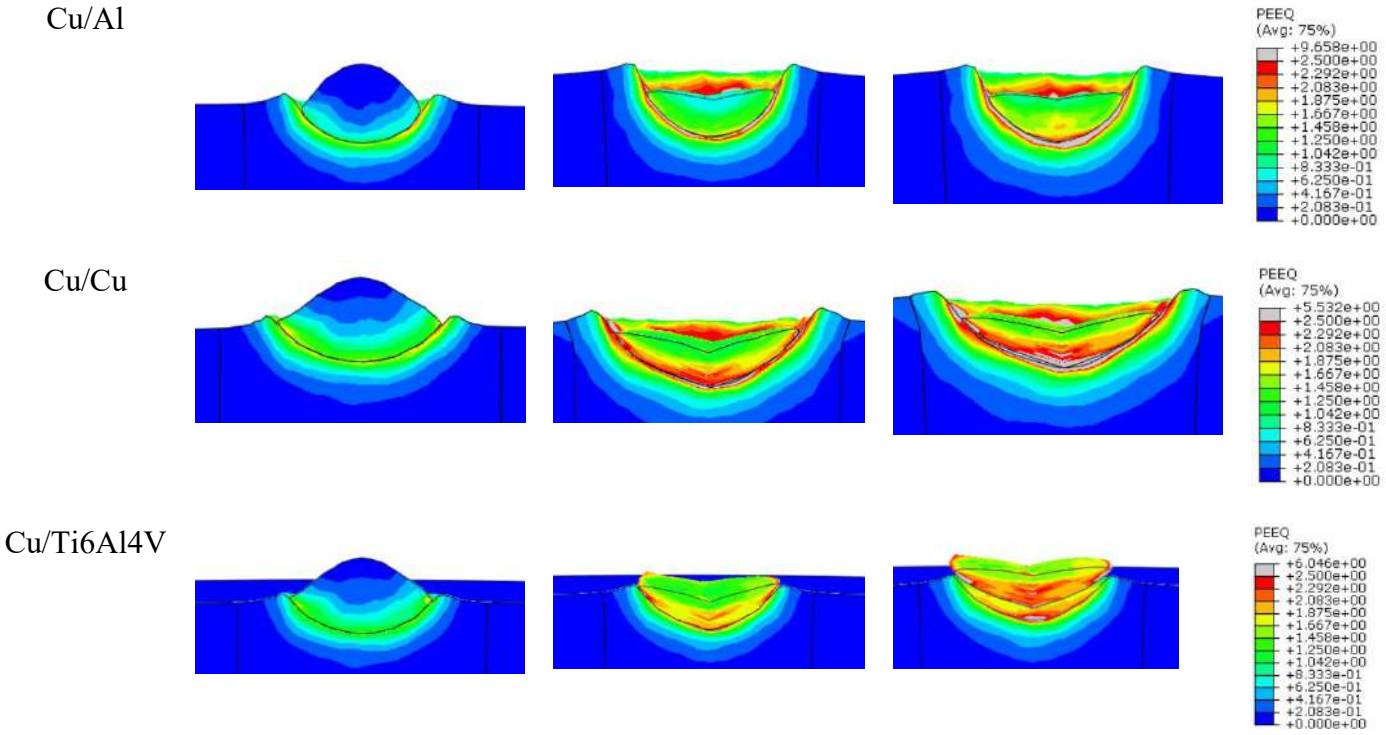


Figure 4. 28 PEEQ of Al/Cu, Cu/Al, Cu/Cu and Cu/Ti6Al4V impacts within 60ns at 500, 700 and 900m/s

B. Compression ratio (CR) and comparative deformation ratio (CDR)

Generally, in CS process, deformation occurs in both particle and substrate surface. To predict the degree of the sprayed particles deformation, a compression ratio (CR) is proposed. It is defined as:

$$\mathrm{CR} = \frac{D_p - h_p}{D_p}\ 100\% \quad [111,119] \tag{4.11}$$

The compression ratio was found to be independent of the mesh size. This means that the CR results do not change by changing the mesh size in the particle; hence, deformation of the particle is determined only by the physical characteristics of the model.

Figure 4.29 depicts the compression ratio (CR) as a function of particle velocity for the soft/soft, soft /hard, hard/hard and hard/soft impacts.

It is clear that the CR increases with the impact velocity in all cases. However, in the Cu/Ti6Al4V impact the CR decreases after 700m/s. This is due to the strong elastic rebound of the particle, where partially restoring its initial high.

It is worth noting that a higher velocity was needed for the soft material (Al particles) to achieve the same compression ratio as that of the hard material (Cu particles). This indicates that regardless of the substrate material (Al, Cu or Ti6Al4V), Cu particles undergo more severe deformation than Al particles at low velocities, due to its high density, thus high kinetic energy. Consequently, particle density significantly affects the deformation behavior [111]. Nevertheless, upon impacting the Cu substrate, the Al particle experiences severe deformation due to the hardness of the substrate. Since the CR does not consider the substrate deformation, the comparative deformation ratio (CDR) is required to evaluate how much the substrate deforms compared to particle deformation.

The CDR is defined by the ratio of dimensionless crater depth and the CR, as follow:

$$\mathrm{CDR} = \frac{h^*}{CR} \tag{4.12}$$

Where h^* is the dimensionless crater depth: $h^* = \frac{h}{D_p}$

The results in Figure 4.30 show that the CDR increases with the particle velocity in all cases, except for the Al/Cu impact (a decrease is observed at velocities beyond 700 m/s). Additionally, it is observed that the CDR in the Cu/Cu and Cu/Al is higher than all the other cases throughout the entire velocity range. These scenarios also exhibit the largest crater depth (Figure 4.31). The results reveal that for the Cu/Al case, both the particle and the substrate undergo similar degrees of deformation (CDR=1) at 700 m/s. While in the other cases, the crater depth of the substrate is always less than the CR.

In the Al/Cu case, as the impact velocity increases; the particle undergoes greater deformation compares to the substrate due to the higher hardness of Cu relative to Al material, resulting in a low CDR, which is harmful to the bonding mechanisms.

Additionally, an increased CDR can result in substrate erosion. Therefore, effective bonding can be achieved only with a sufficiently large compression ratio and a proper comparative deformation ratio [95].

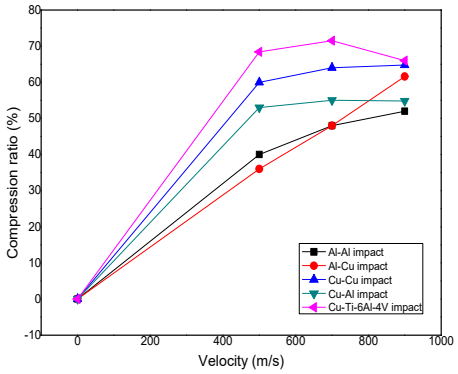


Figure 4. 29 Evolution of particle compression ratio with different velocities

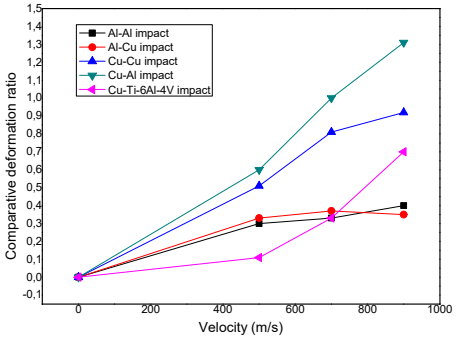


Figure 4. 30 Evolution of comparative deformation ratio with different velocities

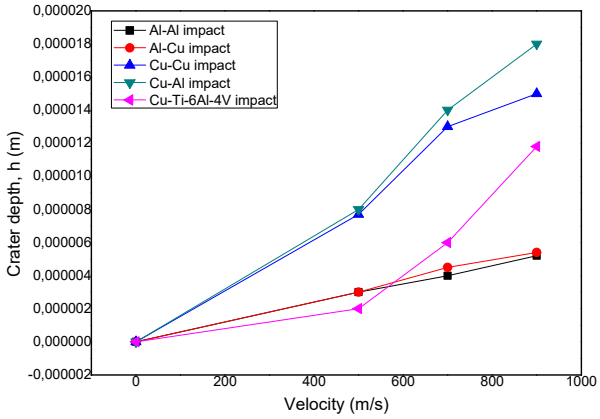


Figure 4. 31 Evolution of substrate crater depth with different velocities

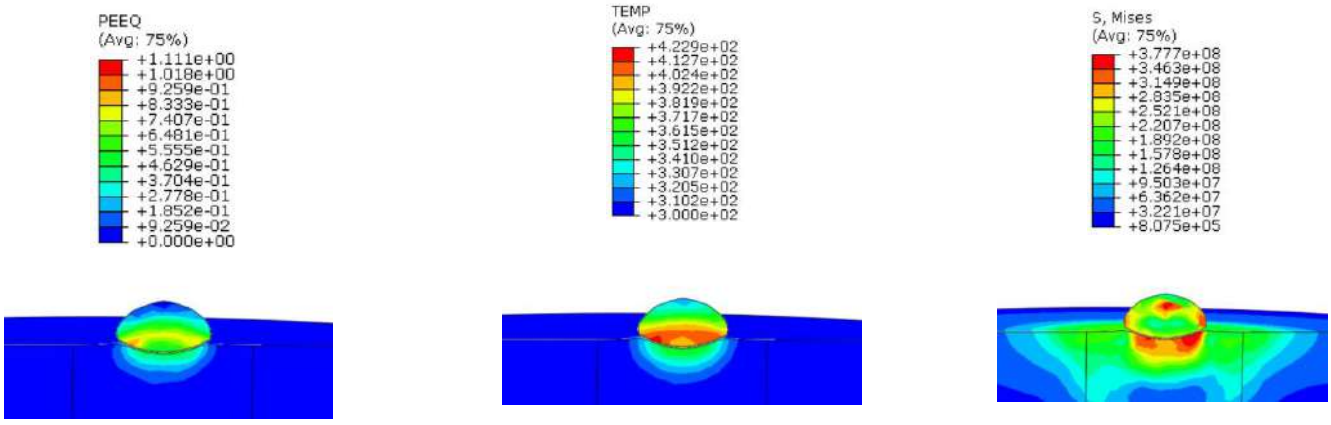
C. Evolution of PEEQ, temperature, and Von-Mises stress

This section presents the simulation results of PEEQ, temperature, and von Mises stress for different material combinations (Al/Al, Al/Cu, Cu/Al and Cu/Cu), evaluated at 60ns after impact (Figure 4.32).

The contours show that the maximum PEEQ is localized at particle/substrate interface (contact zone), and it increases with the particle velocity. As a result, the highest temperature values are likely to occur in these regions due to the adiabatic process in cold spray. The highest PEEQ and temperature are observed in the case of Cu/Al at 900 m/s. The increase in temperature promotes material softening, enhancing metallurgical bonding. Therefore, it can be said that mechanical and metallurgical bonding coexist in the Cu/Al case.

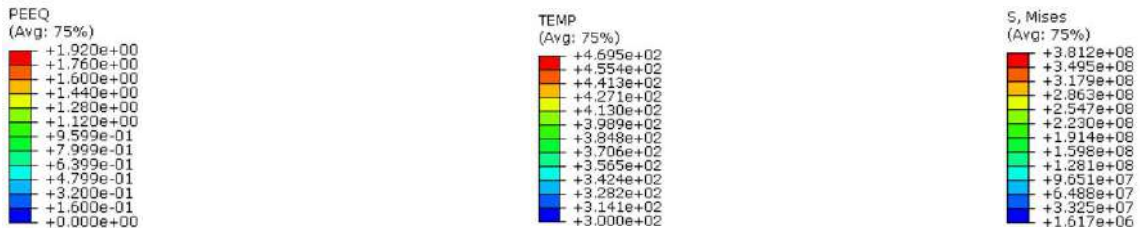
The maximum von Mises stress concentrates at the contact interface, reaching a peak value of approximately 435 MPa. This value exceeds the dynamic yield strength of the Al material, triggering rapid plastic deformation, which results in PEEQ buildup. This intense deformation leads to localized adiabatic heating, as mechanical work is converted into thermal energy. Furthermore, shear stress (deviatoric stress) is the primary factor responsible for material deformation and jetting at the interface, as the normal pressure (hydrostatic) does not contribute to plastic yielding of the Al [120]. When a Cu particle impacts the substrate, the substrate experiences greater stress compared to when an Al particle impacts it, due to the high density of the copper.

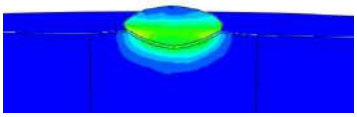
PEEQ **Temperature** **von-Mises stress**

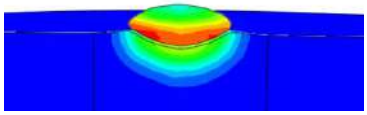


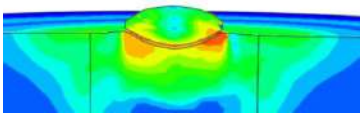
V= 500m/s

PEEQ **Temperature** **von-Mises stress**



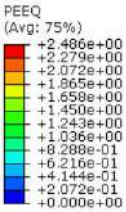


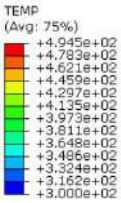


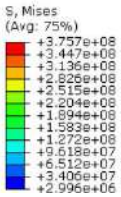


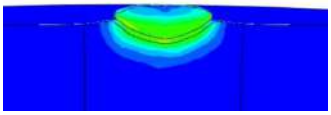
V= 700m/s

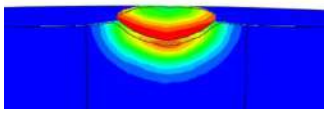
PEEQ **Temperature** **von-Mises stress**

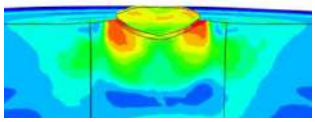








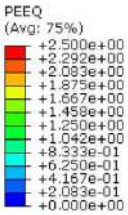


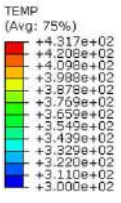


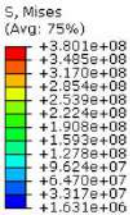
V= 900m/s

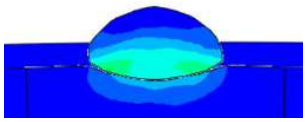
(a) Al/Al impact

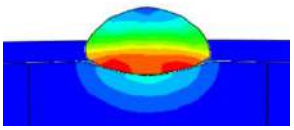
PEEQ **Temperature** **von-Mises stress**

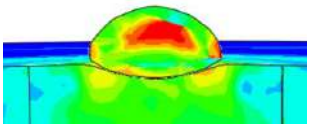






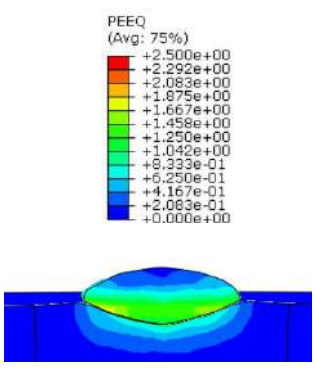


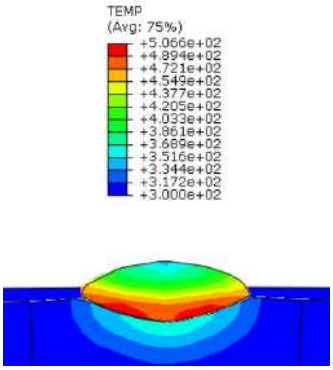


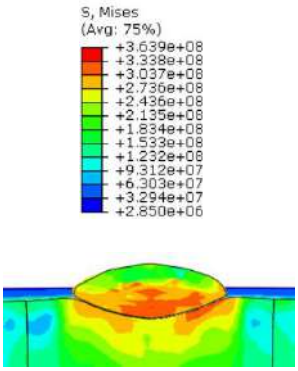


V=500m/s

PEEQ **Temperature** **von-Mises stress**

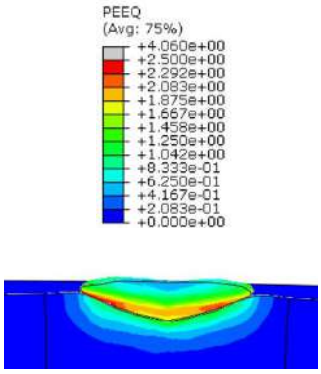


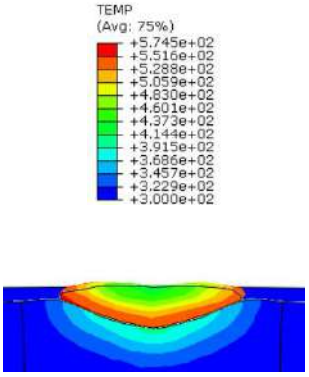


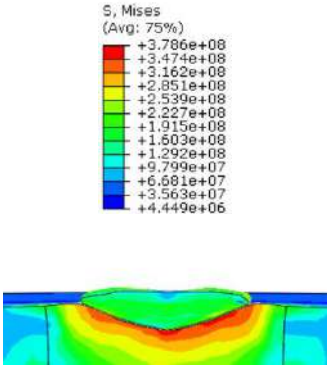


V=700m/s

PEEQ **Temperature** **von-Mises stress**



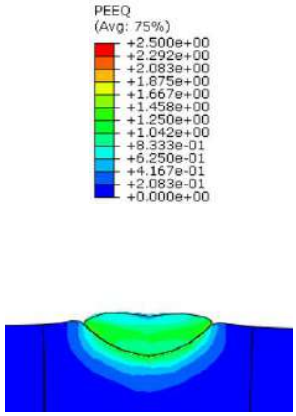


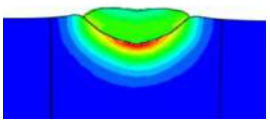


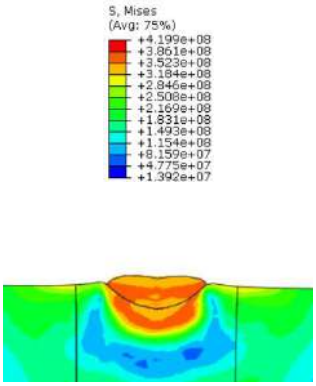
V=900m/s

(b) Al/Cu impact

PEEQ **Temperature** **von-Mises stress**

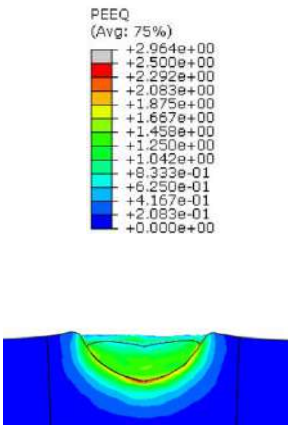


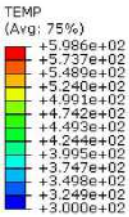


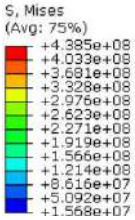


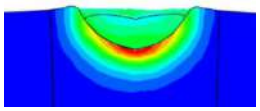
V=500m/s

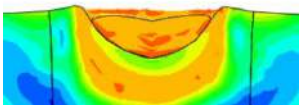
PEEQ **Temperature** **von-Mises stress**







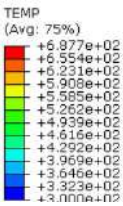


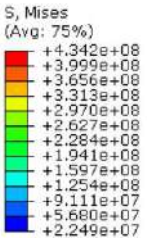


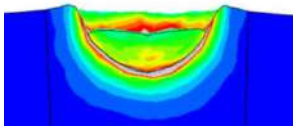
V=700m/s

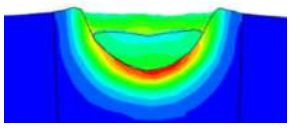
PEEQ **Temperature** **von-Mises stress**

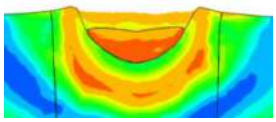








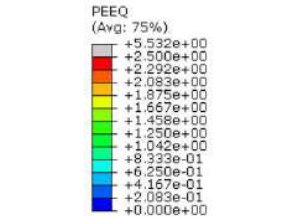


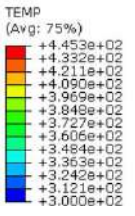


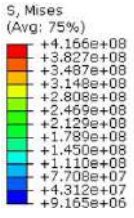
V=900m/s

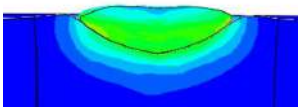
(c) Cu/Al impact

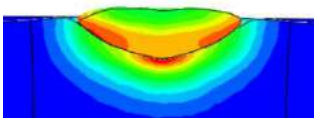
PEEQ **Temperature** **von-Mises stress**

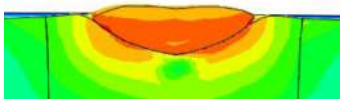






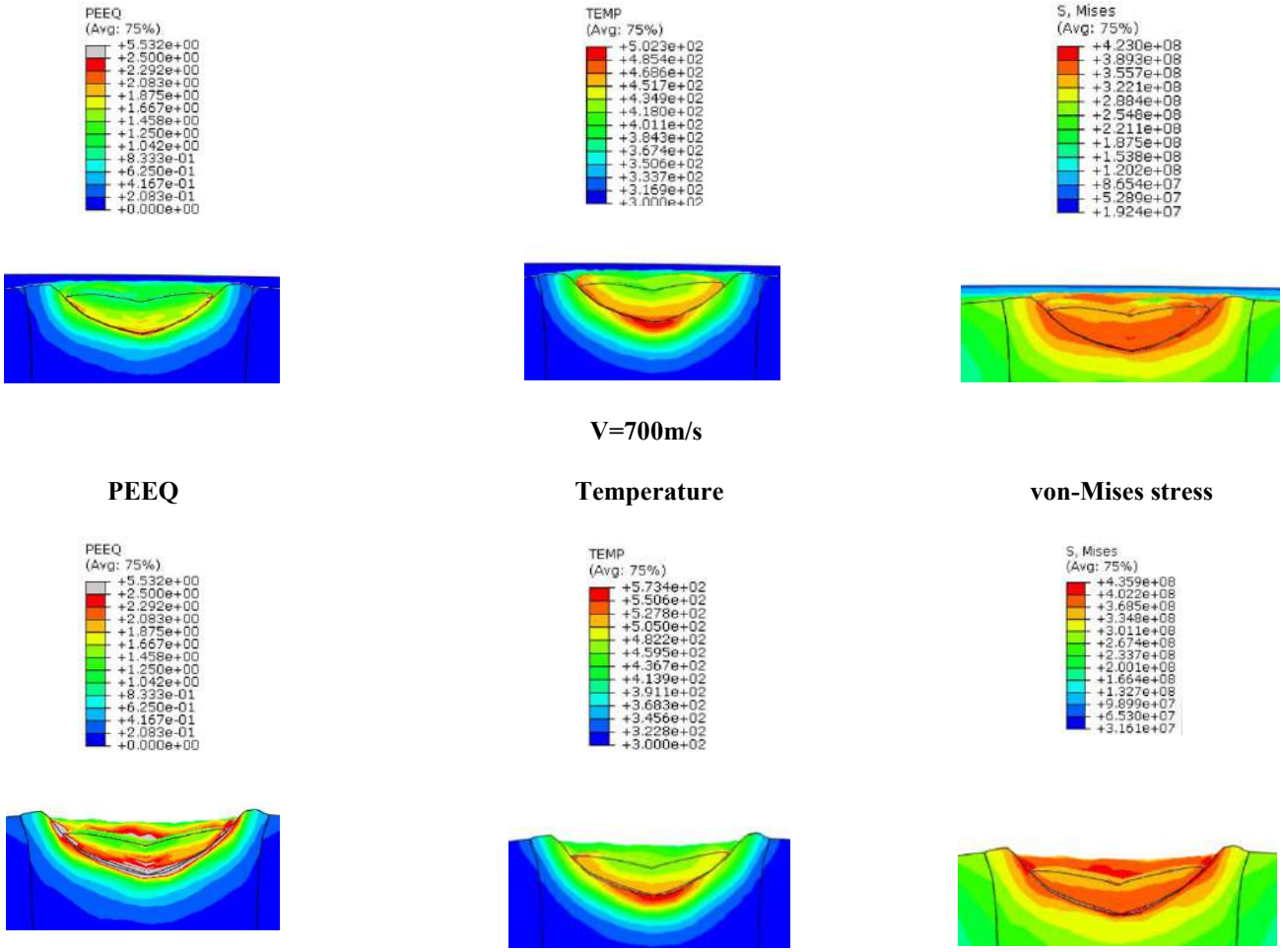






V=500m/s

PEEQ **Temperature** **von-Mises stress**



(d) Cu/Cu impact

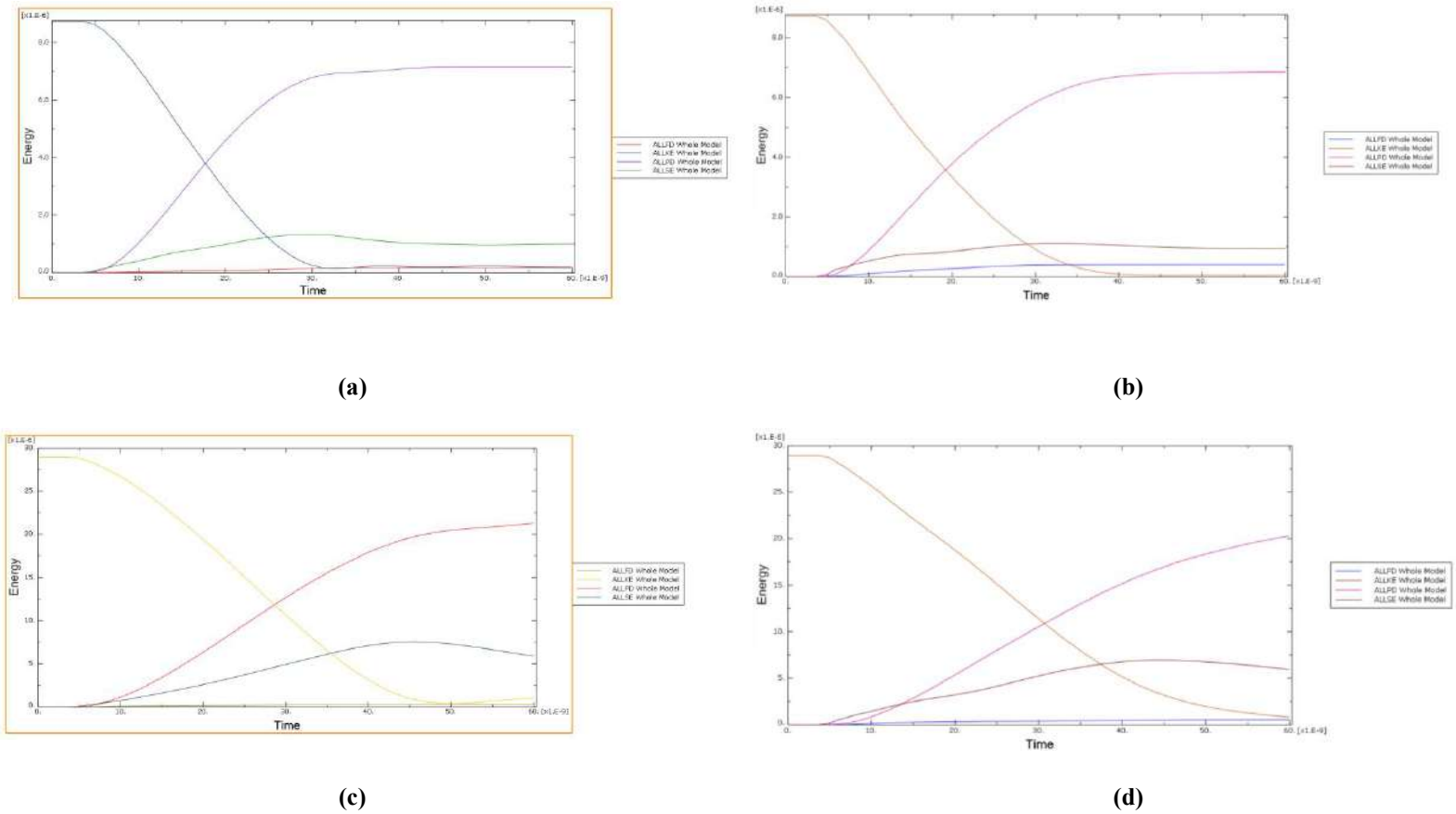
Figure 4. 32 Evolution of PEEQ, temperature and von Mises of all cases after 60ns at different velocities

D. Evolution of energy: ALLKE, ALLFD, ALLPD, and ALLSE

Figure 4.33 shows the energy evolution process over time of the whole model during the simulation of different materials combination (Al/Al, Al/Cu, Cu/Al, and Cu/Cu), where different forms of energy are represented: kinetic energy (ALLKE), frictional dissipation (ALLFD), plastic dissipation (ALLPD), and recoverable strain energy (ALLSE).

The results show that, although all particles impact at the same velocity (900 m/s), the Cu particles possess higher kinetic energy than Al particles. The reason is that denser particles possess greater initial kinetic energy [108]. Therefore, particle deformation is significantly affected by its density [111]. The increase in kinetic energy promotes more severe plastic deformation, leading to higher plastic dissipation within the material [104].

It can be observed that recoverable strain energy (ALLSE) is low throughout the process, which indicates that most deformation is plastic and irreversible as is common in the CS process. In addition, the friction dissipation (ALLFD) is very low that can be neglected in all cases. Since the impact is normal to the substrate, there is less sliding of the particle.



(a) **(b)**

(c) **(d)**

Figure 4. 33 Energy evolution process over time at impact velocity of 900m/s. (a) Al/Al, (b) Al/Cu, (c) Cu/Al, (d) Cu/Cu

4.5.3. Influence of particle and substrate preheating

The previous results indicated that during the impact of Cu particle onto Al substrate at 500m/s, the particle experiences significant flattening. Also, a strong particle/substrate bonding was observed. In addition, a high compression ratio (CR) and a proper comparative deformation ratio (CDR) are achieved at this velocity, indicating good deposition properties. Therefore, the Cu/Al case is chosen for the subsequent simulations to study the influence of particle and substrate preheating.

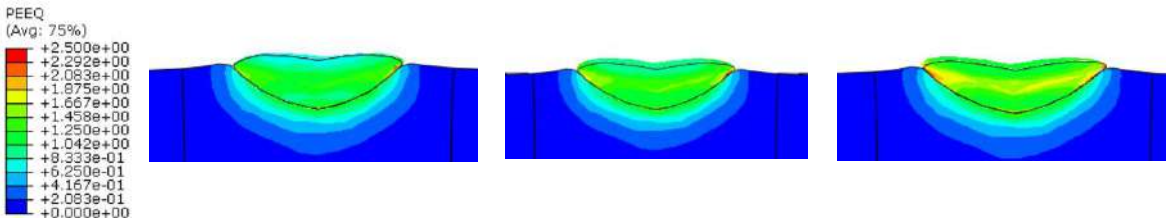
First, we examine the particle preheating. Figure 4.34 presents the PEEQ results of the Cu particle impacts with 500m/s and at different temperatures (500, 700 and 900 K) on Al substrate with a constant temperature of 300 k. Many studies [121,109] have indicated that the

preheated particles experience thermal softening, which increases the deformation degree. However, in this case of Cu/Al, as can be seen, preheating the particle has no significant effect on its deformation behavior or that of the substrate. Although increasing the temperature to 900 K (less than the material melting point), the Cu particle experienced limited plastic deformation with slight PEEQ localized primarily at the edges. Therefore, it can be concluded that in the Cu/Al case bonding is governed by the high particle velocity, not particle preheating.

Subsequently, we investigate the effects of substrate preheating where Cu particle impacts with 500m/s and a constant temperature of 300 K. It is evident from Figure 4.35 that the particle almost retains its shape as the substrate temperature increases. Increasing the temperature of the Aluminum substrate induces thermal softening, reducing the material's yield strength. It was found that this deformation behavior is favorable for particle/substrate mechanical interlocking [122,123,124] and it improves coating bonding [91].

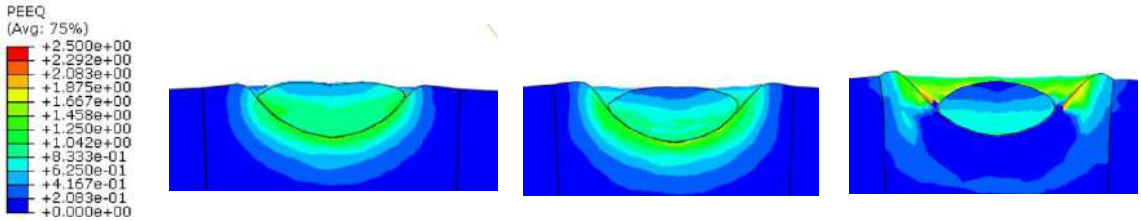
At 500 K and 700 k, the PEEQ is intensely localized at the interface. However, when the Al substrate temperature increases to 900 K (approaching its melting point), its shear strength significantly decreases, allowing plastic deformation to spread along the substrate boundary. This indicates that thermal softening facilitates more extensive plastic flow at higher temperatures.

Figure 4.36 shows the results of the PEEQ of the Cu/Al impact when both particle and substrate have the same temperature. It is evident that there is no significant difference between the whole-model preheating and the substrate preheating case; only the particle is more flattened (as seen in Figure 4.34) and exhibits a higher PEEQ. This indicates that increasing the initial particle temperature has a less significant effect compared to substrate preheating. In addition, it appears that the deformation behavior achieved by preheating the model is comparable to that induced by the high impact velocities [123]. The deformation behavior at 900 K is consistent with that observed experimentally for the Cu/Al impact at a temperature of 873 K (Figure 4.37).



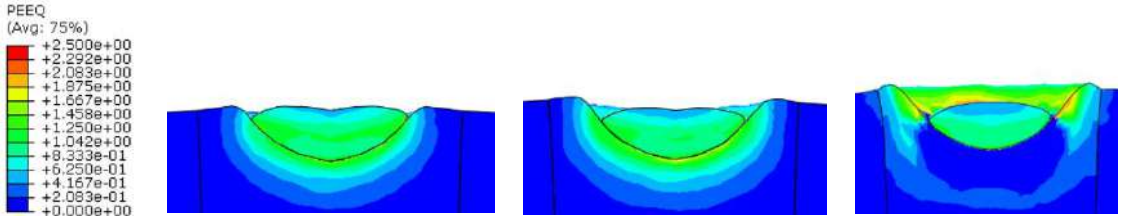
500 K **700 K** **900 K**

Figure 4. 34 PEEQ distribution for Cu/Al impact after 60ns at different particle temperatures



500 K **700 K** **900 K**

Figure 4. 35 PEEQ distribution for Cu/Al impact after 60ns at different substrate temperatures



500 K **700 K** **900 K**

Figure 4. 36 PEEQ distribution for Cu/Al impact after 60ns at different temperatures of whole-model

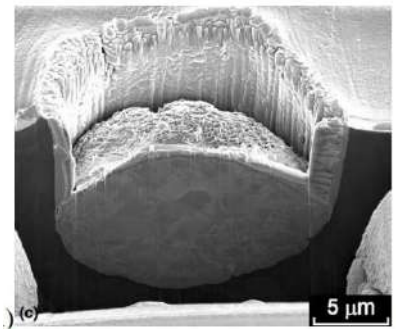
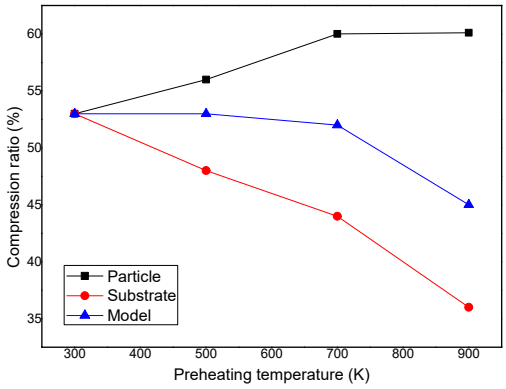


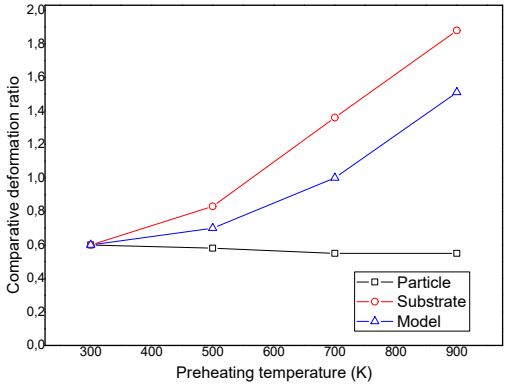
Figure 4. 37 SEM image of Cu/Al impact

The evolution of compression ratio (CR), comparative deformation ratio (CDR) and crater depth of the substrate at different heating temperatures are presented in Figure 4.38 (a-c). As indicated by the deformed final shape of the Cu particle, the CR increases with increasing particle preheating temperature. Conversely, the CR decreases when the substrate or the whole model is preheated. Because the increase of Al substrate temperature leads to thermal softening, rendering it softer and uncapable of resisting the Cu particle, resulting in a low

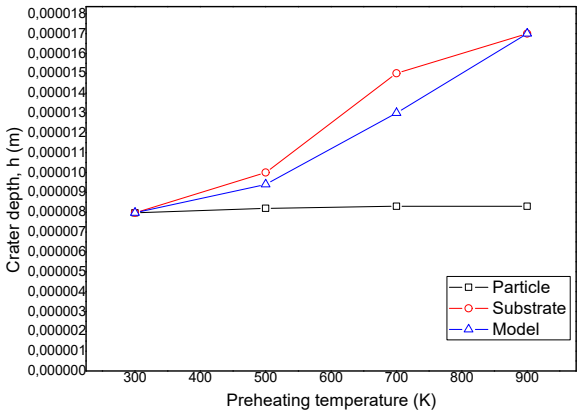
compression ratio [125]. The crater depth of the substrate increases with both substrate and whole-model preheating, while remains unchanged for the particle preheating. This explains the variation of CDR (Figure 4. 38 (c)).



(a)



(b)



(c)

Figure 4. 38 Evolution of (a) compression ratio, (b) comparative deformation ratio and (c) crater depth of the substrate at different preheating ways (particle, substrate and whole model)

In order to evaluate the effect of whole model preheating on optimizing the particle velocity in the Cu/Al impact case, the simulation was repeated at velocity of 200 m/s and temperature of 900 K. The calculation time was set to 100 ns to capture the full process. The results

clearly show that a decrease in particle velocity leads to significantly less deformation of Cu particle with less crater depth in the substrate. However, there is a significant increase in PEEQ at the contact interface. Additionally, even after 100 ns the particle does not flatten as much as it does at 500m/s after only 60ns, resulting in a reduced compression ratio.

Subsequently, the temperature was increased to 1200k (higher than the melting point of both Cu and Al materials), as shown in Figure 4.39 (c). It can be observed a notable increase in the particle flattening. The Al substrate is melted at this temperature; it acts as a fluid, therefore no plastic deformation occurs at the substrate. The crater depth is mainly due to the elastic strain. Thus, preheating at low velocities (less than the critical velocity) has a minimal effect on the bonding process.

In conclusion, in the cold spray process, increasing the preheating temperature is generally less effective compared to increasing the initial particle velocity in promoting coating/substrate strong bonding.

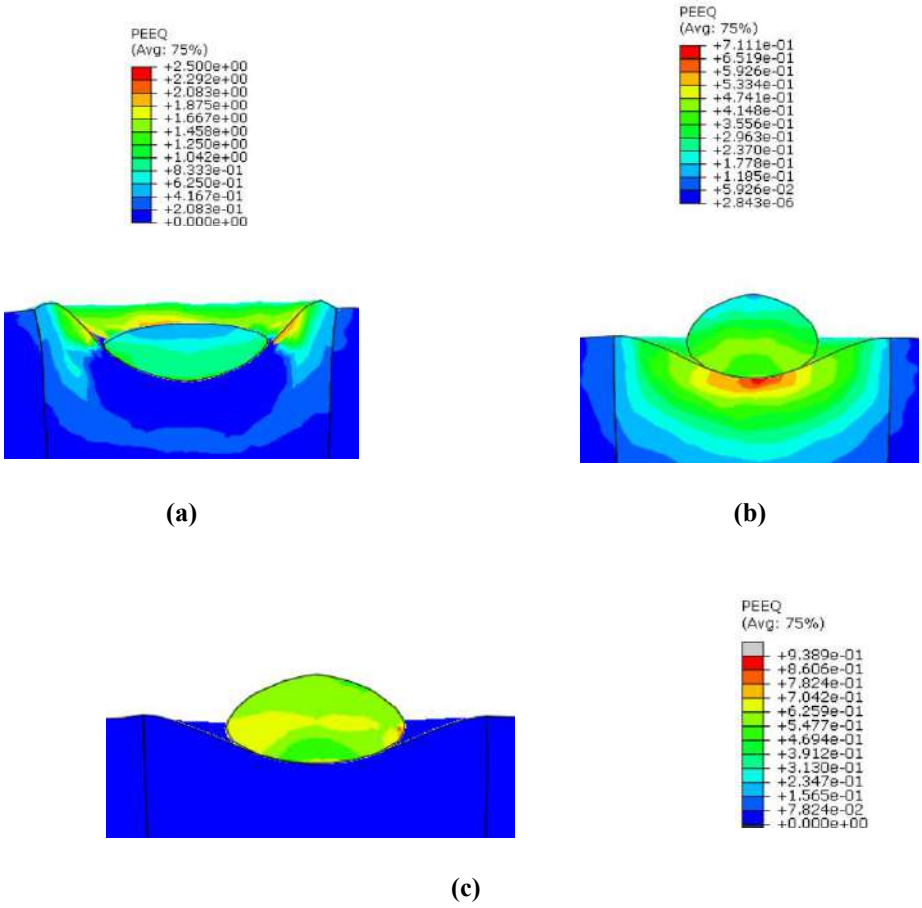


Figure 4. 39 PEEQ distribution of Cu/Al impact. (a) T= 900 K, V=500m/s and t= 60ns (b) T=900 K, V=200m/s and t=100ns (c) T=1200 K, V=200m/s and t=100ns

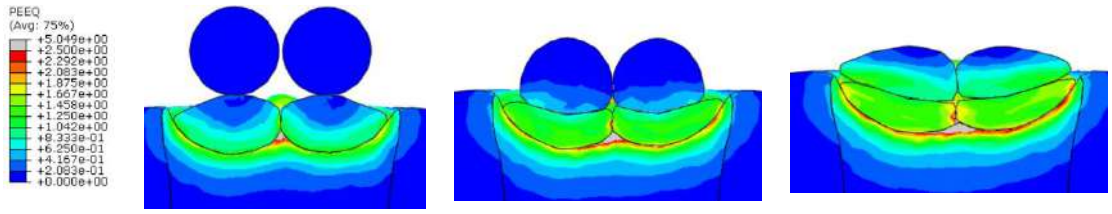
4.5.4. Mixed Al–Cu multi-particle deposition

A. Uniform velocity impact:

This section presents an analysis of multi-particle impacts involving dissimilar Cu and Al materials in order to examine whether placing a dense copper particle as the first layer that impacts the aluminum substrate can enhance bonding and coating efficiency. Research reveal that the harder Cu particle easily penetrates the softer Al substrate, improving the tamping effect and leading to strong mechanical interlocking [126,117]. Herein, we investigate the spraying process of mixed 25 μm Cu and Al particles at a temperature of 300 K and an impact velocity of 700 m/s. The selected velocity is substantially higher than the critical velocity required for Cu particles to achieve bonding with an Al substrate. According to finite element analyses reported by Chengsong Zhang et al [127], the critical velocity for (Cu/Al) system range between 510 and 530 m/s. Therefore, the chosen impact velocity is sufficient to ensure effective bonding.

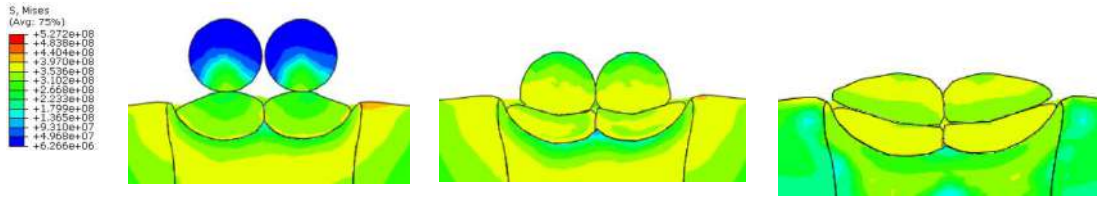
Figure 4.40 shows the mechanical and thermal response of Cu–Al particles during the impact on Al substrate. The spherical shape of the particles promotes symmetrical plastic deformation along the direction of impact. As discussed previously, the low hardness of the Al substrate allows the cu particle to penetrate deeply, forming a crater around the contact region, which exhibits pronounced penetration behavior. As the following Al particles impact, they cause the Cu particles to flatten even more. It can be observed that the highest PEEQ values are localized at the particle/substrate interface (identified as the element key). Von Mises stress was used to evaluate the onset and localization of plastic deformation (Figure 4.40 (b)). The stress in the Cu particles increases as they are squeezed between the following Al particles and the substrate, where elevated shear stresses force the material to undergo pronounced deformation (flattening). The stress extends deeper into the Al substrate, indicating that the impact energy has been distributed through the bulk material. This stress remains stored in the substrate as compressive residual stress. While residual stresses can sometimes contribute to delamination or peeling, studies have demonstrated that they are generally advantageous for coatings and can improve fatigue life [128].

Figure 4.40 (c) shows the temperature distribution, highlights the role of adiabatic heating. The increse of the temperature at the interface promotes thermal sofetning. Therefore, using Cu particles as the first impacting layer instead of Al particles not only creates mechanical interlocking, but also promotes metallurgical bonding [76,129].



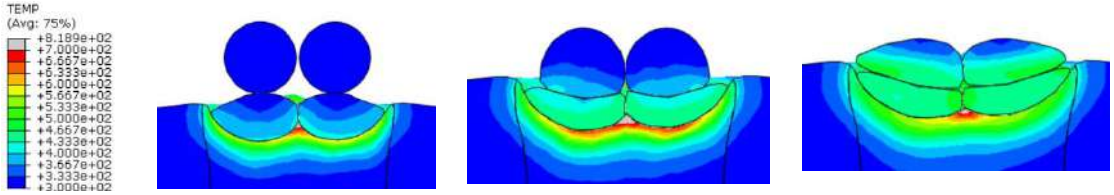
t=30ns t=50ns t=70ns

(a)



t=30ns t=50ns t=70ns

(b)



t=30ns t=50ns t=70ns

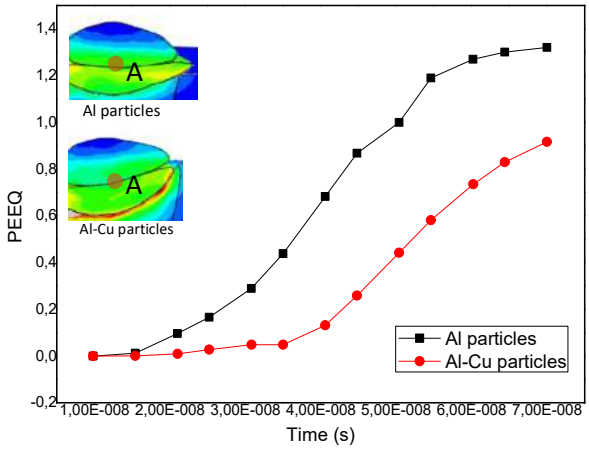
(c)

Figure 4. 40 Cu–Al particles deposition on Al substrate at 700m/s: (a) Equivalent plastic strain distribution. (b) Von Mises stress distribution. (c) Temperature distribution

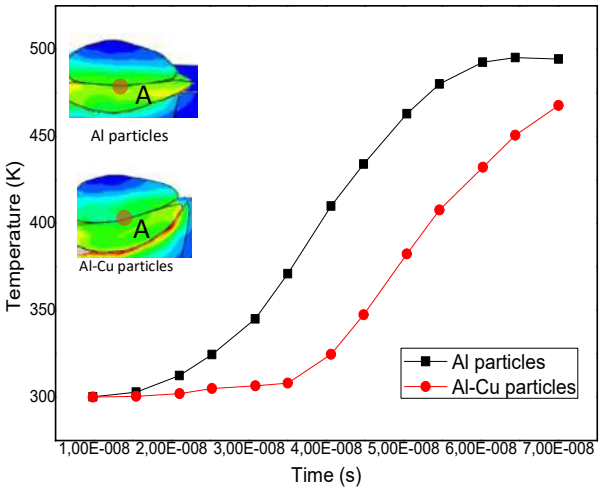
Figures 4.41(a) and (b) show the evolution of PEEQ and temperature, respectively, at the impact point of the subsequent particle (point A). Both multiple impacts of Al particles and combined Al–Cu impacts are considered. The temperature rise is associated with the magnitude of plastic deformation, providing the thermal energy required for adiabatic shear instability (ASI).

In contrast to the multi-Al impact, the Al particles caused minimal deformation of the Cu layer under identical impact conditions, due to the hardness of the Cu material, which is indicated by the lower PEEQ values recorded within the Cu regions in Figure 4.41 (a). This behavior is governed by the mechanical impedance mismatch at the interface.

Furthermore, the suppression of PEEQ in the Al-Cu case implies reduced plastic work converted into heat, thereby limiting the local adiabatic softening effect required for metallurgical bonding.



(a)



(b)

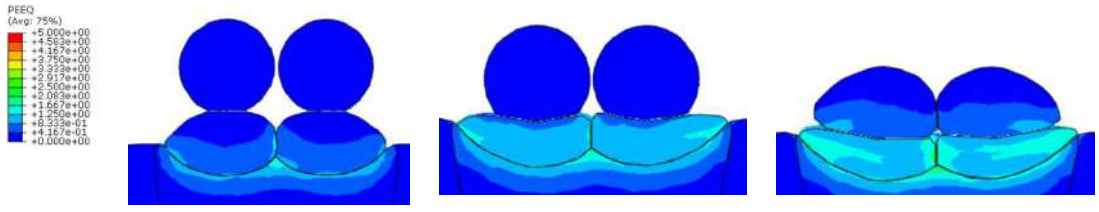
Figure 4. 41 (a) Time evolution of equivalent plastic strain (PEEQ) at point A for Al and mixed Al-Cu particle impacts. (b) Time evolution of temperature at point A for Al and mixed Al-Cu particle impacts. Point A represents the top surface of the first impacting particles, (Cu)

B. Material-specific critical velocity impact:

To more realistically capture material-dependent deposition behavior, material-specific critical velocities are applied to each particle in a mixed-metal CS simulation. According to Chengsong Zhang et al [127], the critical velocities for Al/Cu and Cu/Al cold-spray systems are in the ranges of 600–630 m/s and 510–530 m/s, respectively. To elucidate the underlying thermomechanical mechanisms governing particle deformation, the equivalent plastic strain, von Mises stress, and temperature are first investigated. As can observed from Figure 4.42 (a), the highest plastic strain is localized at the particle/substrate interface. Such behavior is also evident when the particles impact at a uniform velocity. However, the concentration is less pronounced due to the lower kinetic energy. At 70ns, it can be observed that the material flaring out at the edges, representing adiabatic shear instability (ASI), which is essential for metallurgical bonds.

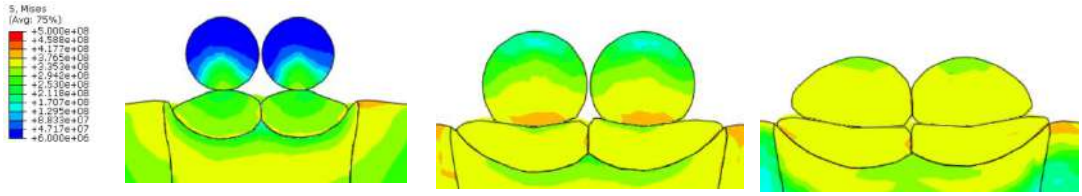
In addition, the Von-Mises stress exhibits the highest value at the interface as seen in Figure 4.42 (b). As the Cu particles undergo compression, the stress propagates throughout the particles. A sharp increase in Von Mises stress is observed in the trailing Al particles as they impact the already-deformed Cu layer, leading to rapid plastic deformation.

The intense plastic deformation of both particles and substrate generates significant local heat. The temperature rise is particularly concentrated in the contact regions (Figure 4.42 (c)). This is why cold spray is preferred for oxygen-sensitive materials; it avoids bulk melting while enabling bonding through localized heating and plastic deformation at the contact interface [130].



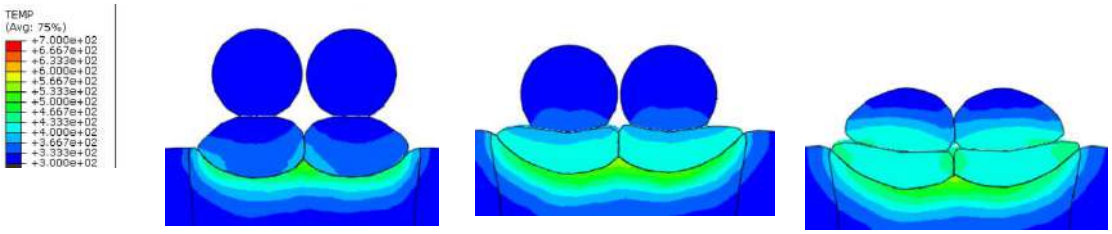
t=30ns t=50ns t=70ns

(a)



t=30ns t=50ns t=70ns

(b)



t=30ns t=50ns t=70ns

(c)

Figure 4. 42 Cu–Al particles deposition on Al substrate: (a) Equivalent plastic strain distribution. (b) Von Mises stress distribution. (c) Temperature distribution. Critical velocities of Al and Cu particles are taken 600 and 510m/s, respectively

Conclusion

This chapter summarizes the findings concerning the deformation behavior of cold-sprayed particles. The main findings are summarized below.

- The numerical model was validated with those from previous studies in literature, considering both Lagrangian and Coupled-Eulerian-Lagrangian (CEL) approaches, in two-dimensional (2D) and three-dimensional (3D) configurations. The results revealed a good agreement.
- The CEL method proves to be more effective than the Lagrangian method, as the latter exhibits severe mesh distortion after a short calculation time.
- Achieving bonding between the solid particle and the substrate requires an impact velocity higher than the material's critical velocity. However, higher velocity causes erosion of the substrate.
- The investigation of particle/substrate material combinations indicates that in Cu/Cu and Cu/Al impacts, a high compression ratio (CR) and significant crater depth of the substrate were achieved, respectively.
- The outcomes of particle preheating, substrate preheating, and whole model preheating indicate that increasing the initial particle temperature has a less pronounced effect on bonding mechanism compared to substrate preheating. Additionally, increasing the preheating temperature is generally less effective compared to increasing the initial particle velocity in CS.
- The analysis of the impact of dissimilar materials where copper particles were placed as the first impacting particles on aluminum substrate, followed by the Al particles, indicate that in contrast to the multi-Al impact case, the Cu particles penetrate deeply into the softer substrate, creating mechanical interlocking.
- Assigning material-specific critical velocities provides a more physically realistic representation of multi-material CS deposition, ensuring that each material reaches the minimum kinetic condition required for bonding.

GENERAL CONCLUSION

This doctoral thesis presents a numerical study of the phenomenon of particle impact and spreading on a solid substrate. It is primarily divided into two sections, each focusing on a specific surface treatment technique: namely, thermal spray and cold spray coating processes. This work is expected to contribute to the optimization of surface coating strategies for industrial applications.

We first simulate the normal impact of fully molten Al droplets on a steel substrate; both successive and simultaneous impacts are studied. Therefore, to begin the spacing distance and time separation between two impacting droplets were simulated. We found that in the simultaneous impact, a jet of material was produced as the two droplets interact under the effect of a significant kinetic energy, the high of this jet decreases as the droplets spread. However, it does not completely disappear, resulting in uneven splat morphology; an effect that was not observed during successive impacts, besides splashing phenomenon. To improve our understanding, we examined the effect of increasing the initial droplet velocity on the final shape of lamella, which exhibited disk-splat morphology, except for the simultaneous impact, where the jet high is more pronounced for higher impact velocities. In addition, the spreading rate was improved as the velocity increases.

Subsequently, the influence of including a solid core within the droplets in successive impact with different percentages was examined. A completely molten droplets exhibit a larger spreading compared to the semi-molten droplets. Additionally, the droplet with 75% of solid core produces the higher shear stress at the point of impact among all cases. However, the molten state of the droplet does not really affect the dynamics of the droplets (spreading velocity and pressure remain nearly unchanged), since the spreading is governed by the molten layer of the droplet. The surface oxidation effect was also investigated by the fluid-structure interaction (FSI), we noticed that the oxide layer can act as a thermal barrier between the liquid droplet and the solid substrate.

Secondly, in order to avoid the thermal issues that may occur during thermal spray due to the high droplet's temperature, we developed a numerical model of solid droplet impact and deformation under different material and process conditions, using CEL approach in the ABAQUS/EXPLICIT software. We found that achieving a strong bonding between the particle and the substrate requires an impact velocity higher than the material’s critical velocity. Additionally, each material possesses a specific critical velocity. Using aluminum as

both the droplet and substrate material is not recommended in our study. Except in the case of multiple impacts, where bonding is achieved through the subsequent droplet.

Compression ratio (CR) and comparative deformation ratio (CDR) are two of the parameters that predict the bonding mechanism. High CR and a proper CDR are needed for good adhesion.

The substrate preheating is another factor that affects the particles behavior. However, not as much as the particle velocity. Thus, the CS is a dynamic process that depends primarily on the kinetic energy.

Finally, the study examined the impact of dissimilar particles composed of Cu and Al. It was revealed that the higher kinetic energy of the Cu particles leads to deeper penetration into the substrate compared to multi-Al impacts, facilitating robust mechanical interlocking. In addition, the analysis indicated that assigning material-specific critical velocities ensures bonding with minimal kinetic energy and provides a more physically realistic representation of the deposition process.

This study offers valuable insights for the development of high-performance metal coatings by examining the high-thermal spray and the solid-state kinetic deposition of cold spray. The research allows engineers to develop coatings with superior bond strength, reducing the risk of delamination and fatigue-related failure in metallic substrates.

Perspectives

There are several promising topics merit examination in future works.

- Electromagnetic fields can be used in order to improve droplets deposition in thermal spraying process.
- Simulations of the carrier gas (in both thermal and cold spray processes) can be conducted.
- The effect of the oxide layer on both particle and substrate surfaces should be examined in further studies.
- Future research can also focus on using environmentally friendly materials.
- AI can be a good use in the field of surface treatment, by predicting the optimal parameters such as impact velocity, particle size, particle initial shape, and temperature of both droplet and substrate.

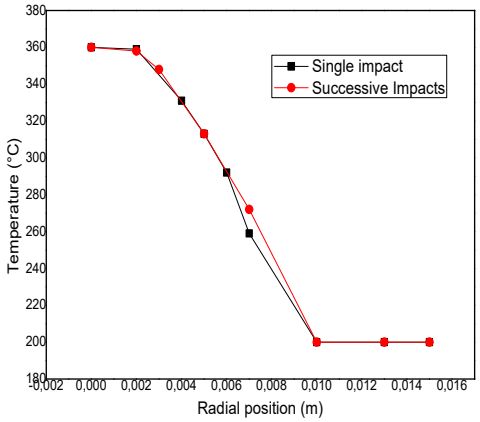
Appendix A: Radial temperature evolution of a fully molten aluminum droplet during single and successive impacts on a steel substrate under thermal spray conditions

Figure 1 (a) and (b) present the radial temperature evolution along the substrate surface for single and successive impacts, evaluated at 2 and 4 m/s (the onset of droplet solidification), to ensures that the thermal field relevant to bonding is captured. Data from simultaneous impacts was excluded because each particle behaves similarly to a single impacting droplet. Instead, the analysis focused on the temperature evolution where the two particles meet, measured on the bottom surface of the particles and the top surface of the substrate, as illustrated in Figure 1 (c).

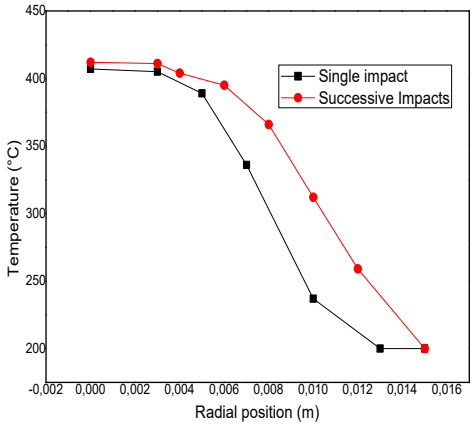
At the center (r = 0), the substrate temperature increased from an initial 200°C to over 400°C after the impact of the droplets. As the droplet flattens into a splat, it covers more of the substrate (the droplet/substrate contact area increases). It can be observed that the point where the temperature drops back to 200°C at 2 ms is at roughly r = 0.01 m. By 4 ms, this knee has moved to r = 0.013m. This perfectly represents the spreading of the liquid on the substrate surface over time.

Furthermore, for the successive impacts at 4 ms, the temperature is higher at the center (r=0), where the second particle acts as a fresh heat source and forces the substrate surface to stay hotter for longer. Due to the extra mass of the liquid in the successive impacts compaired to single impact, heat duration is prolonged.

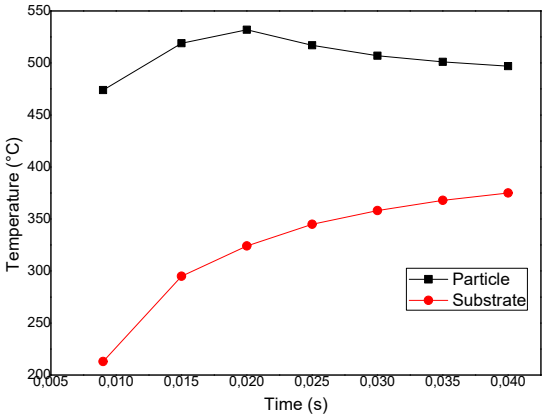
Figure 1 (c) shows the temperature evolution at the meeting point of the particles, measured on the bottom surface of the particles and the top surface of the substrate. The increase of the temperature at the droplets interface at first moments of collision is explained by the conversion of kinetic energy into viscous forces. Then it gradually declines with the cooling and solidification of the jet. For the substrate, the temperature rises steadily from 200°C toward 375°C, indicating that heat is being transferred from the hot liquid particles down into the substrate. In a simultaneous impact, unlike the outer edges of a splat which cool over time, the meeting point is surrounded by hot liquid on both sides, creating a thermal concentration zone where heat cannot dissipate sideways, only downward, which increases the substrate temperature.



(a) At 2ms



(b) At 4ms



(c)

Figure 1. The radial temperature distribution along the substrate surface. (a) At t=2ms. (b) At t=4ms. (c) Temperature evolution at the collision point between two particles during simultaneous impact, examined on both the bottom and top surfaces of the particles and the substrate.

Appendix B: Stress concentration during the impingement of droplets on the substrate

The detailed evolution of XY shear stress within the substrate, as captured in Figure 2, reveals a dynamic sequence governed by the interplay of impact dynamics, fluid flow, and phase change. The process initiates with a classic Hertzian elastic contact field during the compressible impact phase, evidenced by a highly localized, subsurface shear stress peak. As the droplet transitions to spreading, this stress field undergoes a profound transformation, radially propagating in direct concert with the expanding liquid lamella. This expansion acts as a source for a shear stress wave, driven by the horizontal momentum transfer of the flowing liquid, whose magnitude decays radially due to spreading and viscous dissipation. The final and most critical transition occurs with solidification, which fundamentally alters the stress state.

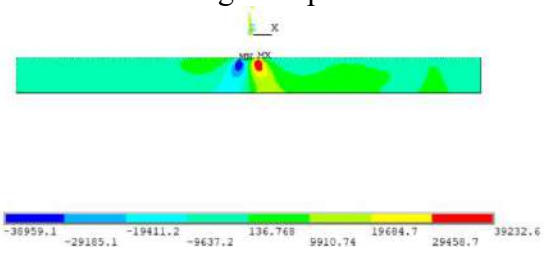
The transition from single to successive droplet impacts leads to a fundamentally different thermomechanical response, characterized by stress superposition and strong thermal coupling, which collectively forge a more complex and persistent interfacial stress state. Unlike a single impact, the stress field generated by a subsequent droplet is imposed on a substrate that has not fully relaxed and remains at an elevated local temperature due to prior deposition. This phenomenon arises from two primary, coupled mechanisms: the constructive interference of stress waves from the sequential impacts, which amplifies shear loads prior to full substrate relaxation, and the thermal softening of the substrate material due to pre-heating from the initial splat. This reduced yield strength enhances the material's compliance, facilitating a broader distribution of shear stress and greater plastic deformation. Consequently, the residual stress locked in after solidification remains markedly elevated, reflecting a cumulative plastic deformation legacy. This legacy presents a dual-edged outcome: while it promotes adhesion through enhanced mechanical interlocking and a larger bonded interface, it simultaneously elevates the mean stress level, thereby increasing the driving force for potential fatigue-driven crack propagation or interfacial delamination over the coating's service life.

The simultaneous impact scenario generates a uniquely complex and heterogeneous stress field, driven by the interplay of interfering stress waves and chaotic fluid-structure interactions. At the moment of initial contact, the substrate responds not to a single symmetric load but to two distinct, off-axis contact zones.

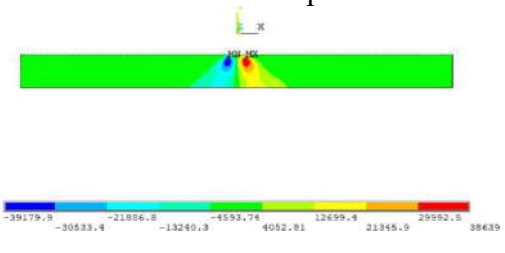
As the droplets spread, the system enters a highly dynamic phase dominated by two concurrent phenomena. First, radially expanding shear stress waves from each impact site collide. Their interaction creates zones of intense interference, where wave superposition can lead to localized peaks from constructive interference. Second, and occurring simultaneously, the violent collision of the two liquid lamellae above the substrate with associated jetting, splashing, and vortex formation imparts rapid, asymmetric shear loads. These transient fluid dynamics are directly registered on the substrate surface as sharp, localized stress fluctuations superimposed on the broader wave pattern.

A persistent line of residual shear stress concentrated at the coalescence boundary. This concentration is not a relic of the initial impact but a direct consequence of incompatible strain. As the two separate splats solidify and merge, their differential thermal contraction and the geometric constraint imposed by their meeting line create a localized, locked-in stress field. This interfacial stress concentration acts as a preferential microstructural defect, serving as a potent site for the initiation of micro-cracks or interfacial voids, thereby dictating the potential failure mechanisms within the coating.

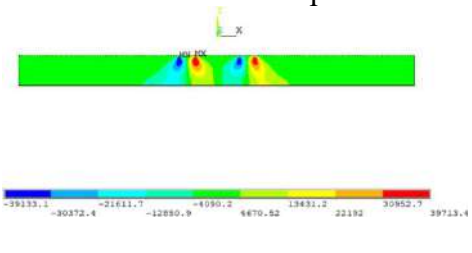
Single droplet



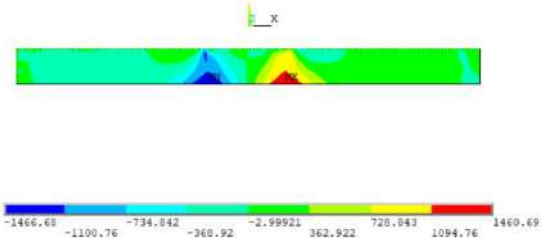
Successive droplets



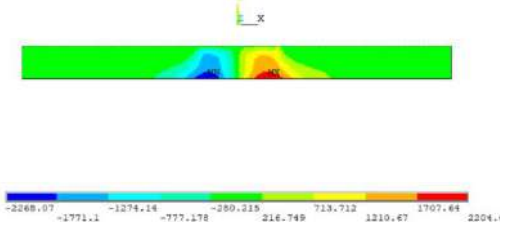
Simultaneous droplets



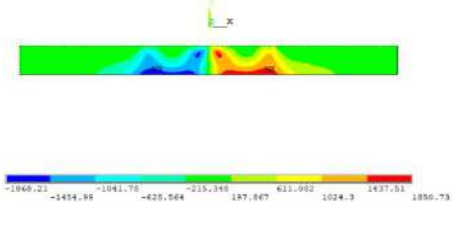
t=0.05ms



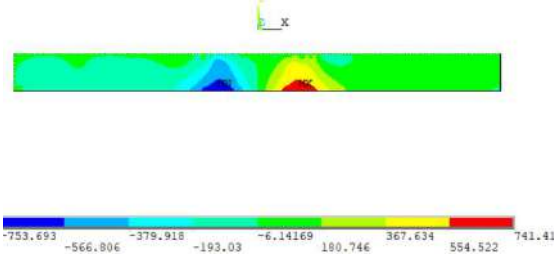
t=0.05ms



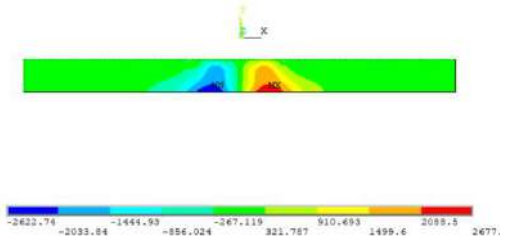
t=0.05ms



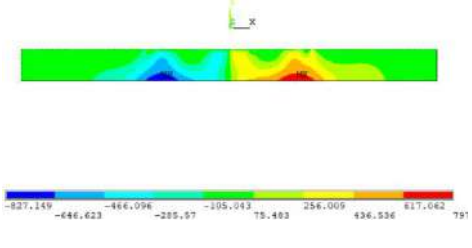
t=0.7ms



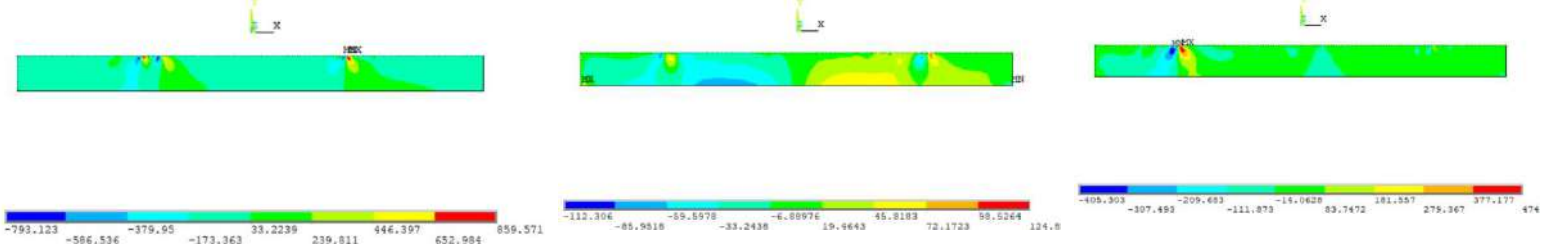
t=0.7ms



t=0.7ms



t=1ms t=1ms t=1ms



t=4ms t=4ms t=4ms

Figure 2. XY shear stress distribution over time

Appendix C: Eulerian Material Assignment (Volume Fraction tool)

The volume fraction tool generates a scalar discrete field by applying a Boolean comparison between an Eulerian part instance (particle) and an intersecting reference part instance. The comparison determines the overlapping regions between the two part instances and assigns each element of the Eulerian instance a volume fraction based on the percentage of the element that is occupied by the reference instance [131].

Figure 3 illustrates the initial assembly configuration for Coupled Eulerian-Lagrangian (CEL) analysis used in the study.

Figure 4 and the following procedure summarize the process of using the volume fraction tool:

1.Using the appropriate modeling tools in Abaqus/CAE, create a reference part that represents the geometry of the target Eulerian material domain.

2. Position an instance of the reference part within the Eulerian part instance such that it spatially matches the intended Eulerian material region.

3. Apply the volume fraction tool to generate a discrete field by comparing the reference part instance with the Eulerian part instance.

4. Assign the material to the Eulerian part instance by defining a predefined material assignment field using the discrete field obtained from the volume fraction tool.

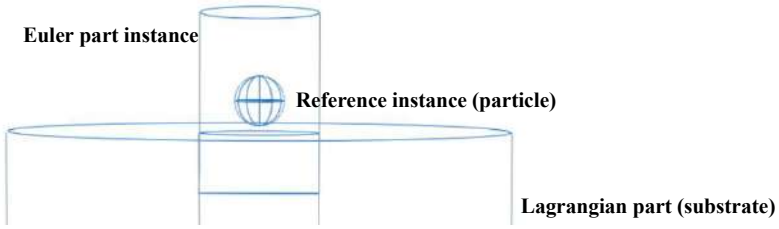


Figure 3. Schematic representation of the Eulerian-Lagrangian assembly and reference instance positioning.

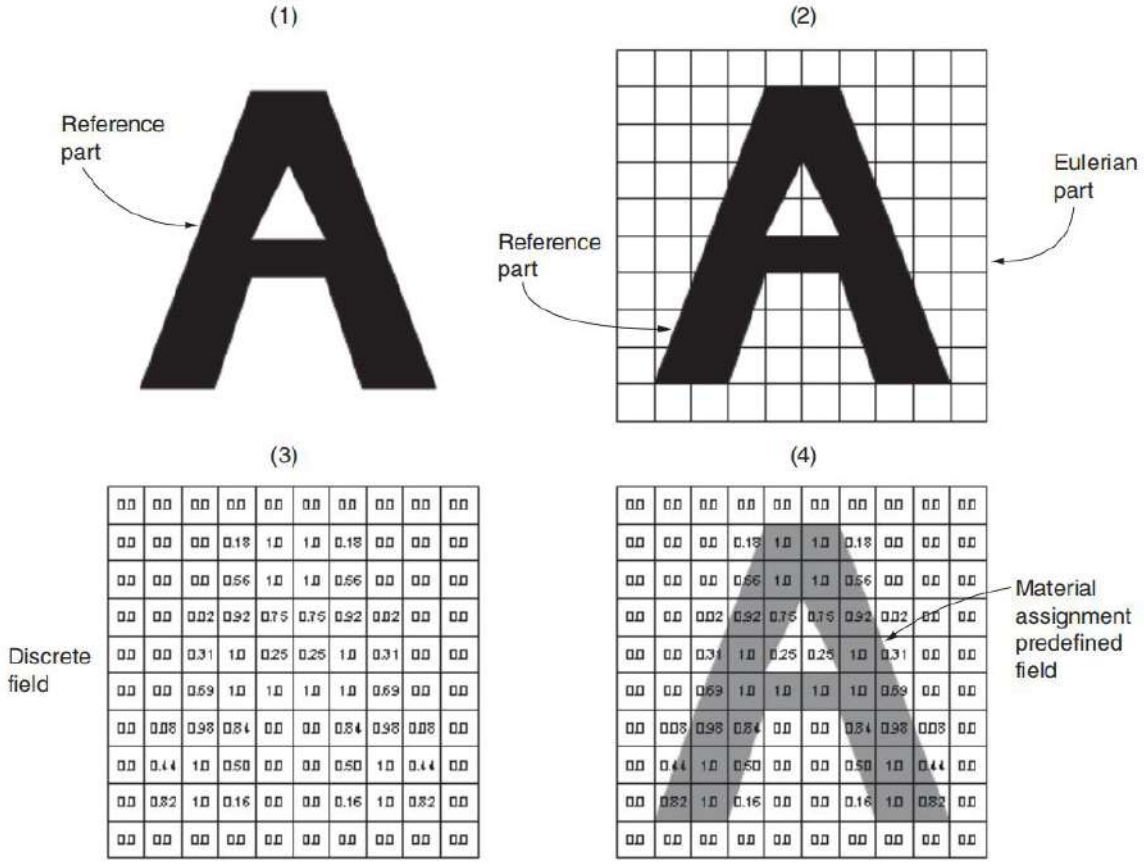


Figure 4. Procedure for using the volume fraction tool [131]

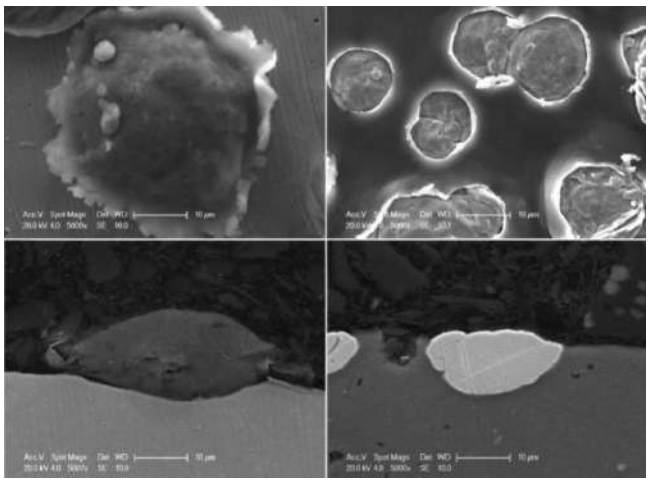
Appendix D: Multi-particle deposition of Al and mixed Al–Cu particles

Figure 5 presents the thickness of the formed coating in multi-particle deposition of Al and mixed Al–Cu particles after 70 ns. In pure Al impact, the particles and the substrate have identical mechanical properties (hardness and density). Particles stack on each other, but it does not punch deeply into the substrate. Thus, the splat exhibits a larger height, indicating a thicker splat and limited penetration. In contrast, in the Al–Cu case, the Cu particle exhibits deeper penetration into the substrate, which improves particle anchoring. This is consistent with the SEM images from the work of T. Hussain [129] (Figure 6).



(a) (b)

Figure 5. Coating thickness. (a) Impact of Al particles on Al substrate. (b) Impact of Al-Cu particles on Al substrate



(a) (b)

Figure 6. Plan-view and cross-section SE images of (a) an Al particle on a Cu substrate and (b) Cu particles on an Al substrate [129]

References

[1] Bolleddula DA. (2001). Droplet impact and spreading of viscous dispersions and volatile solutions. PhD dissertation.

[2] Hao Yi, Zhipeng Wang, Huajun Cao, Menglin Liu, and Jinxin Li. (2023). Metal Droplet Deposition: From Foundation to Engineering Manufacturing. Adv. Eng. Mater. 25, 2201003.

[3] Yang Ma, Zijian Zhou, Feiyu Zhang, Yongpan Cheng, Jinliang Xu. (2023) Numerical investigation of impacting heat transfer of binary droplets on superhydrophobic substrates. International Journal of Thermal Sciences 192 108381.

[4] Yang Xu. (2018). Normal impact of liquid droplets on smooth solid surfaces. Université Paris-Est.

[5] Kuppa Ashoke Raman, Rajeev K. Jaiman, Thong-See Lee, Hong-Tong Low. (2016). Lattice Boltzmann study on the dynamics of successive droplets impact on a solid surface. Chemical Engineering Science 145 181–195

[6] Njobuenwu D. O., Nna E. (2005). The Effect of Critical Wetting Agent Concentration on Drilling Fluids Performance, J. Sci. & Tech. Research, 4(1), p. 65-71.

[7] https://www.igvp.uni-stuttgart.de/en/research/plasmatechnology/processes/surface-wettability/

[8] Alireza Mohammad Karim. (2023). Physics of droplet impact on various substrates and its current advancements in interfacial science:: A review. J. Appl. Phys. 133, 030701. doi: 10.1063/5.0130043

[9] Daniel A. Bolleddula. (2011). Droplet impact and spreading of viscous dispersions and volatile solutions. A dissertation submitted in partial fulfillment of the requirements for the degree of Doctor of Philosophy

[10] Rioboo R, Delattre B, Duvivier D, Vaillant A, De Coninck J. (2012). Superhydrophobicity and liquid repellency of solutions on polypropylene. Adv Colloid Interface Sci 175:1–10

[11] Antonini C, Villa F, Bernagozzi I, Amirfazli A, Marengo M .(2013). Drop rebound after impact: the role of receding contact angle. Langmuir 29:16045–16050

[12] Carlo Antonini, Alidad Amirfazli, and Marco Marengo. (2012). Drop impact and wettability: From hydrophilic to superhydrophobic surfaces. Physics of Fluids 24, 102104. http://dx.doi.org/10.1063/1.4757122

[13] Fauchais P. (2004). Understanding plasma spraying J. Phys. D: Appl. Phys., Vol. 37, n° 9, pp. 86-108

[14] Jones H. (1971). Cooling, freezing and substrate impact of droplets formed by rotary atomization, J. Phys. D: Appl. Phys., Vol. 4, pp. 1657-1660

[15] Yamina MEBDOUA. (2008). Numerical Study of Thermal Phenomena Controlling the Solidification of a Lamella in Thermal Spraying: Application to Deposit Formation. Thesis to obtain the degree of Doctor. UNIVERSITY OF LIMOGES

[16] B. Scheller and D. Bousfield. (1995). Newtonian droplet with a solid surface. AIChE J. 41, 1357–1367

[17] Madejski, J. (1976). Solidification of droplets on a cold surface. International Journal of Heat and Mass Transfer, 19(9), pp.1009-1013.

[18] Roisman, I.V., Rioboo, R. and Tropea, C. (2002). Normal impact of a liquid drop on a drysurface: model for spreading and receding. Proceedings of the Royal Society of London: Mathematical, Physical and Engineering Sciences, 458, pp.1411-1430.

[19] Pasandideh-Fard, M., Qiao, Y.M., Chandra, S. and Mostaghimi, J. (1996). Capillary effects during droplet impact on a solid surface. Physics of Fluids, 8(3), pp.650-659.

[20] yonemoto, Y., Tashiro, K., Shimizu, K. (2022). Predicting the splash of a droplet impinging on solid substrates. *Sci Rep* **12**, 5093 https://doi.org/10.1038/s41598-022-08852-3

[21] C. Mundo, M. Sommerfeld, C. Tropea. (1995). Droplet-wall collisions: Experimental studies of the deformation and breakup process. Int. J. Multiphase Flow Volume 21, Issue 2, April, Pages 151-173 https://doi.org/10.1016/0301-9322(94)00069-V

[22] Masahiro Fukumoto, Eiji Nishioka, Takeshi Nishiyama. (2002). New criterion for splashing in flattening of thermal sprayed particles onto flat substrate surface. Surface and Coatings Technology 161 103–110.

[23] Xu, L., Zhang, W. W., and Nagel, S. R. (2005). Drop splashing on a dry smoot surface. Phys. Rev. Lett. 94, 184505

[24] Jie Liu, Henry Vu, Sam S. Yoon, Richard Jepsen & Guillermo Aguilar. (2010). SPLASHING PHENOMENA DURING LIQUID DROPLET IMPACT. Atomization and Sprays 20(4), 297–310

[25] M.Y. Zhang, H. Zhang, L.L. Zheng. (2008). Simulation of droplet spreading, splashing and solidification using smoothed particle hydrodynamics method. Int. J. Heat Mass Transf. Volume 51

[26] H. R. Chiu, H. K. Ma. (2009). Solidification Models of an Impinging Metal Droplet. Particul. Sci. Technol. Volume 27. https://doi.org/10.1080/02726350802611788

[27] Zhang, H., Zhang, X., Yi, X. et al. (2021). Reversed role of liquid viscosity on drop splash. Phys. Fluids 33, 052103

[28] T. Ma, D. Chen, H. Sun, D. Ma, A. Xu, P. Wang, Eur. (2021) Dynamic behavior of metal droplet impact on dry smooth wall: SPH simulation and splash criteria. J. Mech. B Fluids volumr 88, 123-134

[29] Arda Cetinera, Burak Evrenb, Mete Budaklia, Mehmet Arikc, Arif Ozbek. (2020). Spreading behavior of droplets impacting over substrates with varying surface topographies. Colloids and Surfaces A 606 125385

[30] Danish, M. (2022). Contact Angle Studies of Hydrophobic and Hydrophilic Surfaces. In: Thomas, S., Rezazadeh Nochehdehi, A. (eds) Handbook of Magnetic Hybrid Nanoalloys and their Nanocomposites. Springer, Cham. https://doi.org/10.1007/978-3-030-90948-2_24

[31] T. Mao, D.C.S. Kuhn, H. Tran. (1997). Spread and rebound of liquid droplets upon impact on flat surfaces. AIChE J. 43 (9) 2169–2179.

[32] C. Antonini • F. Villa • M. Marengo. (2014). Oblique impacts of water drops onto hydrophobic and superhydrophobic surfaces: outcomes, timing, and rebound maps. Springer-Verlag Berlin Heidelberg. DOI 10.1007/s00348-014-1713-9.

[33] Xue, M.; Heichal, Y.; Chandra, S.; Mostaghimi, J. (2007). Modeling the impact of a mol-ten metal droplet on a solid surface using variable interfacial thermal contact resistance. J. Mater. Sci. 42, 9–18.

[34] Rahul Ramachandran and Michael Nosonovsky. (2016). Vibrations and Spatial Patterns Change Effective Wetting Properties of Superhydrophobic and Regular Membranes. DOI: 10.3390/biomimetics1010004

[35] S. Shakeri, S. Chandra. (2002). Splashing of molten tin droplets on a rough steel surface. Int. J. Heat Mass Transf. 45 4561–4575.

[36] C. Tang, et al. (2017). Dynamics of droplet impact on solid surface with different roughness. Int. J. Multiph. Flow 96 56–69

[37] Tahar, S.; Zirari, M.;Labbadlia, O.; Chiba, Y. (2022). The Influence of the Fusion State of the Particles during the Simultaneous Impact on an Oxidized Substrate in the Presence of Asperities. Processes 10, 1458. https://doi.org/10.3390/pr10081458

[38] Tahar Souad, Zirari Mounir, Benzerdjeb Abdelwahab, Hanini Salah. (2018). Numerical simulation EF/VOF to study the influence of the surface condition of the formation of the slats of a

nickel deposit produced by plasma spraying. Annales de Chimie - Science des Matériaux– n° 2/2018, 165-180

[39] G.K. Creffield, M.A. Cole, and G.R. White. (1995). The Effect of Gas Parameters on HVOF Coatings Advances in Thermal Spray Science and Technology. C.C. Berndt and S. Sampath, Ed., ASM International, p 291-301

[40] A. Abedini, A. Pourmousa, S. Chandra, J. Mostaghim. (2006). Effect of substrate temperature on the properties of coatings and splats deposited by wire arc spraying. Surface & Coatings Technology 201 3350–3358

[41] Fukumoto M., Shiiba M. and Yasui T. (2004) .Effect of substrate surface change by heating on transition in flattening behavior of thermal sprayed particles. International Thermal Spray Conference and Exposition, Osaka, Japan.

[42] Cedelle J., Vardelle M., Fauchais P. (2006). Influence of stainless steel substrate preheating on surface topography and on millimeter- and micrometer-sized splat formation. Surface & Coatings Technology, Vol. 201, pp. 1373–1382.

[43] Mingguang Shena, Ben Q. Li b, Yu Bai. (2020). Numerical modeling of YSZ droplet impact/spreading with solidification microstructure formation in plasma spraying. International Journal of Heat and Mass Transfer 150 119267

[44] Pasandideh-Fard, M., Pershin, V., Chandra, S., and Mostaghimi. (2002). Splat shapes in a thermal spray coating process: Simulations and experiments. Journal of Thermal Spray Technology, 11(2), pp.206-217

[45] Cédric Le Bot, Stéphane Vincent, Eric Arquis. (2005). Impact and solidification of indium droplets on a cold substrate. International Journal of Thermal Sciences 44 219–233

[46] M.V. Gielen, R.d. Ruiter, R.B.J. Koldeweij, D. Lohse, J.H. Snoeijer, H. Gelderblom. (2019). Solidification of liquid metal drops during impact, J. Fluid Mech. 883 A32

[47] S.D. Aziz, S. Chandra. (2000). Impact, recoil and splashing of molten metal droplets. Int. J. Heat Mass Transf. 43 (16) 2841–2857.

[48] Tao An, Hao Chen, Yuchen Wang, Haisheng Fang. (2024). Effect of substrate temperature on the deformation of liquid metal droplets during spreading and solidification. International Journal of Heat and Mass Transfer 223 125241

[49] Ghafouri-Azar, R; Mostaghimi, J; Chandra, S; Charmchi. (2003). NUMERICAL SIMULATION OF COATING DEPOSITION IN A THERMAL SPRAY PROCESS. M. Journal of Thermal Spray Technology; New York Vol. 12, N° 1

[50] Amitesh Kumar. (2014). SOLIDIFICATION OF IMPINGING MOLTEN METAL DROPLET ON A COLD SUBSTRATE. Int. J. Mech. Eng. & Rob. Res.

[51] Askeland D. R. (1990). The Science and Engineering of Materials, second edition, Chapman and Hall.

[52] Bazilevs, Yuri. (2013). Computational fluid-structure interaction : methods and applications. ISBN 978-0-470-97877

[53] Honegger, E. (1927). Test on Erosion caused by Jets. Brown Boveri Review, Vol. 14, pp. 95-104

[54] Mounir Zirari. (2010). Modeling the construction of a deposit by thermal spraying: From the formation of a lamella to the stacking of layers. Doctoral thesis.

[55] Onnu Ubbink. (1997). Numerical Prediction of two fluid systems with Sharp Interfaces". Department of Mechanical Engineering, Imperial College of Science, Technology and Medicine.

[56] C. W. Hirt and B. D. Nichols. (1981) Volume of Fluid (VOF) Method for the Dynamics of Free Boundaries. Journal of Computational Physics 39, pp. 201-225.

[57] Mahmut Aydogdu. (2023) Analysis of the effect of rigid vegetation patches on the hydraulics of an open channel flow with Realizable k-ε and Reynolds stress turbulence models. Flow Measurement and Instrumentation. Volume 94, 102477

[58] Christian Mulbah, Can Kang, Ning Mao, Wei Zhang, Ali Raza Shaikh, Shuang Teng. (2022). A review of VOF methods for simulating bubble dynamics. Progress in Nuclear Energy 154 104478.

[59] M. Rieber and A. Frohn. NAVIER STOKES SIMULATION OF DROPLET COLLISION DYNAMICS. Institut f ur Thermodynamik der Luft- und Raumfahrt, Pfaenwaldring 31, 70550 Stuttgart, Germany

[60] Meng Huang, Lilong Wu, Bin Chen. (2012). A Piecewise Linear Interface-Capturing Volume-of-Fluid Method Based on Unstructured Grids. An International Journal of Computation and Methodology Volume 61.

[61] F. J. Hong and H.-H. Qiu. (2005). MODELING OF SUBSTRATE REMELTING, FLOW, AND RESOLIDIFICATION IN MICROCASTING. Numerical Heat Transfer, Part A, 48: 987–1008.

[62] M. Pasandideh-Fard, S. Chandra, J. Mostaghimi. (2002). A three-dimensional model of droplet impact and solidification. International Journal of Heat and Mass Transfer 45 2229–2242.

[63] S. N. Marzbali. (2013).Fluid-Solid Interaction Modeling of Compressible Droplet Impact onto Elastic Substrates. American Institute of Aeronautics and Astronautics.

[64] Vít Dolejši: Discontinuous Galerkin Method (Analysis and Applications to Compressible Flow). Springer Series in Computational Mathematics. Volume 48

[65] G. P. Nikishkov. (2004). INTRODUCTION TO THE FINITE ELEMENT METHOD. University of Aizu, Aizu-Wakamatsu 965-8580, Japan

[66] Hazrat Ali and Md. Shafiqul Islam. (2017). GENERALIZED GALERKIN FINITE ELEMENT FORMULATION FOR THE NUMERICAL SOLUTIONS OF SECOND ORDER NONLINEAR BOUNDARY VALUE PROBLEMS. GANIT J. Bangladesh Math. Soc. (ISSN 1606-3694) 37 147-159

[67] Luke, P. (2021). Variational Calculus: Deriving the Strong and Weak Form. Computational Mechanics.

[68] Amel Hadjeri, Mounir Zirari, Souad Tahar, Redha Rebhi, Mohamed Kezrane, Moustafa Boukraa. (2024). Influence of the Fusion State of Particles During Slat Formation on an Oxidized Substrate. Nanotechnology Perceptions 20 No.6 1768-1785

[69] Weibo Ren, Yueqiao Hu, Bernhard Weigand. (2022) Splashing During Simultaneous Two Drops Impact Onto A Micropillared Superhydrophilic Surface. ILASS– Europe 2022, 6-8 Sep.

[70] H. Tabbara and S. Gu. (2012). Modelling of impingement phenomena for molten metallic droplets with low to high velocities. International Journal of Heat and Mass Transfer 55 2081–2086

[71] SuLi Li, ZhengYing Wei, Jun Du, Pei Wei, ZuoXian Hou, BingHeng Lu. (2015). The fusion process of successive droplets impinging onto a substrate surface. Applied Physics A . DOI:10.1007/s00339-015-9146-8

[72] Ning-Ning, HanBao-Min, SunXin He. (2022). Oblique impacts of water nanodroplets on superhydrophobic surfaces: A molecular dynamics study. Journal of Molecular Liquids 365 120074. https://doi.org/10.1016/j.molliq.2022.120074

[73] S. Alavi, M. Passandideh-Fard, J. Mostaghimi. (2012). Simulation of Semi-Molten Particle Impacts Including Heat Transfer and Phase Change. Journal of Thermal Spray Technology. 1278—Volume 21(6). DOI: 10.1007/s11666-012-9804-8

[74] A.A. Syed, A. Denoirjean, B. Hannoyer, P. Fauchais, P. Denoirjean, A.A. Khan, J.C. Labbe. (2005). Influence of substrate surface conditions on the plasma sprayed ceramic and metallic particles flattening. Surface & Coatings Technology 200 2317 – 2331

[75] Junghyun Park, Donghyun Kim, Hyunsik Kim ,Junghoon Lee ,and Wonsub Chung. (2021). Thermal Radiative Copper Oxide Layer for Enhancing Heat Dissipation of Metal Surface. Nanomaterials 11(11):2819. DOI: 10.3390/nano11112819

[76] Vaz, R.F.; Garfias, A.; Albaladejo, V.; Sanchez, J.; Cano, I.G.(2023). A Review of Advances in Cold Spray Additive Manufacturing. Coatings, 13, 267. https://doi.org/10.3390/coatings13020267

[77] Jing Xie. (2014). Simulation of cold spray particle deposition process. Mechanics of materials [physics.class-ph]. INSA de Lyon. English. NNT : 2014ISAL0044.

[78] A. P. Alkimov, V. F. Kosarev and A. N. Papyrin.(1990). Dokl. Akad. Nauk. SSSR, 315, 1062–1065.

[79] A. Papyrin, Sergey Klinkov, Vasily Fomin, Vladimir Kosarev, Anatolii Alkimov. (2007). Cold Spray Technology. Elsevier Science. 978-0-08-045155-8. DOI: https://doi.org/10.1016/B978-0-08-045155-8.X5000-5.

[80] Raoelison, R.N.; Aubignat, E.; Planche, M.P.; Costil, S.; Langlade, C.; Liao, H. (2016). Low-pressure cold spraying under 6bar pressure deposition: Exploration of high deposition efficiency solutions using amathematical modelling. Surf. Coat. Technol. 302, 47–55.

[81] Huang, Y.; Li, H.; Liu, J.; Wu, Z.; Wang, Q.; Ramachandran, C.S. (2025). Research Progress on Post-Treatment Technologies of Cold Spray Coatings. Coatings, 15, 265. https://doi.org/10.3390/coatings15030265

[82] O.C. Ozdemir, C.A. Widener, M.J. Carter, K.W. Johnson. (2017). Predicting the efects of powder feeding rates on particle impact conditions and cold spray deposited coatings. J. Term. Spray Technol. 26(7), 1598 (2017)

[83] J. Karthikeyan. (2007). The advantages and disadvantages of the cold spray coating process. ASB Industries Inc., USA

[84] Assadi, H.; Schmidt, T.; Richter, H.; Kliemann, J.O.; Binder, K.; Gärtner, F.; Klassen, T.; Kreye, H. (2011). On Parameter Selection in Cold Spraying. J. Therm. Spray Technol. 20, 1161–1176.

[85] V.K. Champagne. (2007). The cold spray materials deposition process: fundamentals and applications. (CRC Press, Boca Raton, 2007)

[86] E. Irissou, J.G. Legoux, A.N. Ryabinin, B. Jodoin, C. Moreau. (2008). Review on cold spray process and technology: Part I—intellectual property. J.Term. Spray Technol. 17(4), 495

[87] Xiawei Yang, Tingxi Meng , Yu Su, Xiaoxia Chai, Zhenguo Guo, Tiejun Ma, Shuo Yin, Wenya Li. (2024). Particle deformation and coating deposition behavior in cold spray additive manufactured aluminum deposit on copper substrate by simulation and experiment. Journal of Materials Research and Technology 30 2879–2890

[88] Qi, J.; Raoelison, R.N.;Verdy, C.; Li, J.; Rachik, M. (2023). Comparative Microstructural Study of Cold Sprayed Coatings Using Pure Aluminum and Aluminum Alloy Powders. Eng. Proc. 43, 7. https://doi.org/10.3390/ engproc2023043007

[89] Shuo Yin, Yingchau Xie, Xinkun suo, Hanlin liao, Xiaofang wang. (2014). Interfacial bonding features of Ni coating on Al substrate with different surface pretreatments in cold spray. Materials Letters 138 143–147 http://dx.doi.org/10.1016/j.matlet.2014.10.016

[90] Shuo Yin, Wenya Li, Bo Song, Xingchen Yan, Min Kuang, Yaxin Xu, Kui Wen, Rocco Lupoi. (2019). Deposition of FeCoNiCrMn high entropy alloy (HEA) coating via coldspraying. Journal of Materials Science & Technology 35 1003–1007. https://doi.org/10.1016/j.jmst.2018.12.015

[91] Alessia Bruera, Pietro Puddu, Stephan Theimer, Maria Villa-Vidaller, Alexander List, Giovanni Bolelli, Frank Gärtner, Thomas Klassen, Luca Lusvarghi. (2023). Adhesion of cold sprayed soft coatings: Effect of substrate roughness and hardness. Surface & Coatings Technology 466 129651. https://doi.org/10.1016/j.surfcoat.2023.129651

[92] CHAVAN N. M., RAMAKRISHNA M., PHANI P. S., RAO D. S., SUN DARARAJAN G. (2011). The influence of process parameters and heat treatment on the properties of cold sprayed silver coatings. Surface and Coatings Technology, vol. 205, no 20, p. 4798–4807

[93] OKA Y., OKAMURA K., YOSHIDA T. (2005). Practical estimation of erosion damage caused by solid particle impact: Part 1: Effects of impact parameters on a predictive equation. Wear, vol. 259, no 1–6, p. 95–101.

[94] A. Fardan, C.C. Berndt, R. Ahmed. (2021). Numerical modelling of particle impact and residual stresses in cold sprayed coatings: a review. Surf. Coat. Technol. 409, 126835

[95] S. Yin, Hanlin Liao, F Wang. (2013). Euler based finite element analysis on high velocity impact behaviour in cold spraying. Surface Engineering. DOI: 10.1179/1743294413Y.0000000240

[96] J.T. Carroll and J.S. Strenkowski. (1988). Finite-Element Models of Orthogonal Cutting with Application to Single Point Diamond Turning, Int. J. Mech. Sci., 12(30), p 899-920

[97] Moses A. Adaan-Nyiak, Ahmed A. Tiamiyu. (2023). Recent advances on bonding mechanism in cold spray process: A review of single-particle impact methods. Journal of Materials Research Volume 38 Issue 1 DOI:10.1557/s43578-022-00764-2

[98] X. Song, K. Lin, J.M. Chea, W. Sun, A.W. Tan, W. Zhai, F. Li, I. Marinescu, E. Liu. (2020). Coupled Eulerian-Lagrangian (CEL) simulation of multiple particle impact during Metal Cold Spray process for coating porosity prediction. Surf. Coat. Technol. 385, 125433

[99] Zhongyi Liu. (2022). Mechanism study on spreading dynamics of nanofluids droplet coupled with thermal evaporation. International Journal of Heat and Mass Transfer 183 122172

[100] Wesley Kean Wah Tai. (2022). Comparing Relative Bond Characteristics Between Spherical and Elongated Morphologies for Cold Spray Process Using SPH Simulation. J Therm Spray Tech https://doi.org/10.1007/s11666-022-01448-3

[101] G.R. Liu, M.B. Liu. (2003). Smoothed Particle Hydrodynamics. World Scientific, https://doi.org/10.1142/5340

[102] A.A. Hemeda, C. Zhang, X.Y. Hu, D. Fukuda, D. Cote, I.M. Nault, A. Nardi, V.K. Champagne, Y. Ma, J.W. Palko. (2021). Particle-based simulation of cold spray: Influence of oxide layer on impact process. Additive Manufacturing Volume 37, 101517 https://doi.org/10.1016/j.addma.2020.101517

[103] Abaqus Analysis User's Manual, ABAQUS 6.8 HTML Documentation, Dassault Systemes, 2008

[104] Nima Pourakbar Zehtab, Amir Ardeshiri Lordejani, M. Guagliano, Sara Bagherifard. (2022). Numerical Simulation of Cold Spray Bonding for CrFeNi Medium-Entropy Alloy. Adv. Eng. Mater. 24, 2200603. DOI:10.1002/adem.202200603

[105] Li, W. Y. (2009). 3-D FEM analysis of impacting behavior of cold sprayed particles. China Surface Engineering, Vol. 22, pp. 31–37

[106] T. Schmidt, F. Gärtner, H. Assadi, H. Kreye. (2006). Development of a generalized parameter window for cold spray deposition. Acta Mater. 54, 729. https://doi.org/10.1016/j.actamat.2005.10.005

[107] A. Manap, T. Okabe, K. Ogawa, S. Mahalingam, H. Abdullah. (2019). Experimental and smoothed particle hydrodynamics analysis of interfacial bonding between aluminum powder particles and aluminum substrate by cold spray technique. Int. J. Adv. Manuf. Technol. 103, 4519.

[108] Hu W. J. (2020). Effects of metal particles on cold spray deposition onto Ti-6Al-4V alloy via Abaqus/Explicit. Journal of Engineering Sciences, Vol. 7(2), pp. E19–E25, doi: 10.21272/jes.2020.7(2).

[109] Liu, Z.; Liu, J.; Li, H.; Wu, Z.; Zhong, Y.; Ramachandran, C.S.; Cheng, Y.; Wang, Q. (2024). Research Progress on Numerical Simulation of the Deposition and Deformation Behavior of Cold Spray Particles. Coatings , 14, 913. https://doi.org/10.3390/coatings14070913

[110] MANAP A., OGAWA K., OKABE T. (2011). Numerical Analysis of Interfacial Bonding of Aluminum Powder Particle and Aluminum Substrate by Cold Spray Technique using the SPH Method. Proceedings of the JSME/ASME 2011 ICMP2011, Corvallis,Oregon,USA

[111] Wen-Ya Li, Hanlin Liao, Chang-Jiu Li, Hee-Seon Bang, C. Coddet. (2007). Numerical simulation of deformation behavior of Al particles impacting on Al substrate and effect of surface oxide films on interfacial bonding in cold spraying Applied Surface Science 253 5084–5091.

[112] N.K. Gupta, M.A. Iqbal, G.S. Sekhon. (2006). Experimental and numerical studies on the behavior of thin aluminum plates subjected to impact by blunt- and hemispherical-nosed projectiles. Int. J. Impact Eng. 32 1921–1944. https://doi.org/10.1016/j.ijimpeng.2005.06.007

[113] G.R. Johnson, W.H. Cook. Fracture characteristics of three metals subjected to various strains, strain rates, temperatures and pressures. (1985). Eng. Fract. Mech. 21 31–48.

[114] King PC, Zahiri SH, Jahedi M. (2008). Focused ion beam micro-dissection of cold-sprayed particles. Acta Mater; 56(19):5617–26.

[115] M. Yu, W.-Y. Li, F. F. Wang & H. L. Liao. (2011). Finite Element Simulation of Impacting Behavior of Particles in Cold Spraying by Eulerian Approach. Journal of Thermal Spray Technology. DOI: 10.1007/s11666-011-9717-y

[116] M. Grujicic, C.L. Zhao, W.S. DeRosset, D. Helfritch. (2004). Adiabatic shear instability based mechanism for particles/ substrate bonding in the cold-gas dynamic-spray process. Mater. Des. 25 681–688

[117] Sunday Temitope Oyinbo and Tien-Chien Jen. (2020). Feasibility of numerical simulation methods on the Cold Gas Dynamic Spray (CGDS) Deposition process for ductile materials. Manufacturing Rev. 7, 24 https://doi.org/10.1051/mfreview/2020023

[118] C.D. Reddy, Z.-Q. Zhang, S. Msolli, J. Guo, N. Sridhar. (2021). Impact induced metallurgical and mechanical interlocking in metals. Comput. Mater. Sci. J. 192, 110363

[119] Xiang-lin Zhou, Xiang-kun Wu, Hui-hua Guo, Jian-guo Wang & Ji-shan Zhang. (2010). Deposition behavior of multi-particle impact in cold spraying process. International Journal of Minerals, Metallurgy and Materials Volume 17, Page 635 DOI: 10.1007/s12613-010-0367-8

[120] Saeed Rahmati. (2021). A Numerical Approach to Study the Oxide Layer Effect on Adhesion in Cold Spray. J Therm Spray Tech https://doi.org/10.1007/s11666-021-01245-4

[121] Yin, S.; Wang, X.; Suo, X.; Liao, H.; Guo, Z.; Li, W.; Coddet, C. (2013). Deposition behavior of thermally softened copper particles in cold spraying. Acta Mater. 61, 5105–5118

[122] J.O. Klieman, H. Gutzmann, F. Gartner, H. Hubner, C. Brochers, T. Klassen. (2011). Formation of Cold-Sprayed Ceramic Titanium Dioxide Layers on Metal Surfaces. J. Therm. Spray Technol. 20 292.

[123] M. Yu, , W.-Y. Li, F.F. Wang, X.K. Suo, H.L. Liao. (2013). Effect of particle and substrate preheating on particle deformation behavior in cold spraying. Surface & Coatings Technology 220 174–178

[124] Yingchun Xie. (2016). Study of particle/substrate deformation in the bonding mechanism in cold spraying. Materials. University of Technology of Belfort-Montbeliard. French. NNT 2016BELF0301

[125] Sun, W., Tan, A. W. Y., Bhowmik, A., Marinescu, I., Song, X., Zhai, W.,Liu, E. (2018). Deposition characteristics of cold sprayed Inconel 718 particles on Inconel 718 substrates with different surface conditions. Materials Science and Engineering A, 720 75-84. doi: 10.1016/j.msea.2018.02.059

[126] Gyuyeol Bae, Yuming Xiong, Santhu Kumar, Changhee Lee. (2008). General aspects of interface bonding in kinetic sprayed coatings. Acta Mater. 56(17):4858-4868. DOI: 10.1016/j.actamat.2008.06.003

[127] Chengsong Zhang, Haoting Zhan, Xiaolong Zhou, Ninshu Ma. (2024). An Improved Model for Prediction of Critical Velocity of Cold-Spray by First-Principles Calculations. Coatings, 14, 1226. https://doi.org/10.3390/coatings14091226

[128] Felipe Torres and Ruben Fernandez. (2024). Effect of Thickness on the Residual Stress Profile of an Aluminum Cold Spray Coating by Finite Element Analysis. Coatings 14(6), 665. https://doi.org/10.3390/coatings14060665

[129] T.Hussain. (2012). Bonding between aluminium and copper in cold spraying: story of asymmetry. Materials Science and Technology. DOI: 10.1179/1743284712Y.0000000051

[130] M. Grujicic, C.L. Zhao, W.S. DeRosset, D. Helfritch. (2004). Analysis of the impact velocity of powder particles in the cold-gas dynamic-spray process.v Materials Science and Engineering: A .368(1-2):222-230. DOI: 10.1016/j.msea.2003.10.312

[131] Dassault Systèmes Simulia Corp., Abaqus/CAE User's Guide, Version 2016, Providence, RI, USA, 2016